SOLID DEPOSIT-INDUCED HIGH TEMPERATURE OXIDATION

by

Keeyoung Jung

BS, Korea University, 1997

ME, Korea University, 1999

MS, Carnegie Mellon University, 2002

Submitted to the Graduate Faculty of

Swanson School of Engineering in partial fulfillment

of the requirements for the degree of

Doctor of Philosophy

University of Pittsburgh

2008

UNIVERSITY OF PITTSBURGH

SWANSON SCHOOL OF ENGINEERING

This dissertation was presented

by

Keeyoung Jung

It was defended on

June 30, 2008

and approved by

Ian Nettleship, PhD, Professor, University of Pittsburgh

John P. Leonard, PhD, Professor, University of Pittsburgh

Sridhar Seetharaman, PhD, Professor, Carnegie Mellon University

Dissertation Co-Director: Gerald H. Meier, PhD, Professor, University of Pittsburgh

Dissertation Co-Director: Frederick S. Pettit, PhD, Emeritus Professor, University of Pittsburgh

SOLID DEPOSIT-INDUCED HIGH TEMPERATURE OXIDATION

Keeyoung Jung, PhD

University of Pittsburgh, 2008

The present study is aimed at investigating the high temperature oxidation induced by ash deposition from use of alternative fuels. The alloys and coatings being studied are typical of those used in current power generating gas turbines, as well as those that may be used in advanced systems.

To achieve this objective, the alloys Rene′ N5, GTD 111, and IN 738 as well as these alloys coated with platinum aluminide and CoNiCrAlY were exposed to conditions relevant to corrosion induced by using alternative fuels. The test conditions representative of deposits from use of alternative fuels were selected based upon initial experiments that involved testing the alloy Rene′ N5 with a platinum aluminide coating at 750°C, 950°C, and 1150°C in a variety of environments with deposits of CaO, $CaSO_4$, and Na_2SO_4. Based upon the results from such tests, a temperature (950^{o}C) and a deposit (CaO) were selected for the further experiments to compare the corrosion characteristics of all of the alloys and coatings.

At 950^{o}C with deposits of CaO, which are the selected experimental conditions obtained from the preliminary tests, accelerated cyclic oxidation experiments were performed with all uncoated and coated superalloys in extra dry air and wet (p_{H_2O}=0.1 atm) air to compare corrosion characteristics of each with one another. Experimental details will be described followed by the presentation of experimental results and discussion.

Additionally, uncoated GTD 111 specimens were exposed to different contaminants and moisture level environments to study the effect of contaminant level and water vapor pressure on CaO-induced degradation. Then, CaO deposits were coated on thermal barrier coatings (TBCs) and specimens with TBCs were exposed to the cyclic oxidation environments. The effects of deposits other than CaO, such as Fe_2O_3 and SiO_2, on the oxidation characteristics of the specimens were also investigated.

Finally, a mechanism for high temperature oxidation induced by CaO deposits was developed. It turns out that CaO directly reacts with protective oxides, such as Al_2O_3 and/or Cr_2O_3, to form non-protective ternary Ca compounds. Cracks are initiated and propagate along the weak interfaces between Ca compounds and underlying oxide layers resulting in spallation of Ca compound layers.

TABLE OF CONTENTS

LIST OF TABLES

LIST OF FIGURES

ACKNOWLEDGEMENTS

I would like to thank my mentors, Dr. Pettit and Dr. Meier, for their support and thoughtful advice. What I learned and experienced with them was priceless. I owe so much to them.

I also would like to thank my committee professors, Dr. Nettleship, Dr. Leonard, and Dr. Seetharaman, for their active participation in the overview of my PhD studies. Without their professional comments on my work, I could not have completed this work.

The completion of this dissertation would not be possible without help from my friends and colleagues. My thanks are due to all of them. I am particularly grateful to Meltem Yanar, Wesley Jackson, Mike Task, Edward Magee, Mike Helminiak, Kivilcim Hance, Scott Laney, Monica Maris-Sida, Erika Jackson, Andreas Kulovits, Chris Pekor and Sungjae Cheong for their helpful discussions, comments and suggestions on my work. I also have to express my gratitude and respect to Dr. Goldman for his considerate guidance.

Finally, my most sincere thanks are due to my wife, Eunha, my daughter, Jemine, and my family in Korea. I would like to express my deep love and appreciation for their support and love.

Pittsburgh, Pennsylvania, June 2008 **Keeyoung Jung**

1.0 INTRODUCTION

From the late 1940s to the 1970s, extensive research was performed to develop fuel specifications to reduce turbine hardware deterioration from fuel impurities. However, the advent of natural gas as the fuel of choice for land-based turbine engines gave rise to a discontinuity in the development of fuel specifications. During the period, turbine flow path environments for modern turbines were significantly changed by the advances in technology to increase the power and efficiency. For the newest turbine engines, pressure ratios have increased by a factor of two or more, inlet temperatures have risen, and new materials, such as directionally solidified and single crystal superalloys and/or thermal barrier coatings, have been incorporated to accommodate the higher temperatures.[1]

Recently, a need to use substitute fuels for natural gas has been even more greatly increased due to the significant increase of gas prices. The cost of producing electricity with power plants is directly related to the cost of the fuel being burned and accordingly, power generating companies are interested in operational changes that could reduce the cost and increase fuel flexibility.

A vast amount of research work with a variety of alternate fuels has shown that increasing inlet temperatures tend to increase deposition and corrosion of hot section hardware which was more severe especially in the presence of water vapor. However, the mechanism to explain significant corrosion, which seems to be caused by severe deposition at higher temperatures, is still not fully understood.

1.1 STATEMENT OF THE PROBLEM

When gas turbines use alternate fuels such as syngas, ash from the fuels can be deposited on turbine hardware. Although syngas-fired turbine plants utilize multiple stages of cleanup of the gasified product gas, limited quantities of impurities pass through the cleanup systems; these enter the gas turbine hot section flow path leading to a deposition of ash on the blade materials. This deposited ash after combustion can cause substantial corrosion of turbine hardware which may have significantly different characteristics than Type I and Type II hot corrosion.[1] These characteristics include the accelerated degradation of turbine hardware and the formation of unexpected corrosion products on the surfaces of coatings that have been applied as a protective component. Figure 1.1 shows cross-section micrographs of a service exposed turbine blade having four zones with different degradation modes: (1) the not too severely degraded coating zone, (2) the cracked coating zone, (3) the zone where the coating is gone mainly by erosion and the exposed substrate is subsequently oxidized, and (4) the severely degraded coating zone. The specimen was obtained from the first stage vanes of an electric power generating gas turbine that had used syngas for approximately 16,000 hours. The current study is concerned with degradation modes (1) and (3), i.e., the degradation of coatings and substrate alloys mainly due to deposit-induced high temperature oxidation. The mechanism to explain this type of

degradation is still not clear and the documentation of what happens during operation under these conditions has not been sufficiently studied.

This study is, therefore, directed at investigating and understanding the corrosion of materials induced by ash deposits typical of those that may form from use of alternate fuels derived from coal. The added complication of high moisture environments is also considered.

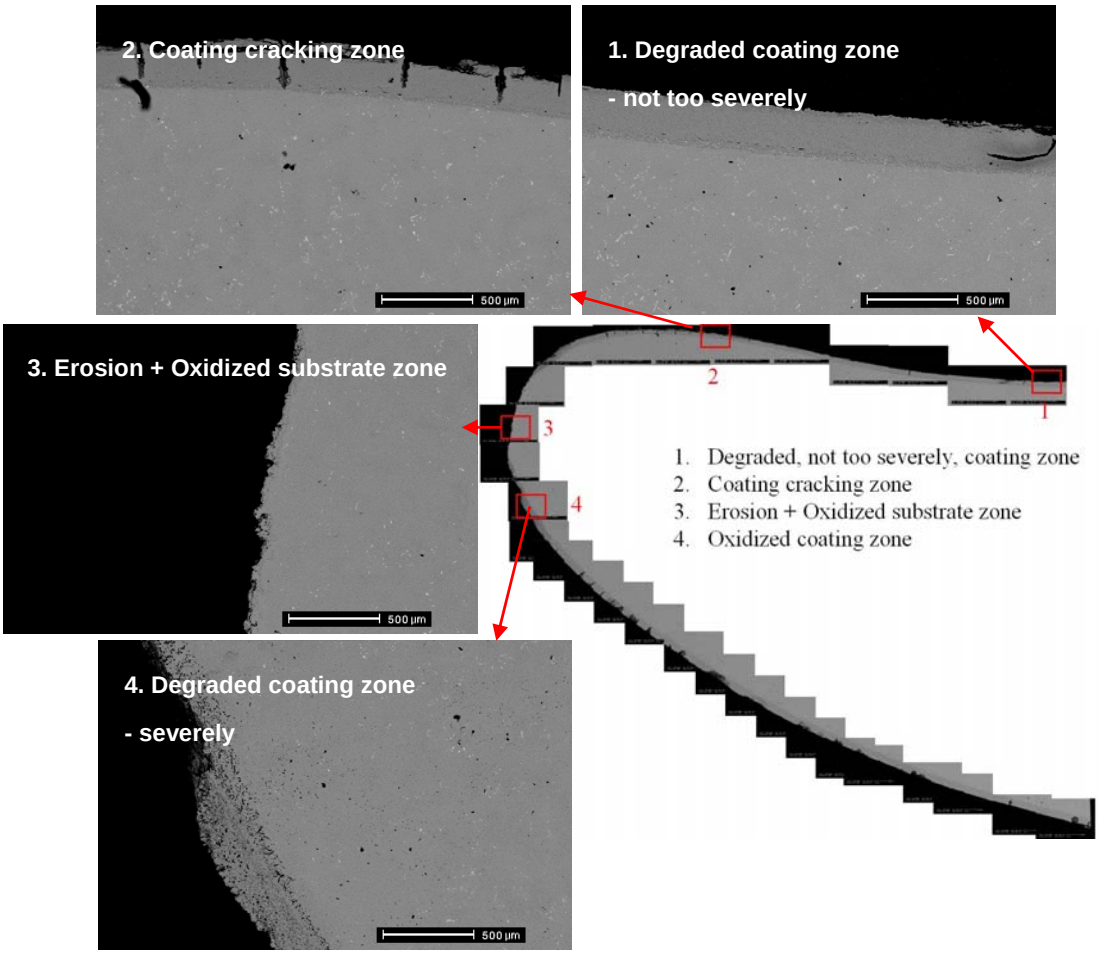

Figure 1.1 Cross-section micrographs of a service exposed turbine blade having four zones with different degradation modes: (1) the not too severely degraded coating zone, (2) the cracked coating zone, (3) the zone where the coating is gone mainly by erosion and the exposed substrate is subsequently oxidized, and (4) the severely degraded coating zone.

1.2 BACKGROUND

1.2.1 Fuels in Gas Turbines

About 75% of the currently installed gas turbines use natural gas and distillate fuels.[2] These fuels are categorized as conventional fuels. On the other hand, the non-conventional fuels are off-gases from iron making, low BTU natural gas, syngas derived from various source fuels, also heavy fuel oil, naphtha, or gas condensate fuels. The non-conventional fuels have a 25% share in the gas turbine market based on 2001 statistics and the share keeps increasing.[3] An estimated use of different fuel types in gas turbines based on 2001 statistics is shown in Figure 1.2.

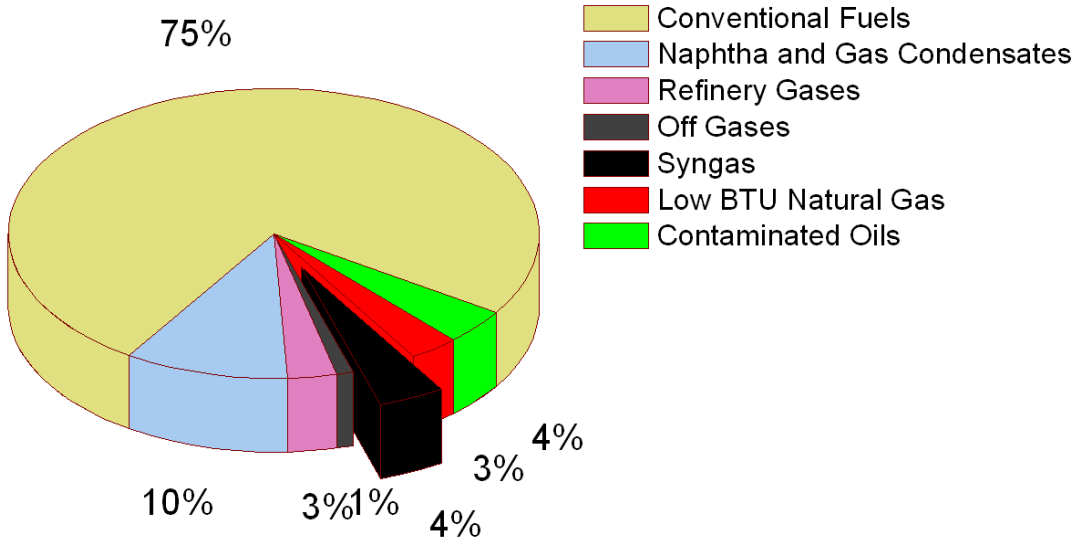

Figure 1.2 Percentage breakup of fuels used in gas turbines based on 2001 statistics.

Among the non-conventional fuels, synthetic gas or syngas is gasification fuel that is produced by either oxygen or air blown gasification process and formed using coal, petroleum coke or heavy liquids (biomass) as feedstock. Then, gasification fuel is purified. The syngas fuels generally are medium or low BTU gases and are comprised of a $CO/H_2/C_nH_m/N_2$ mixture and are suitable to burn in an Integrated Gasification Combined Cycle (IGCC) plant.[3] A schematic flow diagram of an IGCC plant, which utilizes the Heat Recovery Steam Generator (HRSG), is shown in Figure 1.3.[4]

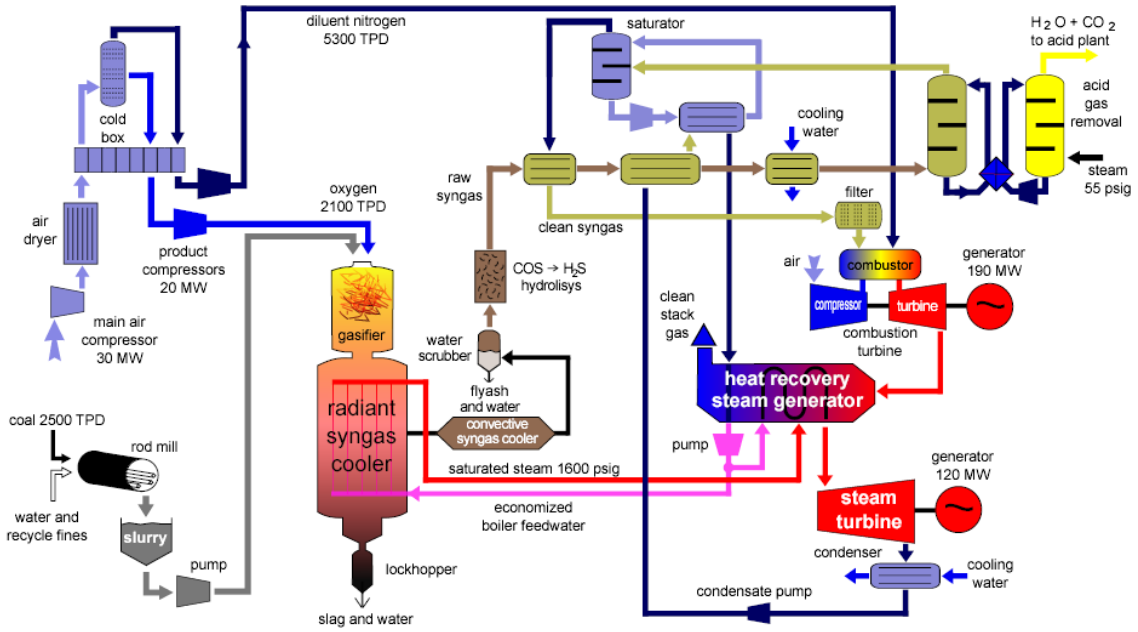

Figure 1.3 A schematic flow diagram of an IGCC plant. TPD = Tons per day.

In their 2007 Annual Energy Outlook, the DOE Energy Information Administration (EIA) documented history and projections of energy production by fuel as presented in Figure 1.4. Increasing coal use for electricity generation at existing plants and construction of a few new coal/syngas-fired plants lead to annual production increases that average 1.1 percent per year from 2005 to 2015, when total production is 25.7 quadrillion BTU. The growth in coal production is even stronger from 2015 to 2030, averaging 1.8 percent per year, as substantial amounts of new coal/syngas-fired generating capacity are added.[5] These projections lead the current research to become more important.

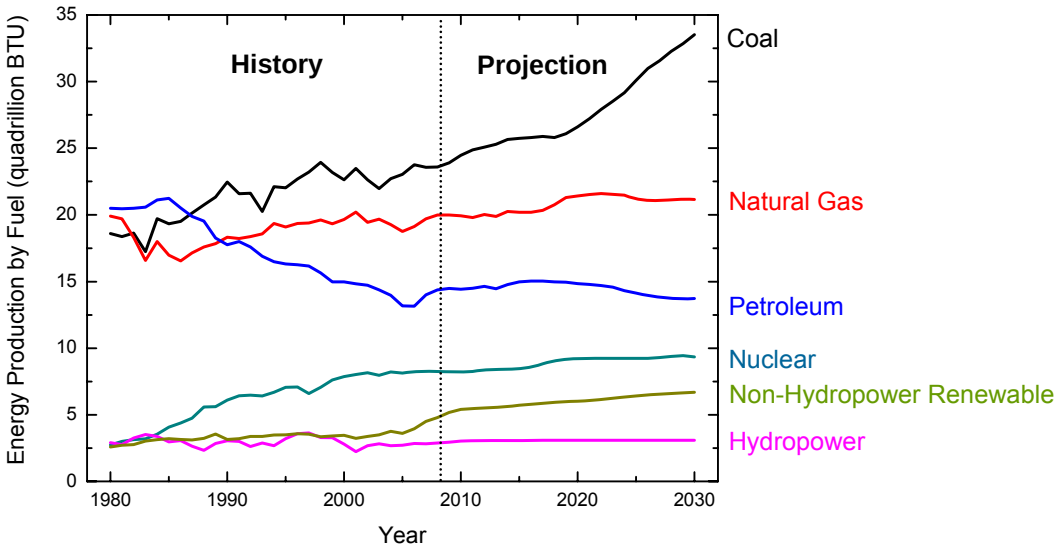

Figure 1.4 History and projections of energy production by fuel from 1980 to 2030.

Prices of three major commodities, i.e. petroleum, natural gas and coal, with respect to the period from 1993 to 2008 are presented in Figure 1.5. Note that coal price has increased continuously, but not greatly increased compared to price increases of the other two commodities over the period in the plot.[5, 6] Higher price projections for crude oil and natural gas lead to slower projected demand for crude oil and natural gas and faster projected growth in use of coal and other non-hydroelectric renewable energy sources.

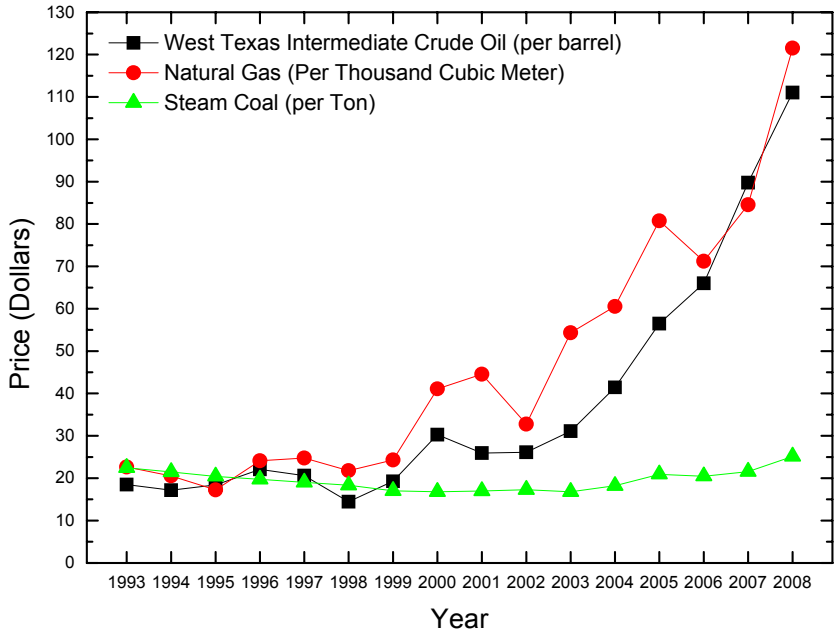

Figure 1.5 Prices of three major commodities for electricity generation: petroleum, natural gas, and coal from 1993 to 2008. Prices in 2008 are prices as of April 2008.

Currently, more than twenty syngas-fired turbine plants have been constructed world wide and many more are being considered for the future.[7] Since the turbines used in these plants and their hot gas path materials have typically been designed to operate with natural gas which is considered as the purest of fuels, materials performance associated with operation with syngas fuels is of concern. When gas turbines use these syngas fuels, ash from the fuels can deposit on turbine hardware. This deposited ash can cause substantial corrosion of turbine hardware.[1-3]

1.2.2 Deposit-Induced Hot Corrosion of Alloys

The accumulation of airborne contaminants which deposit on hot surfaces in gas turbines has always been a point of concern due to degradation of engine performance resulting from blockage of flow paths and cooling holes, as well as due to accelerated corrosion of alloys and coatings induced by the deposits. This study is concerned with the latter problem, namely, the deposit-induced accelerated corrosion of alloys and coatings. Over the past three quarters of a century, a number of examples of deposit induced accelerated corrosion of different alloys and coatings have been documented.[8-40] Some of these examples are described briefly in the following.

Because corrosion by a thin electrolyte film has some common characteristics with atmospheric corrosion by an aqueous film at around room temperature, the phenomenon has

been renamed 'hot corrosion'. Aqueous atmospheric corrosion is often controlled by the diffusion of dissolved oxygen in the water film, the soluble oxidant in hot corrosion is SO_3 ($S_2O_7^{2-}$) in the fused sulfate salt.[8]

The subject of hot corrosion is divided into two types: type I – high temperature hot corrosion above about 900°C where pure Na_2SO_4 is above its melting temperature as described above, and type II – low temperature hot corrosion between about 650°C and 800°C where a liquid salt phase is only formed because of significant dissolution of some corrosion products in the presence of SO_3 in the gas.[9-15] Corroded components show a dispersion of tiny oxide particles in the adherent thin salt film is often observed. This observation led to the suggestion that a fluxing mechanism may be important, whereby an otherwise protective oxide scale on the material dissolves at the oxide/salt interface but precipitates as non-protective particles within the salt film.[16] Whenever fuels with high impurity contents of elements such as S, Na, and V, are used in gas turbines, deposits of Na_2SO_4 or $NaVO_3$ may be formed on turbine blades and vanes. When the hardware surface temperatures are between about 800°C and 950°C (above 950°C, these deposits are not present in significant quantities), the Na_2SO_4 can cause high temperature hot corrosion, Type I hot corrosion, with degradation microstructures such as those presented in Figure 1.6.[15] The mechanisms for this type of hot corrosion are well documented in the literature[15-21] and are often encountered in aircraft gas turbines.[21-22] If the deposits are $NaVO_3$,

sulfides are not present in the alloy, as is the case for Na_2SO_4 deposits, but corrosion is excessive as shown in Figure 1.7 and Figure 1.8.[23] A thin deposit of fused salt on an alloy surface in a hot oxidizing gas causes accelerated corrosion. Recognition of the problem and a search toward a mechanistic understanding were initiated in response to the severe attack of military gas turbines during the Vietnam conflict.[16, 21]

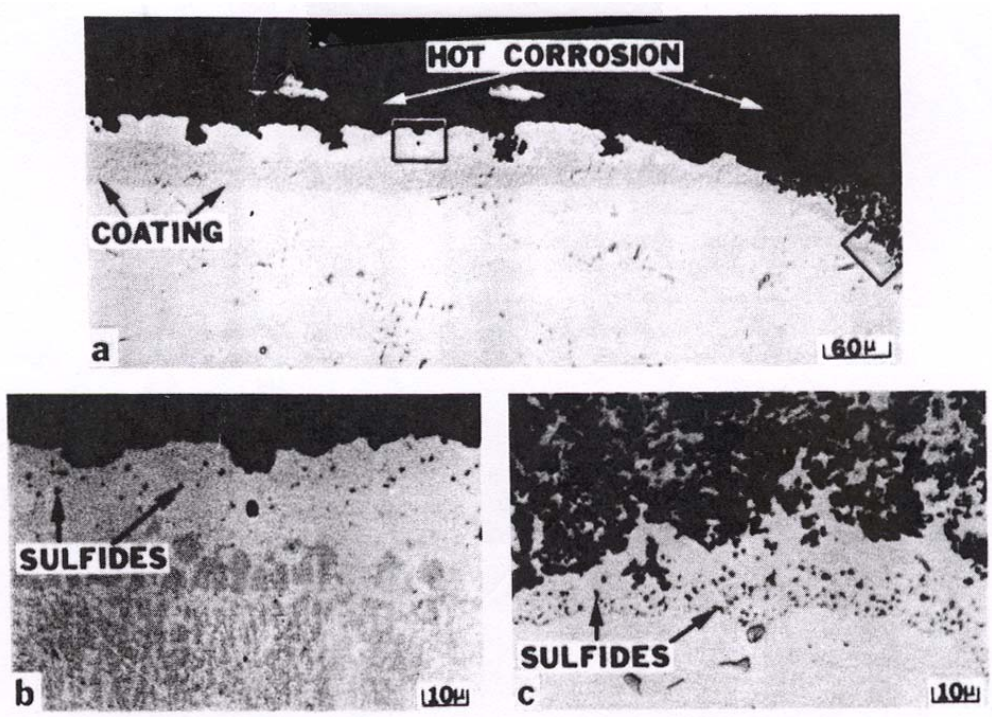

Figure 1.6 Photomicrographs showing the microstructural features developed during high temperature hot corrosion of a coated airfoil from an aircraft gas turbine. Protrusions of oxide have developed into the coating, (a), and sulfides are present in the coating, (b). At one location, the coating has been penetrated and the superalloy substrate has undergone hot corrosion attack, (c).

Initially, the researchers were misled by the observation of corrosion product sulfides beneath a fused film of sodium sulfate to denote the problem and mechanism as sulfidation.[24] Bornstein and DeCrescente showed that hot corrosion could occur due to basic fluxing saying that the presence of a condensed fused salt film is required for severe attack and that Na_2SO_4 vapor in air is innocuous.[22, 25]

Goebel and Pettit studied the attack of pure Ni and Ni-base alloys beneath a fused Na_2SO_4 film at 1000^{o}C and demonstrated that the principal corrosive environmental component was not a vapor species, but rather the contact of the fused salt with the surface.[26] Later, they also showed that Al_2O_3-forming Ni-base alloys containing the refractory elements, Mo, W, or V, can suffer Na_2SO_4-induced catastrophic attack with the formation of stable solute ions involving oxide ions (MoO_4^{2-}, WO_4^{2-}, or VO_3^{-} ions, respectively).[27]

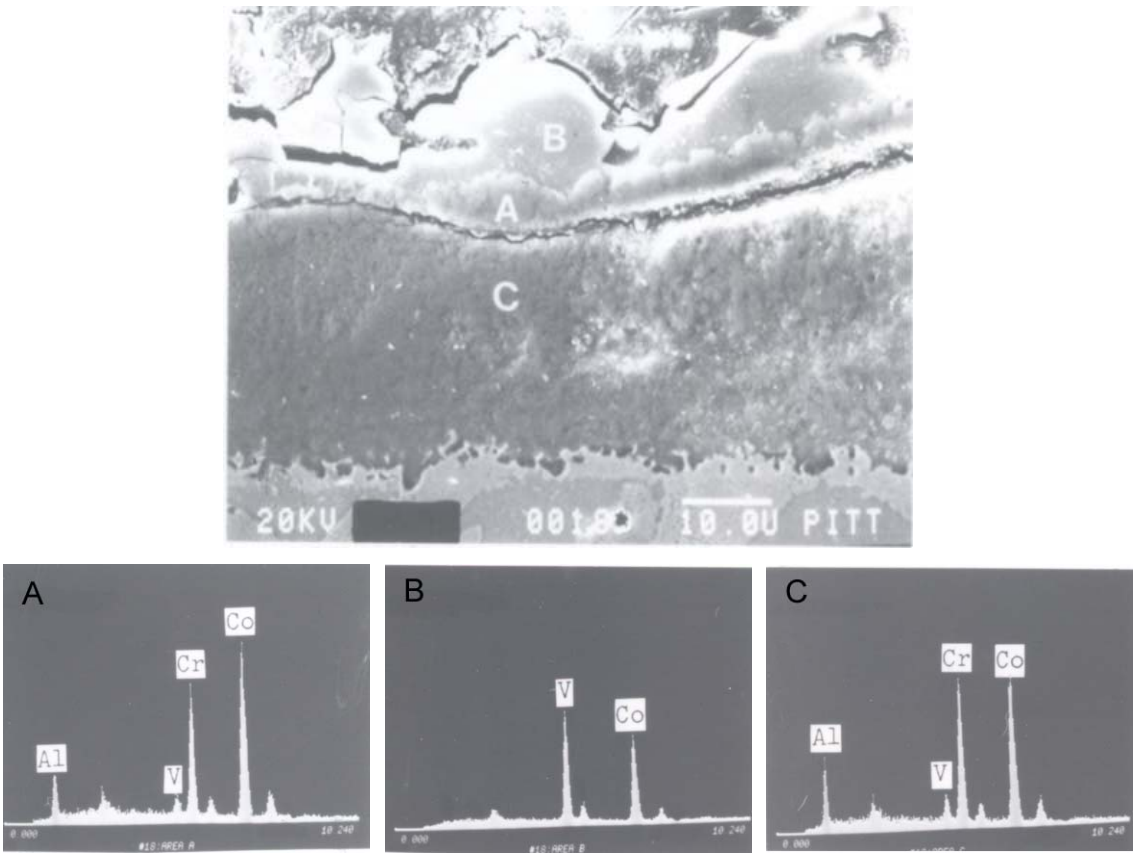

Figure 1.7 A scanning electron micrograph and EDS spectra for CoCrAlY alloys exposed to Na_2SO_4-50 mol% $NaVO_3$, at 973K in oxygen containing 640ppm SO_2.

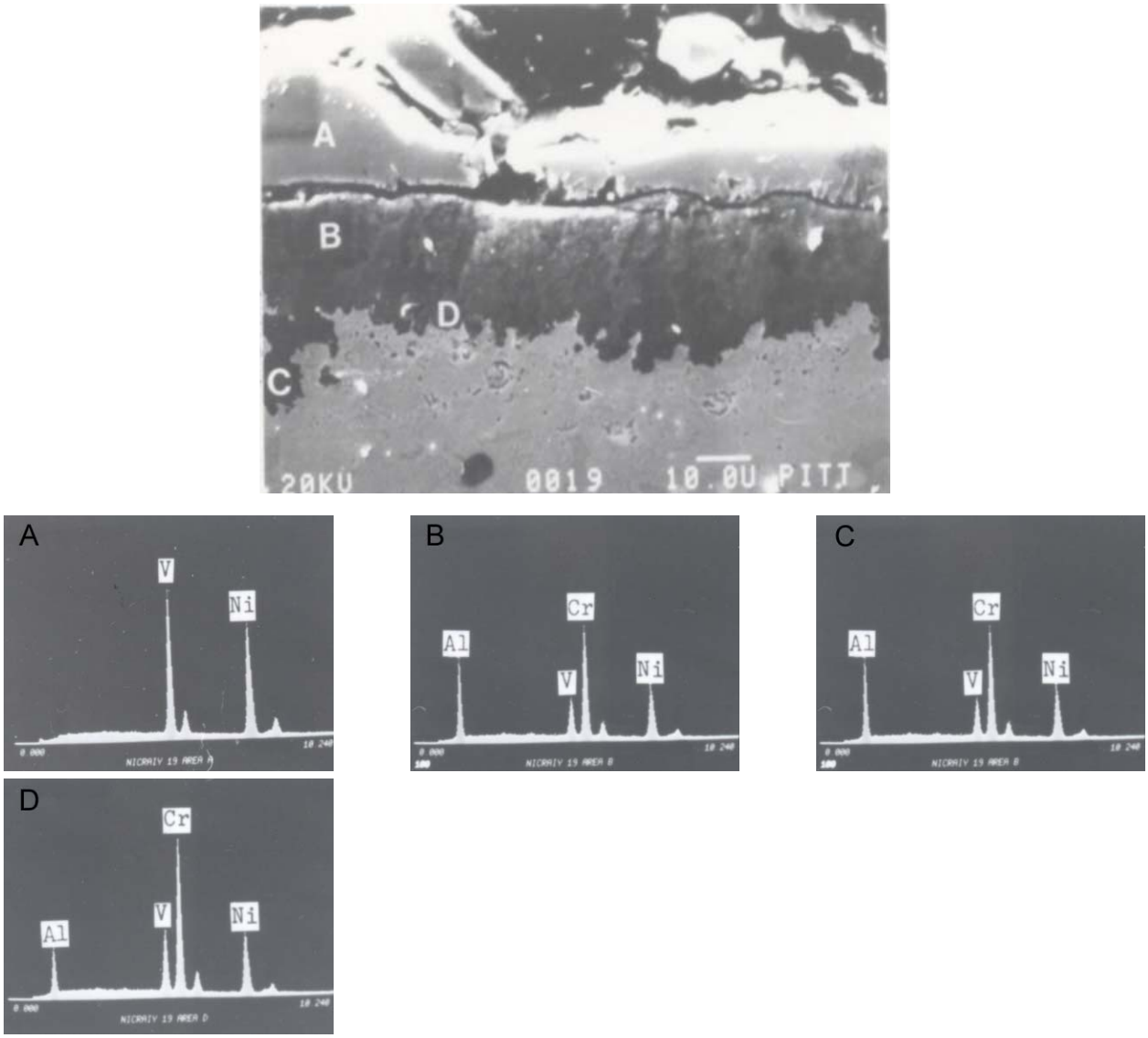

Figure 1.8 A scanning electron micrograph and EDS spectra for NiCrAlY alloys exposed to Na_2SO_4-50 mol% $NaVO_3$, at 973K in oxygen containing 640 ppm SO_2.

In the case of gas turbines used for propulsion of marine vehicles, sea salt is often present in the ingested air, and the fuel is often not of the quality of that used in aircraft gas turbines. If sea salt is ingested in the intake air, NaCl may be deposited on turbine hardware, and the chlorine in the deposit can preferentially remove aluminum from alloys and coatings causing a degradation microstructure consisting of numerous pores as shown in Figure 1.9.[15] The addition of NaCl into Na_2SO_4 considerably accelerates the corrosion of the single crystalline superalloy and the corrosion scale becomes more porous due to the sulfide formation and its subsequent oxidation.[15, 28]

Also, the operating temperatures are not usually as high as in aircraft gas turbines. As a result of such conditions, degradation of turbine hardware can occur via low temperature hot corrosion, or Type II hot corrosion as shown in Figure 1.10.[9-17, 29] In this type of hot corrosion, sulfides are often not present in the alloy adjacent to the corrosion products, however, some alloys, especially those rich in nickel, can have substantial sulfide formation.[9] To induce this type of hot corrosion, in addition to Na_2SO_4 deposits, SO_3 must be present in the gas phase at partial pressures in the range 10^{-3} - 10^{-6} atms.[26, 29]

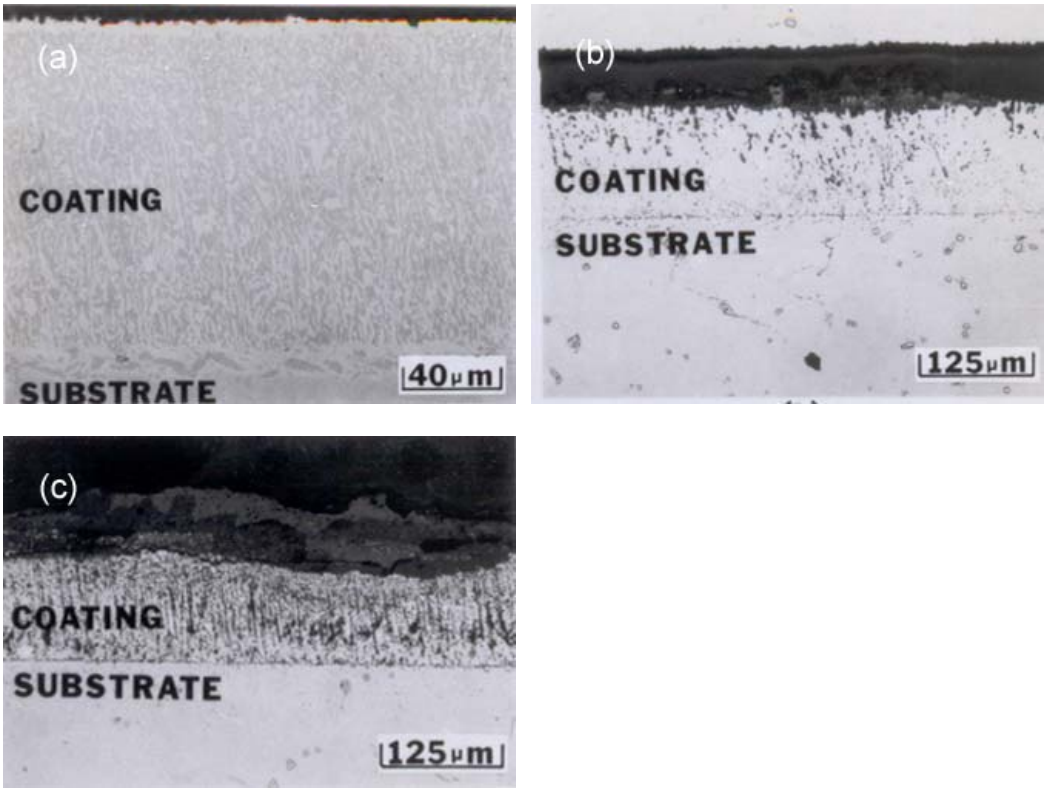

Figure 1.9 Photomicrographs to compare the degradation of CoCrAlY coatings on IN 738 after exposure at 899^{o}C in air to Na_2SO_4 deposits containing different amounts of NaCl. (a) 500 hours with Na_2SO_4 deposits, (b) 500 hours with Na_2SO_4-5 wt% NaCl and (c) 40 hours with Na_2SO_4-90 wt% NaCl.

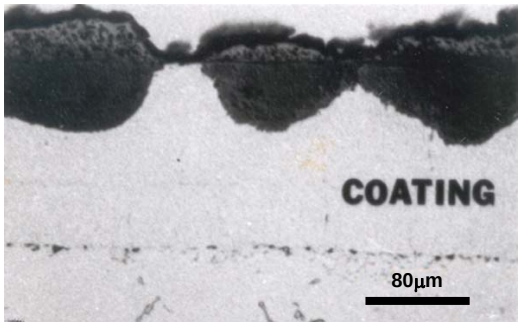

Figure 1.10 A photomicrograph showing the microstructural features developed during the hot corrosion of gas turbine materials in marine service: Low temperature hot corrosion of a CoCrAlY coating after 4200 hours of service, Type II.

Hot corrosion mechanisms induced by a thin film of fused salt deposit have been reviewed by Rapp[16] and Kofstad[30] describing roles of scale fluxing, electrochemical reactions, alloy sulfidation, synergistic dissolution, and strong acidic oxides etc. Measurements of the solubilities of important oxides NiO, Co_3O_4, Fe_2O_3, CeO_2, Cr_2O_3, and Al_2O_3 have been determined as a function of melt basicity and oxygen activity for pure fused Na_2SO_4 at 1200K, and for SiO_2 at 973K. A compilation of these results is presented in Figure 1.11.[10-12, 31-36] In the case of Al_2O_3, the solute is Al_2O_3, but the basic species is AlO_2^- and the acidic species is Al^{3+} by the following reactions:

Acidic reaction: $3SO_3 + Al_2O_3 = 2Al^{3+} + 3SO^{4-}$

Basic reaction: $Al_2O_3 + O^{2-} = 2AlO^{2-}$

The V-shapes of these curves are explained by the formation upon dissolution of an acidic or a basic species, e.g. the solubilities of oxides are described by two contributions or legs on the curve of Figure 1.11.

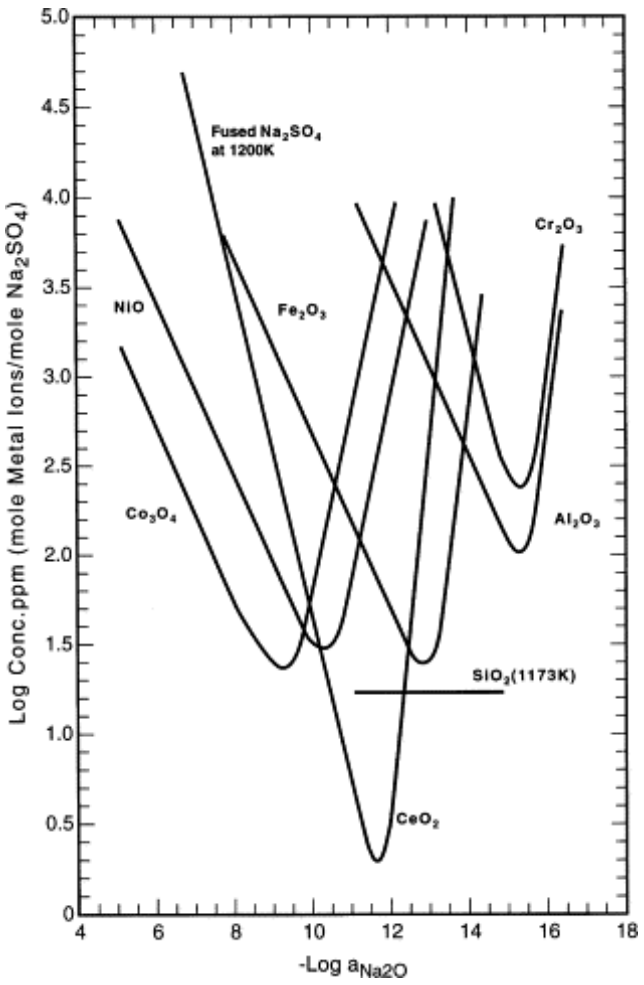

Figure 1.11 Compilation of measured solubilities for several oxides in fused pure Na_2SO_4 at 1200K.

Based on the expectation that oxide solubilities would exhibit individual basic and acidic species with concentrations dependent on melt basicity and perhaps P_{O_2} $_{O2}$, a 'negative solubility gradient' was proposed as a general criterion for continuing hot corrosion attack. Figure 1.12 shows a schematic drawing of this fluxing mechanism.[37-38] If the fuels contain vanadium, hot corrosion attack due to $NaVO_3$ deposits can also occur in this temperature range over 650 – 800°C.[23]

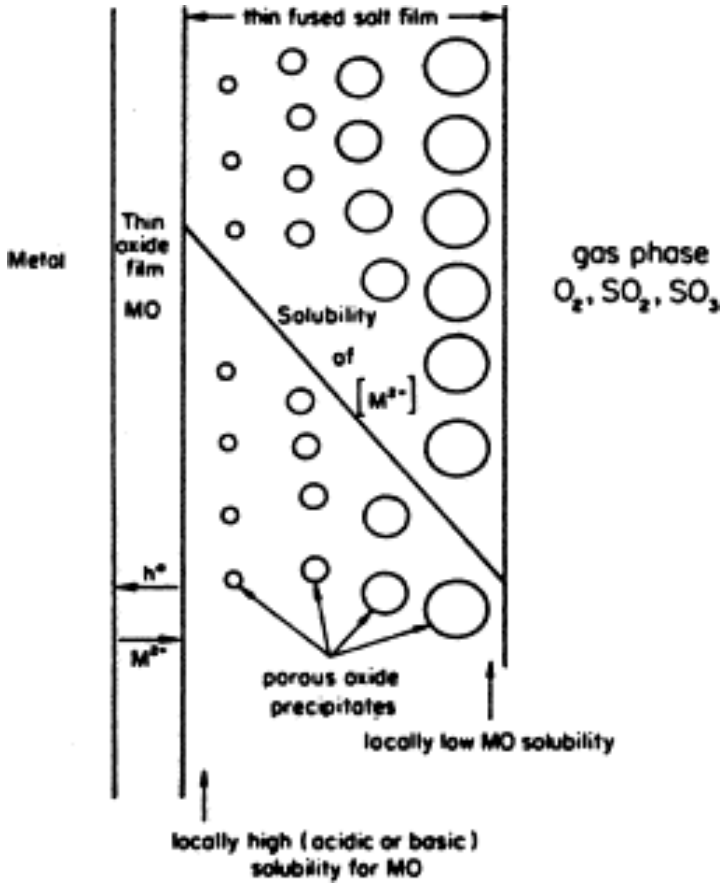

Figure 1.12 Reprecipitation of porous MO oxide supported by a negative solubility gradient in the fused salt film.

Figure 1.13 summarizes mechanisms of deposit-induced high temperature oxidation. The current study is focused on solid deposit induced high temperature degradation mainly via direct chemical reaction between solid deposits and coatings/superalloys both in dry and moist environments.

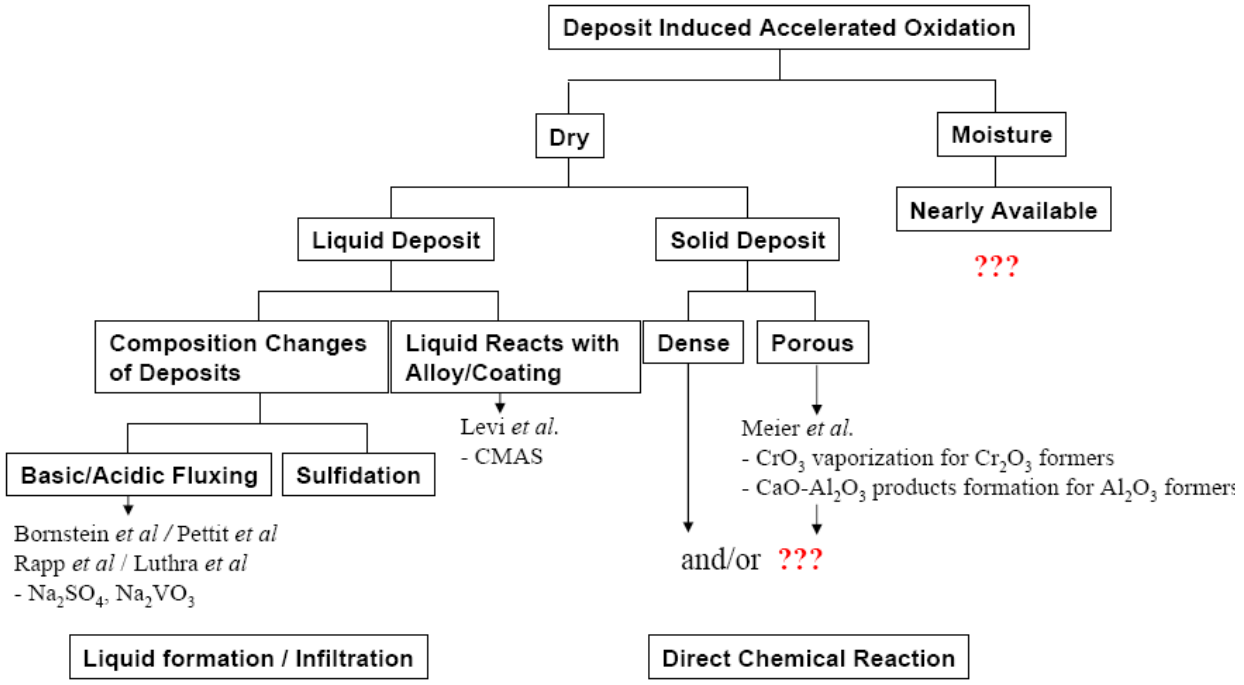

Figure 1.13 Summary of mechanisms for deposit-induced accelerated oxidation. Red question marks indicate regimes that were explored in the current study.

1.2.3 CMAS-Induced Failure of Thermal Barrier Coatings

The nature of the deposit that is formed depends upon the operating conditions of the gas turbine, in particular, the turbine inlet temperature, the quality of the fuel and the characteristics of the intake air.

As the turbine inlet temperatures have been increased, due to the use of thermal barrier coatings (TBCs), deposits of calcium-magnesium-aluminum-silicate (CMAS) with melting points around 1190^{o}C have been observed to develop on turbine hardware.[41] At times aircraft gas turbines can ingest dust from runaways. Also, dust can be ingested when aircraft fly near volcano eruptions. Such deposits form due to material in the intake air and can cause degradation of the TBCs. The failure characteristics of TBCs with CMAS[42] are different from those without any doposit.[43-44]

Upon cooling to ambient temperatures, the CMAS on the surface of the TBC solidifies with an effective modulus significantly larger than that of the porous TBC structure. This stiffer layer can have enough stored energy in it to debond from the rest of the TBC layer. Once debonding occurs, the newly exposed surface of the TBC can be infiltrated by subsequent CMAS deposits, with the process repeating itself until unacceptable amounts or all of the TBC is removed. The TBC failure mechanism associated with the cold shock of the infiltrated CMAS

layer during shut down is illustrated in Figure 1.14[45] and an example of CMAS infiltration induced TBC delamination is shown in Figure 1.15.[42] There is not much data in the literature describing the effect of CMAS on the corrosion of alloys and metallic coatings, however a thermochemical approach to investigate the degradation phenomena of thermal barrier coatings (TBCs) using a model CMAS composition and 7YSZ (ZrO_2-7.6%$YO_{1.5}$) on an alumina substrate is now in progress.[46] It is found that CMAS rapidly penetrates the open structure of the coating as soon as melting occurs, whereupon the original 7YSZ dissolves in the CMAS and reprecipitates with a different morphology and composition that depends on the local melt chemistry.

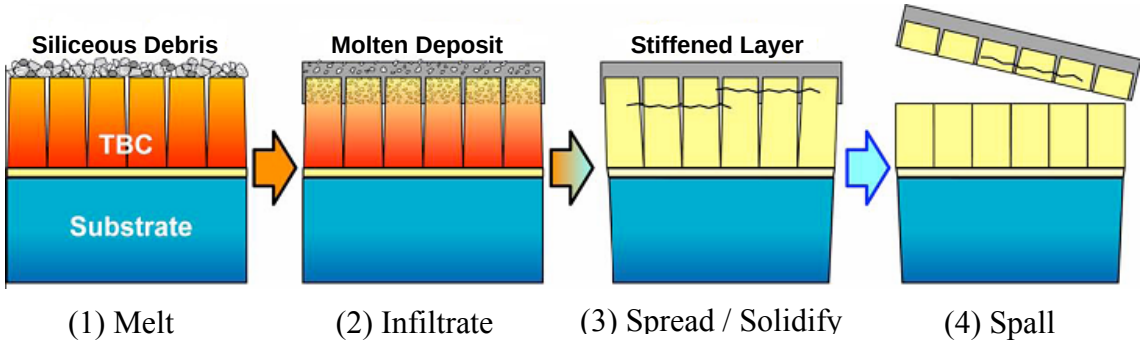

Figure 1.14 A schematic diagram showing the TBC failure mechanism due to molten CMAS deposit infiltration.

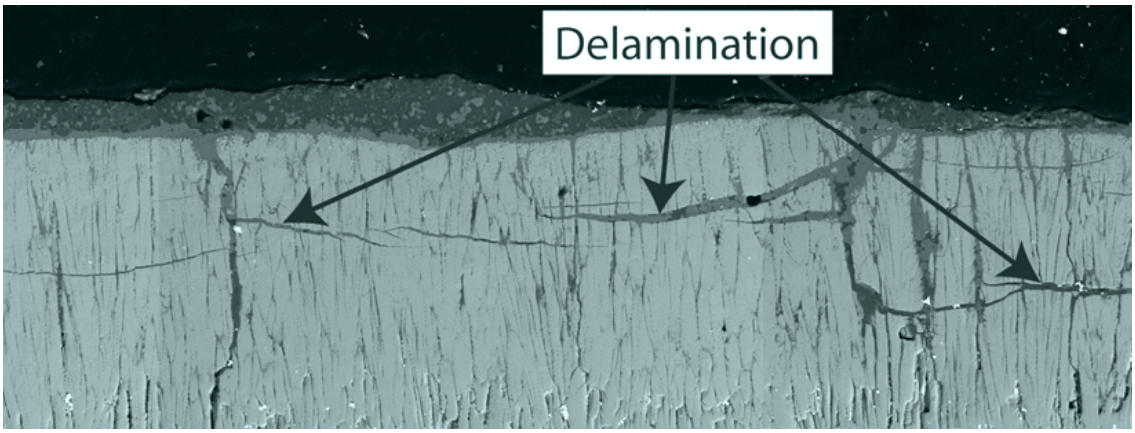

Figure 1.15 A cross-section micrograph of an EB-PVD TBC showing typical delamination cracks associated with the cold shock of the infiltrated layer during shut down.

1.2.4 Ash Deposits from Fuels

When fuels are used in gas turbines that have been derived from coal, or other practicable sources, ash can be formed on turbine hardware which can cause corrosion.[47] It is the inorganic matter in fuels that leads to problems with corrosion and deposits.[48] The composition of the ash is difficult to describe precisely. In most coals about 95% of all the mineral matter is made up of kaolinites ($Al_2O_3 \cdot 2SiO_2 \cdot 2H_2O$), pyrites ($FeS_2$) and calcites ($CaCO_3$).[48] In tests performed using 2 to 3 ppmw ash particulate in the combustion stream, more deposition and corrosion was observed at a gas temperature of 1260^{o}C compared to 1093^{o}C.[47] This corrosion differed from Type I hot corrosion and involved calcium.

Both physical and chemical factors play roles in the formation of deposits. Deposits accumulate on surfaces by at least four physical processes: molecular diffusion, Brownian motion, turbulent diffusion and inertial impact.[48] Although particles of ash may arrive at a surface by physical transport, the accumulation of the ash to form substantial deposits will depend upon the adherence of particle to particle. When the particle to particle adherence is strong ash will continue to build up into thick layers. The sintering characteristics of the ash are affected by many factors, but the composition, temperature, and the time the particles are in contact with each other on a heat receiving surface are the most important factors. Depending upon such factors a transition temperature can exist above which increased deposition occurs.

In considering the deposits that may develop when using fuel derived from coal, it is reasonable to consider CaO and $CaSO_4$, and to compare the attack to that induced by Na_2SO_4 deposits. The influence of deposits of CaO, $CaSO_4$, and MgO on the oxidation behavior of a number of Cr_2O_3-forming and Al_2O_3-forming alloys has been investigated over the temperature range 850°C to 1050°C.[49] Deposits of CaO were observed to accelerate the degradation of Cr_2O_3-forming alloys in oxygen or air by two mechanisms, namely; accelerated CrO_3 evaporation over the entire range studied, and liquid formation by reaction between CaO and Cr_2O_3 at temperatures above 1000°C which resulted in catastrophic corrosion. The corrosion of Al_2O_3-forming alloys that developed transient Cr_2O_3 was also substantially increased by the CaO

deposit. Deposits of $CaSO_4$ did not cause any accelerated corrosion. Deposits of MgO caused increased evaporation of CrO_3, but no corrosion due to the formation of liquid phases containing MgO. The effects of coal-water fuels on materials in modern gas turbine conditions were evaluated by Wenglarz *et al.*[50] They observed the accelerated oxidation of a CoCrAlY coated IN 738 turbine alloy exposed in a subscale turbine combustor.

1.2.5 Effects of Water Vapor on the Oxidation of Alloys

In examining the effect of deposits upon the corrosion of alloys and coatings, it is also necessary to consider the effect of water vapor on such corrosion processes. The effect of water vapor on the oxidation of a variety of alloys including superalloys has been studied in a number of investigations.[51-70] The effect of water vapor on the oxidation of a number of Cr_2O_3-forming and Al_2O_3-forming alloys has been investigated by Meier *et al.*[51-55] The results from this investigation showed that water vapor caused the oxidation resistance of Cr_2O_3-forming and Al_2O_3-forming alloys to be decreased. Water vapor affected the oxidation resistances of these alloys by causing the oxide scales to crack and spall more severely. This increase in spalling of the oxide scales occurred because water vapor decreased the interfacial toughness of the oxide-alloy interface. Water vapor also adversely affected selective oxidation of aluminum in the alloys that were Al_2O_3 formers. This adverse effect on selective oxidation was observed in nickel base

superalloys rather than coatings on such superalloys. The selective oxidation of aluminum in the nickel base superalloys was adversely affected by water vapor since it caused more transient oxidation during the development of Al_2O_3 scales on these alloys. Essuman *et al* revealed that the presence of water vapor affects the transport processes not only in the scale but also in the alloy.[56]

The effects of water vapor depend upon the alloy and the experimental conditions. Water vapor has been found to affect the high temperature oxidation of alloys in the following ways through the following mechanisms:

1. The presence of water vapor permits a H_2-H_2O mixture to be formed in voids which facilitates a rapid inward transport of oxygen across the pores via dissociative gas transport (an oxidation-reduction process).[57-58]

2. Water vapor can affect the plasticity of oxide scales. Some investigators propose that the plasticity of oxide scales is decreased and, consequently, the spalling of scales is increased.[59] Other investigators have proposed that plasticity of oxide scales is increased[60] with increased oxidation rates or improved adherence.[58]

3. The presence of water vapor adversely affects the selective oxidation of elements such as aluminum and chromium from iron-base alloys.[61] It has also been found that water vapor affects the selective oxidation of aluminum from TiAl.[62]

4. Water vapor can affect transport through oxides such as SiO_2 by causing the network structure to be changed.[63]

5. Water vapor can cause the vaporization of some oxides to be increased because of the formation of hydrated species with high vapor pressures.[64-68]

6. Water vapor causes the concentration of proton defects in oxide scales to be increased which can influence defect-dependent properties such as high temperature creep and diffusion.[67, 69]

The effects of water vapor on hot corrosion processes, and on mixed gas corrosion (e.g., in SO_2-O_2-SO_3 gas mixtures), have not been examined but, in view of the results obtained from oxidation experiments, water vapor can be expected to influence these more complex high temperature corrosion processes.

2.0 OBJECTIVES

The objectives of this study were conduct experiments, whereby the oxidation degradation of selected materials are documented in high moisture gas environments and in such environments but with corrosive contaminants on specimens with emphasis on deposits that are encountered in the use of alternate fuels in gas turbines. More specifically, the goals were perform laboratory cyclic and isothermal oxidation tests in a gas environment of air with water vapor and in the same gas environment but with deposits of Na_2SO_4, CaO, and $CaSO_4$ to achieve the following:[71]

1. Develop a fundamental understanding of the degradation processes in moisture environments and in such environments where the specimens have deposits with emphasis on those that will be encountered from alternate fuels.

2. Attempt to describe how moisture/contaminant levels and temperature affect the corrosion processes.

3. Determine the alloy compositions and coatings that are most resistant to corrosion induced by deposits from alternate fuels.

3.0 RESEARCH APPROACH

3.1 OVERVIEW OF EXPERIMENTAL APPROACH

To achieve the objectives described in the previous section, the following experimental approach was developed. First, CaO and $CaSO_4$ deposits were selected which were considered as representative deposits which could be formed when syngas was used as an alternate fuel in gas turbines. The oxidation characteristics of specimens coated with CaO and $CaSO_4$ deposits were compared to those coated with Na_2SO_4 deposit for which much data is already available. Of course, specimens with no deposit were also in the plan as well as tests in wet and dry air. Experimental details including materials used in this study and experimental procedures are described in section 3.2.

In order to determine a test temperature (T_1) and a deposit (D_1) for the further experiments, initial experiments were planned. These tests were performed at 750^{o}C, 950^{o}C and 1150^{o}C for specimens coated with three different deposits, CaO, $CaSO_4$ and Na_2SO_4. Details are described in section 3.3. These tests were to enable reducing the total number of specimens by selecting an appropriate test condition for the further extensive experiments.

Under the conditions that were selected in the initial experiments, the main accelerated cyclic oxidation experiments were conducted to investigate the effect of the deposits on the high temperature oxidation characteristics of different uncoated and coated alloys. Then, these results are compared to one another to study the effect of the kind of alloys and coatings in terms of kinetics and microstructural analyses using the Optical Microscope (OM), the Scanning Electron Microscope (SEM), Energy Dispersive X-Ray Analysis (EDX) and X-Ray Diffraction (XRD), etc. Details of these experiments are described in section 3.2.

In section 3.3, experimental procedures are described. Experimental procedures include: (1) comparison of uncoated alloys, (2) comparison of coated alloys, (3) the interactions between CaO and oxide scales, (4) the effects of CaO deposits on thermal barrier coatings, (5) determination of contamination/moisture limits, and finally (6) the effects of Fe_2O_3 and SiO_2 on coated and uncoated alloys.

3.2 EXPERIMENTAL DETAILS

3.2.1 Materials and Specimen Preparation

The alloys used in this study were Rene′ N5, GTD 111 and IN 738. The alloy Rene′ N5 is used in advanced gas turbines and the alloy GTD 111 was selected because it is used in current industrial gas turbines. The alloy IN 738 is looked upon as an alloy that has some resistance to Na_2SO_4-induced hot corrosion attack. Rene′ N5 is a single crystal alloy and an α-Al_2O_3 former, whereas IN 738 is a polycrystalline alloy and a chromia former. GTD 111 is a directionally solidified polycrystalline alloy and is also a chromia former. The compositions of these alloys are presented in Table 3-1.

Table 3.1 Nominal compositions of the alloys used in the current study*

Alloy	Ni	Cr	Al	Co	Ta	W	Mo	Ti	B	Hf	Re
Rene′ N5 (SC)	Bal.	7	6.2	7.5	6.5	6.0	0.2	---	---	0.1	3.0
GTD 111 (DS)	Bal.	14	3.0	9.5	2.8	3.8	1.5	4.9	0.01	---	---
IN 738	Bal.	16	3.4	8.5	1.7	2.6	1.7	3.4	0.01	---	---

* Unless indicated otherwise all compositions are presented in weight percent.

The composition of a protective layer formed on the surface via selective oxidation is determined by the composition of the underlying materials associated with the activity of each element. If the activity of Cr is high at the surface, Cr_2O_3 will be formed as an external oxide layer. On the other hand, if the activity of Al or Ni is high, Al_2O_3 or NiO will be formed, respectively. Protection schemes for NiCrAl alloys via selective oxidation are represented in an oxide map where oxidation data are superposed on the ternary composition triangle, as shown in Figure 3.1.[72-74] Three primary regions of oxidation can be corresponding to (I) external scales of only Al_2O_3, (II) Cr_2O_3 external scales + Al_2O_3 internal oxides, and (III) NiO external scales + Al_2O_3/Cr_2O_3 internal oxides.

For the exposure tests, rectangular shaped coupon specimens made of materials to be tested were prepared. These coupon specimens were cut from the alloy ingots. The dimensions of specimens were 15×10×3 mm with a 3 mm diameter suspension hole. The hole is used to hang specimens on silica rods.

The results obtained from the oxidation studies by Meier *et al.* in wet and dry air definitely showed that coatings should also be investigated.[52] In the present study, therefore, an MCrAlY type coating, namely a CoNiCrAlY (Co-32Ni-22Cr-10Al-0.3Y) coating as well as a platinum-modified aluminide coating, also called a platinum aluminide coating, were investigated. Both coatings should provide resistance to cyclic oxidation in wet environments.

The CoNiCrAlY coating is used in some current power generating gas turbines. Platinum aluminide coatings are mainly used in aircraft gas turbines. However, a substantial amount of data is available for the degradation of these coatings in moist and dry air. The platinum aluminide coating was included because it is believed to be necessary to have an aluminide coating for comparison with the MCrAlY coating.

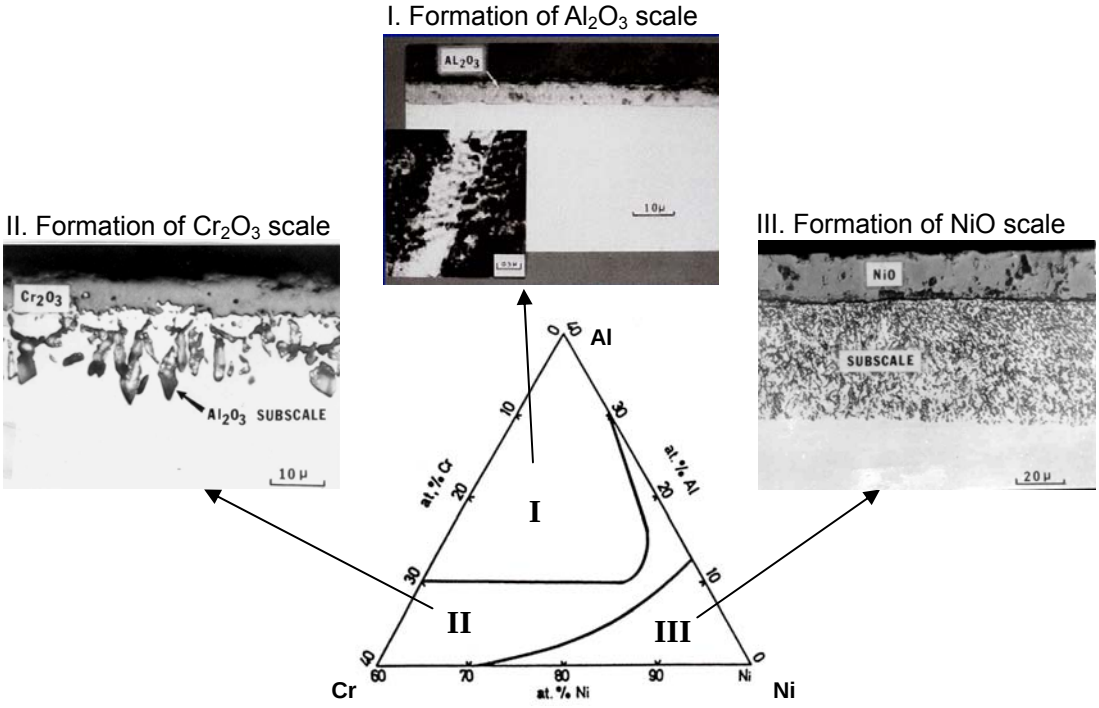

Figure 3.1 An oxide map triangle showing protection schemes for NiCrAl alloys via selective oxidation.

All superalloy specimens were polished through 1200 grit SiC polishing papers before being coated and exposed by themselves. The platinum aluminide coatings were prepared by electrolytic deposition of a thin (about 5 μm thick) platinum layer followed by chemical vapor deposition (CVD) of aluminum. The specimens underwent a thermal diffusion treatment at about 700^{o}C for two to four hours under an argon atmosphere before and after aluminum deposition in order to obtain good metallic bonding between the layers. The CoNiCrAlY coating was coated using a high velocity oxygen fuel (HVOF) thermal spray process. The HVOF coating process introduces powders of CoNiCrAlY alloy into a high temperature, high velocity gas stream. The steam heats and propels them against prepared substrate alloy surfaces. HVOF coatings have good density (low porosity) and low oxide levels providing enhanced wear and corrosion resistance. Schematic diagrams for CVD and HVOF coating processes are shown in Figures 3.2 (a) and (b), respectively.[75]

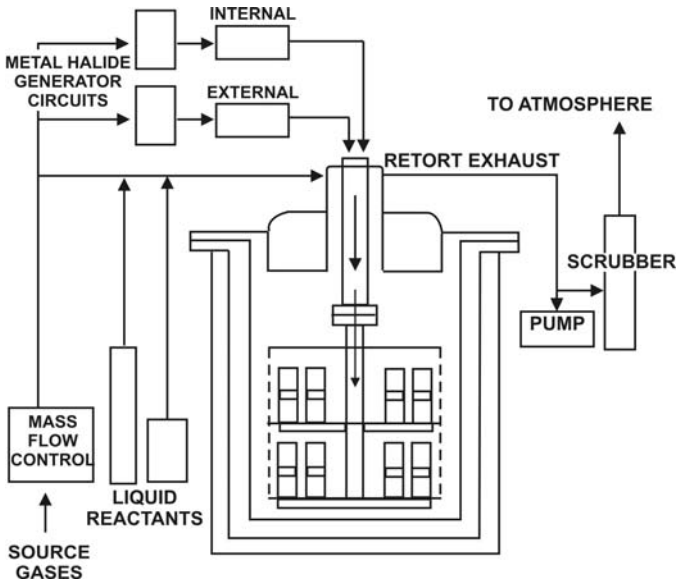

(a) CVD aluminizing process

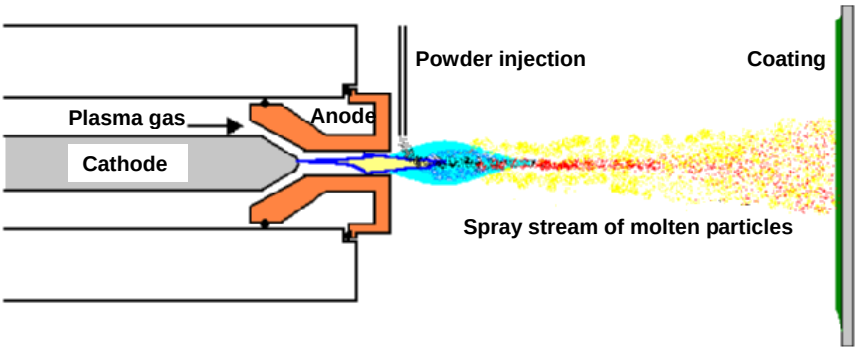

(b) HVOF thermal spray process

Figure 3.2 Schematic diagrams for coating processes: (a) a CVD aluminizing process and (b) a HVOF thermal spray process.

Table 3.2 The notation of specimens.

Coating / Alloy	Uncoated (0)	Pt aluminide (P)	CoNiCrAlY (C)
IN 738 (I)	I0	IP	IC
Rene′ N5 (N)	N0	NP	NC
GTD 111 (G)	G0	GP	GC

Therefore, nine different kinds of specimens were prepared to be investigated as shown in Table 3-2. A notation of a coated specimen consists of two letters. The first letter represents the kind of substrate alloy and the second letter represents the kind of coating. “I”, “N”, and ‘G” in the first letter represents IN 738, Rene′ N5, and GTD 111, respectively. In a similar fashion, “0”, “P”, and “C” in the second letter represents uncoated, platinum aluminide coated and CoNiCrAlY coated specimens, respectively.

In order to have a defined surface condition for all the test specimens, all specimens were grit blasted at 30 psi (=207 kPa) for 45 minutes using 20 μm α-Al_2O_3 particles. This process provided a surface roughness (R_a) of less than 1 μm. The surface roughness changes of platinum aluminide coated GTD 111 can be seen in Figure 3.3 which were taken on an optical microscope and reproduced with an image analyzer. Measured surface roughness using an optical profilometer as a function of grit-blasting time is shown in Figure 3.4. Cross-section micrographs of platinum aluminide coating on GTD 111 before and after 45 minutes grit blasting

at 30 psi (=207 kPa) blowing pressure are shown in Figure 3.5. The figures indicated that grain boundary ridges were removed by grit blasting.

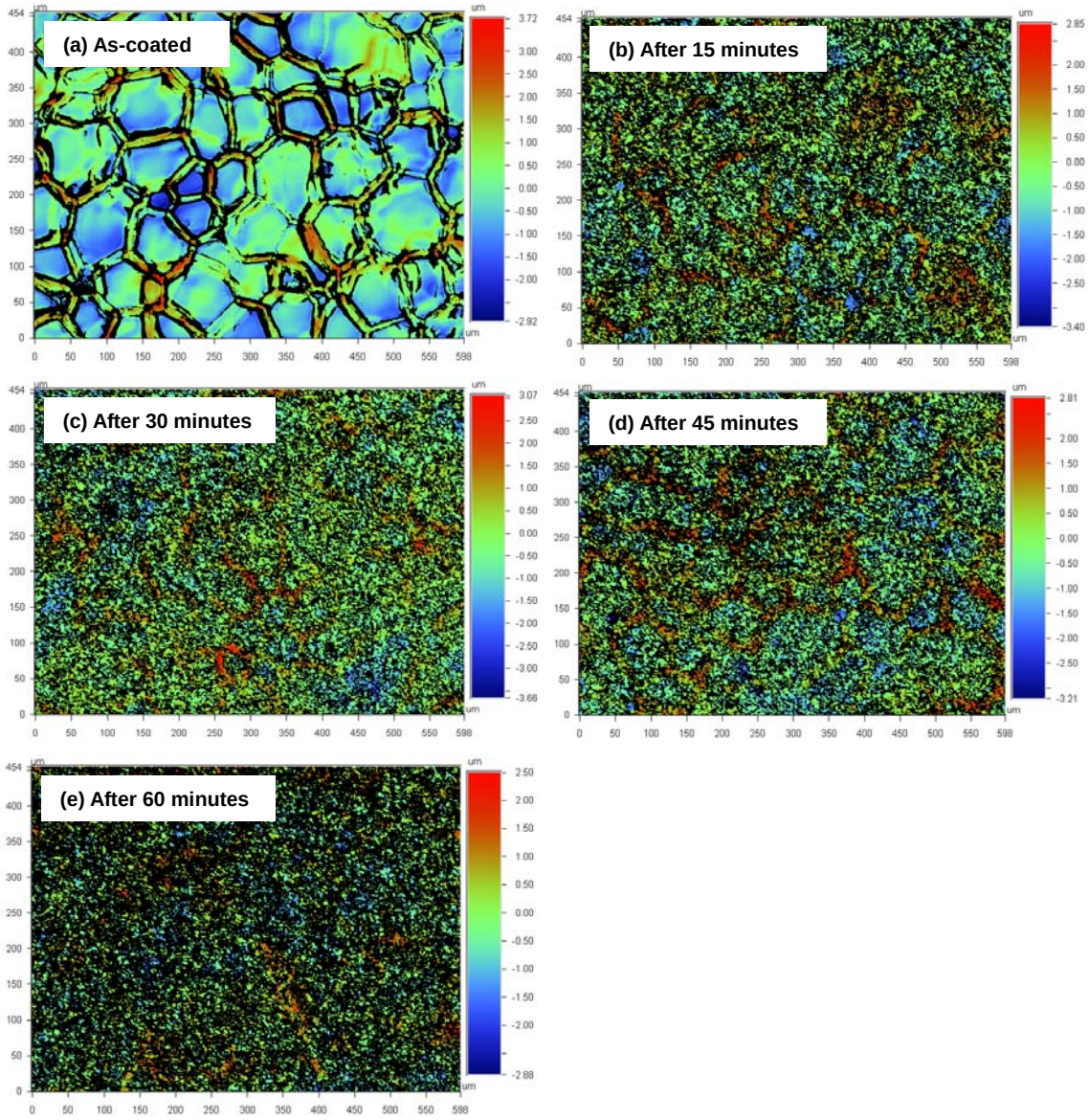

Figure 3.3 Surface micrographs of platinum aluminide coated GTD 111 specimens grit blasted at 30 psi (=207 kPa) using 20 μm α-Al_2O_3 particles as grit blasting time increases. Note that grain boundary ridges vanish as grit blasting time increases.

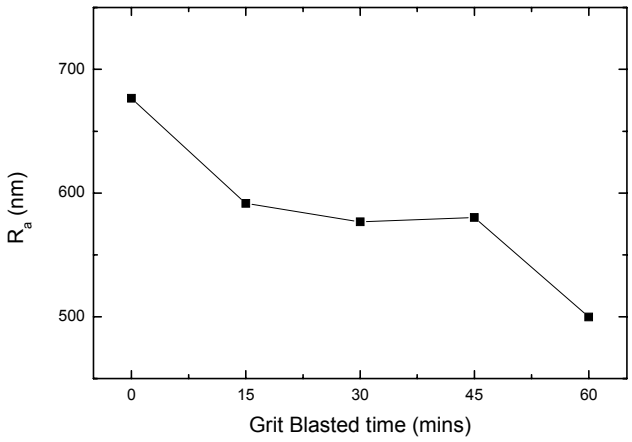

Figure 3.4 R_a values of platinum aluminide coated GTD 111 specimens grit blasted at 30 psi (=207 kPa) using 20 μm α-Al_2O_3 particles as grit blasting time increases.

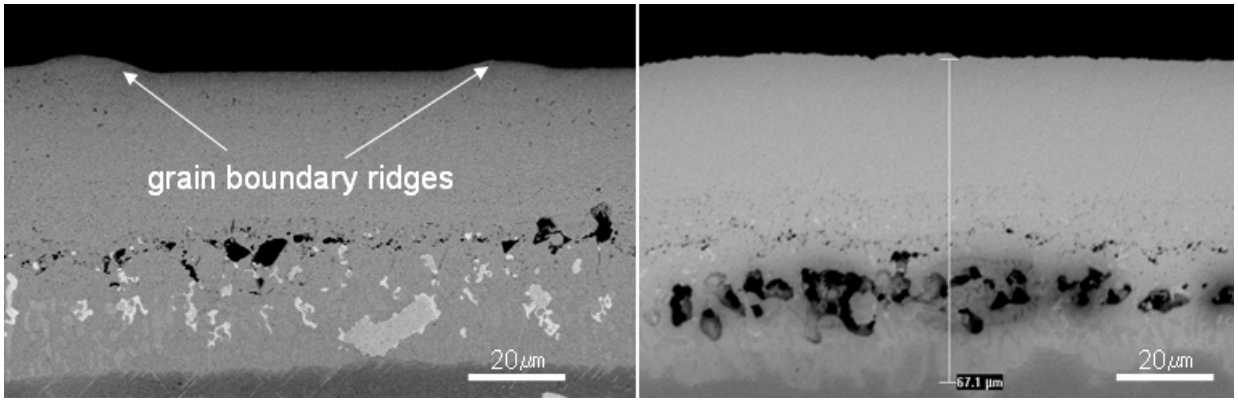

(a) Before grit blasting (b) After grit blasting

Figure 3.5 Cross-section micrographs of platinum aluminide coating on GTD 111 (a) before and (b) after 45 minutes grit blasting at 30 psi (=207 kPa) using 20 μm α-Al_2O_3 particles. Note that grain boundary ridges vanished after grit blasting.

Uncoated specimens were exposed after they were polished and grit blasted. For the coated specimens, platinum aluminide was coated on the grit blasted alloy specimens. To make CoNiCrAlY coated specimens, one side of the platinum aluminide coated specimens was polished to remove the coating and CoNiCrAlY was coated on the side of the polished surface. Then, coated specimens were grit blasted again under the previous grit blasting condition. Surface photographs of nine specimens that were used in this study are presented in Figure 3.6.

Cross-section micrographs of as-coated specimens are also presented in Figures 3.7 and 3.8. The platinum aluminide coating, Figure 3.7, consists of β phase NiAl. The CoNiCrAlY coating, Figure 3.8, contains some aluminum oxide particles and consists of a mixture of aluminum depleted γ phases and aluminum rich β phases as shown in Figure 3.9.

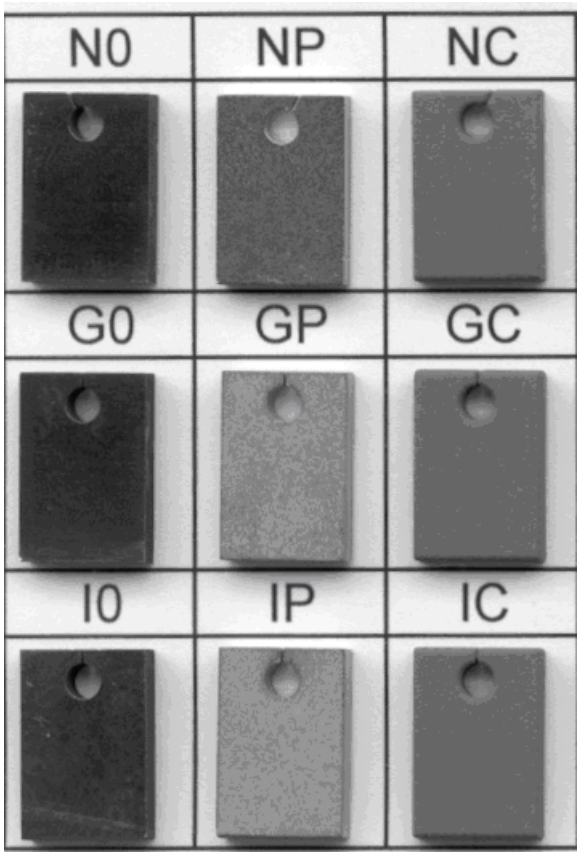

Figure 3.6 Surface photographs of nine as-received specimens that were used in the current study. The dimensions of each specimen are 15×10×3 mm. Notations of specimen ID are indicated in Table 3.2.

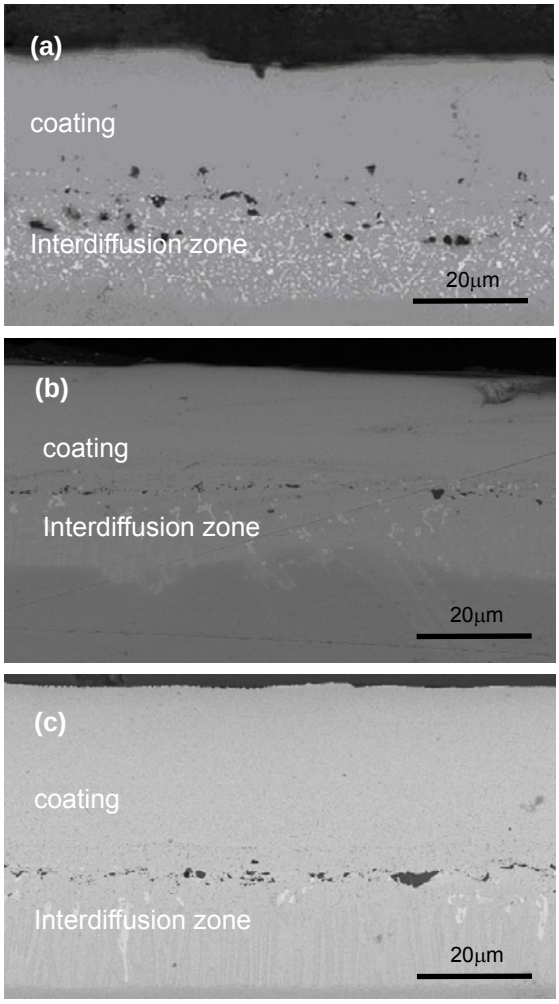

Figure 3.7 Scanning electron micrographs of cross sections of as-processed platinum aluminide coatings on (a) Rene′ N5, (b) GTD 111, and (c) IN 738.

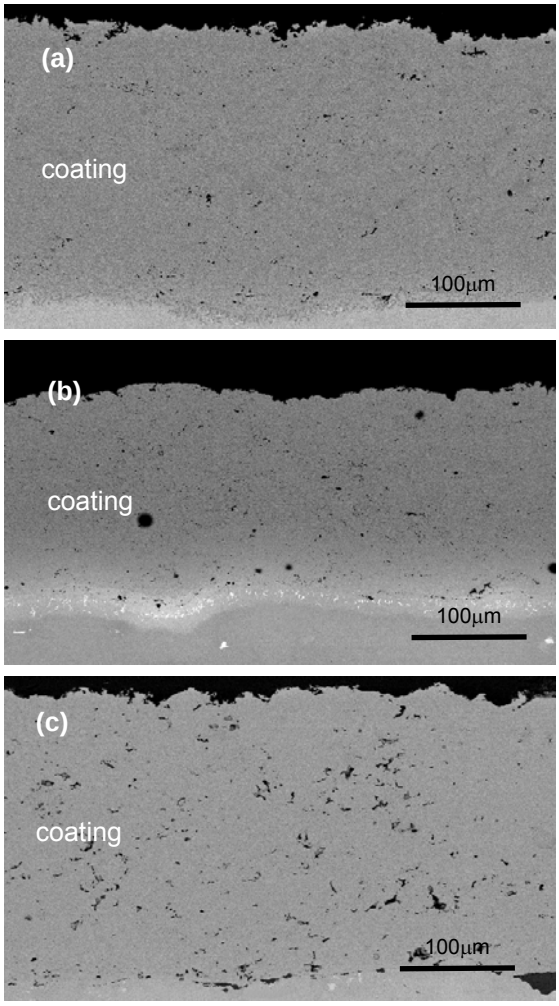

Figure 3.8 Scanning electron micrographs of cross-sections of as-processed CoNiCrAlY coatings on (a) Rene′ N5, (b) GTD 111, and (c) IN 738.

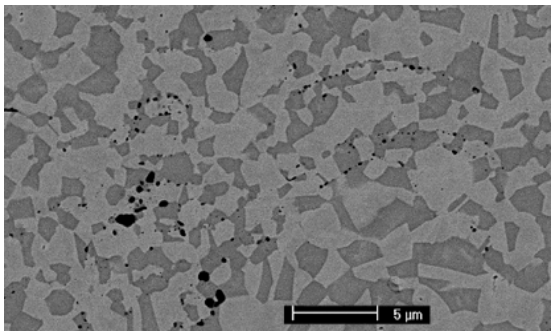

Figure 3.9 A scanning electron micrograph (higher magnification) showing the cross-section of CoNiCrAlY coating on GTD 111. Note that the bright and dark regions represent γ phase (aluminum depleted CoNiCrAlY) and β phase (aluminum rich CoNiCrAlY), respectively. Black particles are aluminum oxides.

3.2.2 Accelerated Cyclic Oxidation Experiment

The cyclic oxidation exposure tests were performed in horizontal tube furnaces with controlled gas environments, as shown in Figure 3.10. These furnaces were used for cyclic exposures in dry as well as in air/water vapor mixtures. All cyclic experiments were done at atmospheric pressure. To establish the wet air environment, extra dry grade tank air (-46^{o}C dew point) was passed through water containers which were kept at a certain temperature to satisfy the desired saturation level. During the experiments, contents of which will be described in the following sections in detail, the partial pressure of water vapor was chosen as 0.1 atm. To establish this environment, the temperature of the water bath was maintained at 46^{o}C. For the dry exposures, the tank air was directly sent to the furnace so that the partial pressure of water vapor is considered to be virtually zero.

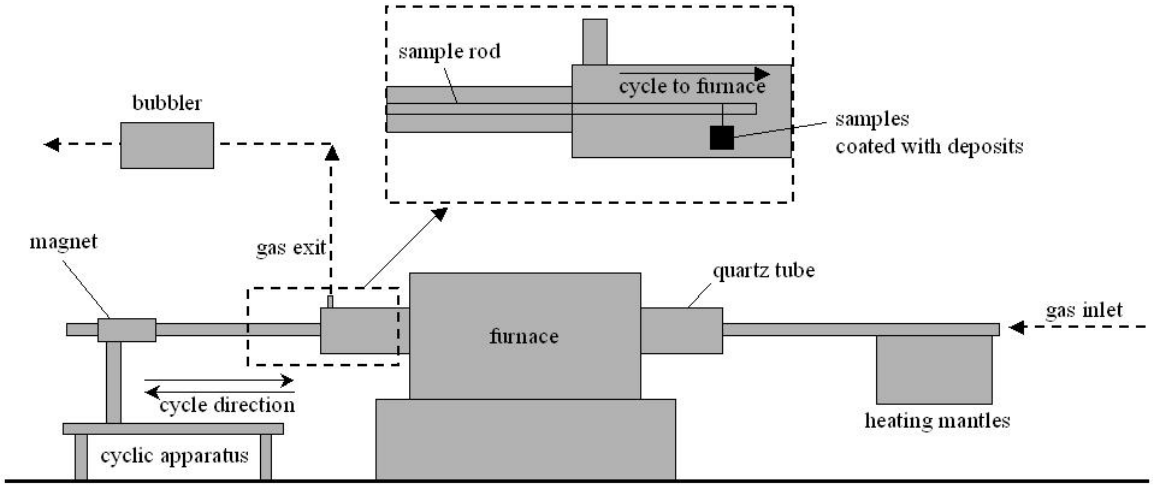

Figure 3.10 Schematic diagram showing the apparatus to cyclically oxidize coupons in gases with defined and controlled amounts of water vapor in air at a total pressure of 1.0 atm.

The cyclic experiments were designed as one hour periods where the specimens were exposed to hot gases for 45 minutes, and then the specimens were moved to the cold zone to be cooled down to lower temperatures (~100^{o}C) for 15 minutes. It took 80 seconds for the specimens to be moved from the hot zone to the cold zone or vice versa. The exposures were interrupted every 20 cycles to measure the specific weight changes of the specimens as a function of time, along with visual examinations of the specimen surfaces. Surface photographs were taken every 20 hours to document the visual examinations. The weight change data were used to document the oxidation kinetics of the systems under investigation. In the initial experiments, the cyclic exposure tests were performed at 750^{o}C, 950^{o}C, and 1150^{o}C. The rest of

the experiments were performed only at the temperature ($T_1 = 950^oC$) which was determined as the best temperature among the above three temperatures to study.

3.3 EXPERIMENTAL PROCEDURES

Under the conditions (D_1 = CaO, T_1 = 950^{o}C) that were determined from the initial experiments described in section 3.1, the main experiments were performed using the following procedures.

(1) Comparison of Uncoated alloys

This is to investigate the effects of CaO deposits on three different uncoated alloys, Rene′ N5, GTD 111, and IN 738. Specimens were cyclically exposed at 950^{o}C with and without CaO deposits both in dry and wet air. Thermogravimetric analyses and microstructural observation via optical and scanning electron microscopy with EDX analysis were used to document the degradation process during exposure. Results were compared with respect to the presence of moisture and CaO deposits.

(2) Comparison of Coated alloys

To study the effects of CaO deposits on coated alloys, two different coatings, platinum modified aluminide and CoNiCrAlY, were applied to three different substrate superalloys, Rene′ N5, GTD 111, and IN 738. Therefore, six specimens, as listed in Table 3.2, were tested in this set of experiments. Also, the effect of substrate alloys on degradation was of concern. Conditions for the experiments were the same as those described in procedure (1)

(3) Effects of CaO on Thermal Barrier Coatings

APS YSZ TBC specimens with and without CaO deposits were isothermally exposed at 950^{o}C in dry air for 200 hours to study the effects of CaO on degradation of APS YSZ TBC specimens. Surface and cross-section micrographs were documented and the element mapping technique via EDX was used to identify the reaction products formed on the surface.

(4) Interactions between CaO and Oxide Scales

Pure Al_2O_3 specimens were placed in an alumina tube filled with CaO powder and isothermally exposed at 950^{o}C in dry air for 200 hours to study the interactions between Al_2O_3 and CaO. Surface and cross-section micrographs were documented and the X-ray diffraction technique was used to identify the phases produced from the reaction. A mechanism to explain CaO-induced degradation on an alumina-forming alloy/coating is proposed at the end of this section. Additionally, the effects of CaO on degradation of chromia-forming alloys/coatings and YSZ TBCs were discussed.

(5) The Effects of Contaminant Level and Water Vapor Pressure

The purpose of this task was to determine the effects of contaminant amount and water vapor partial pressure on the deposit induced degradation. To determine the effects of the amount of

CaO deposits on degradation of chromia-forming superalloys, GTD 111, the amount of CaO deposits was varied. Thermogravimetric analyses and microstructural observation via optical and scanning electron microscopy with EDX technique were used to document the degradation process during exposure.

On the other hand, GTD 111 specimens were exposed with and without CaO deposits in higher water vapor pressure, 0.2 atm. Results were compared to those from procedure (1) which was conducted in dry and wet (0.1 atm water vapor pressure) air.

(6) Effects of Fe_2O_3 and SiO_2 on GTD 111

The effects of Fe_2O_3 and SiO_2, which are other possible deposits in addition to CaO that may form on the turbine hardware, on degradation of GTD 111 were studied.

Conditions for the experiments were the same as those described in procedure (1)

4.0 EXPERIMENTAL RESULTS AND DISCUSSION

4.1 CHARACTERIZATION OF ASH DEPOSITS FROM USE OF SYNGAS

Fragments of deposits have been obtained from the first stage vanes of an electric power generating gas turbine that had used syngas produced from petroleum coke for approximately 16,000 hours. This vane was coated with a Yttria-Stabilized Zirconia (YSZ) TBC. X-ray diffraction and EDS analyses of the fragments showed that the larger particles in these fragments were the ZrO_2 from the TBC. The smaller particles contained Fe, Ni and oxygen as well as some calcium and sulfur, Figure 4.1. The Fe and Ni in these deposits probably come from hardware in the gas turbines and the influence of sulfur on coating degradation has been the subject of numerous investigations.

It was, therefore, decided to examine the influence of CaO and $CaSO_4$ deposits on degradation of alloys and coatings. Since it has also been documented that water vapor can affect the oxidation processes, the experiments with CaO deposits also included dry and wet conditions. Additionally, from the characterization of the ash of another turbine blade exposed with the use of syngas, Fe_2O_3 and SiO_2 were also detected and they may be introduced from rust of the turbine hardware or ingested with air during operation.[76] Therefore, the experiments to study the

effects of Fe_2O_3 and SiO_2 on coated and uncoated GTD 111 specimens were added at the end of the study to determine if such deposits were benign.

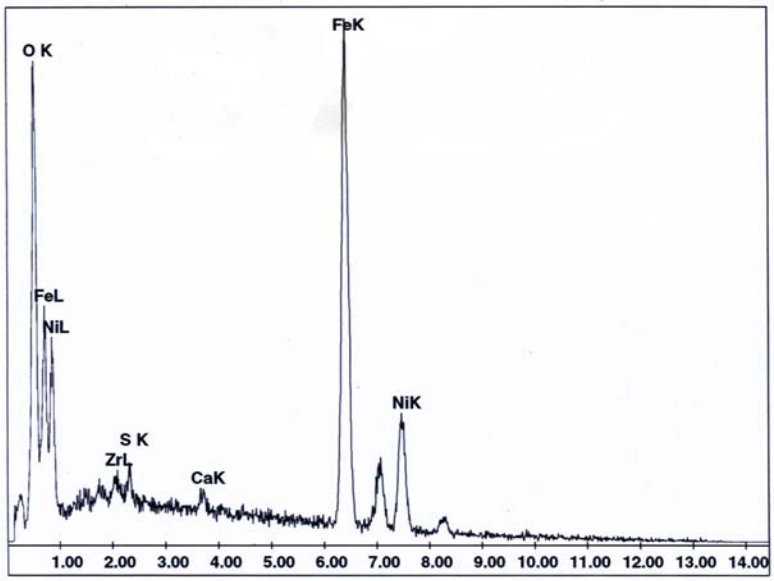

Figure 4.1 EDS analyses obtained from the smaller particles in the ash deposits.

4.2 SELECTION OF TEST CONDITIONS – INITIAL EXPERIMENTS

In this research, it was planned first to determine a set of conditions with which a number of alloys and coatings could be compared. The initial experiments, therefore, involved a limited number of materials but a wide range of test conditions. Platinum aluminide coated Rene′ N5 (NP) specimens were exposed at 750^{o}C, 950^{o}C and 1150^{o}C in a variety of environments with deposits of CaO, $CaSO_4$ and Na_2SO_4. At 750^{o}C, the air contained SO_3 gas at a pressure of about 10^{-4} atm in extra dry air. In order to establish an SO_3 pressure of about 10^{-4} atm, air containing 1000 ppm SO_2 was passed over a platinum catalyst in the tube furnace. In the test with SO_3, the specimens were isothermally exposed at 750^{o}C and these specimens were cycled once every 20 hours when weight change measurements were performed.

At 950^{o}C and 1150^{o}C, the specimens were cyclically exposed every hour in gas environments containing extra dry air and air with 0.1 atm partial pressure of water vapor. For each coated alloy, sixteen specimens were prepared. Four of those were used as ‘no deposit’ specimens and the rest of the specimens had a deposit of CaO, $CaSO_4$ or Na_2SO_4 on their surfaces.

Table 4.1 Summary of test conditions that were used in initial experiments.

Index	Temperature	Atmosphere	Deposits
1	750°C	Dry air + SO_3	No deposit
2			Na_2SO_4
3			CaO
4			$CaSO_4$
5	950°C	Dry air	No deposit
6			Na_2SO_4
7			CaO
8			$CaSO_4$
9		Wet air	No deposit
10			Na_2SO_4
11			CaO
12			$CaSO_4$
13	1150°C	Dry air	No deposit
14			Na_2SO_4
15			CaO
16			$CaSO_4$
17		Wet air	No deposit
18			Na_2SO_4
19			CaO
20			$CaSO_4$

After grit blasting in the sample preparation procedure, the specimens were rinsed in an ultrasonic water bath and 1.0 ± 0.1 mg/cm^2 of CaO, $CaSO_4$ or Na_2SO_4 was deposited on the specimens using an air spray of aqueous solutions containing these materials. Duplicate specimens were also exposed for further analyses and to show the reproducibility of the data. Specimens with no deposit, CaO, $CaSO_4$ and Na_2SO_4 deposits were tested concurrently in a cyclic oxidation experimental apparatus (45 minutes in hot zone and 15 minutes in cold zone) described in section 3.2.2. Test conditions used in these experiments are summarized in Table 4-1. The weight changes of specimens were determined after every 20 cycles. Prior to these measurements, the specimens were washed in an ultrasonic water bath to remove the deposits. After the weight change measurements, the deposits were applied again.

Based on the results from such experiments, a temperature (T_1 = 950^{o}C) and a deposit (D_1 = 1.0 ± 0.1 mg/cm^2 of CaO) were selected to compare the corrosion characteristics of all of the alloys and coatings. Results from these initial experiments will be presented in the following sections.

4.2.1 Exposure Tests at 750°C in Dry Air Containing SO_3 Gas

The weight change versus time measurements for platinum aluminide coated Rene′ N5 specimens with deposits of CaO, $CaSO_4$ and Na_2SO_4 as well as specimens with no deposit are presented in Figure 4.2. The specimens with Na_2SO_4 deposits exhibit relatively large weight gains followed by weight losses due to spallation of the corrosion products as shown in Figure 4.3. This attack was so severe that the coating had been completely penetrated and the substrate had been attacked.

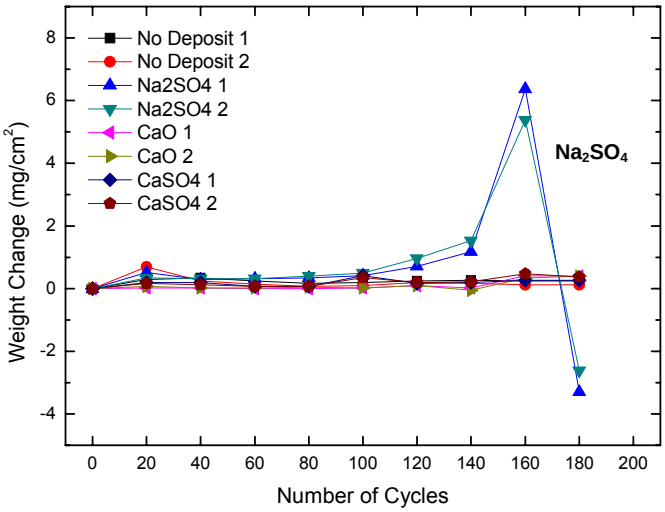

Figure 4.2 Weight change versus time measurements for platinum aluminide coated Rene′ N5 specimens with different deposits exposed at 750°C in air containing 1000 ppm SO_2.

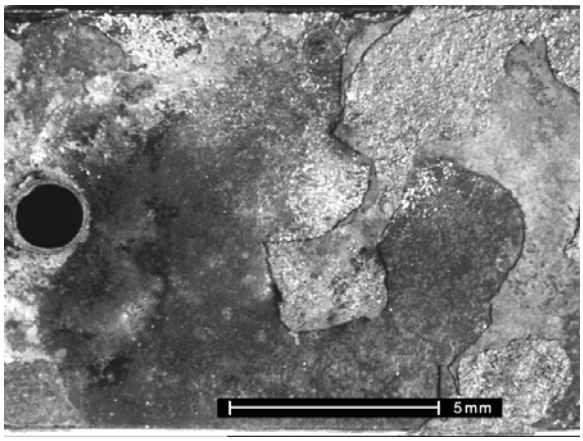

Figure 4.3 Stereographic micrograph of platinum aluminide coated Rene′ N5 (NP) specimen with Na_2SO_4 deposition after 200 hours exposure at 750°C in air containing 1000 ppm SO_2.

Figure 4.4 shows scanning electron micrographs of exposed specimens of platinum aluminide coatings on Rene′ N5 (NP) with Na_2SO_4 deposit after 180 hours. The figures show (a) typical low temperature hot corrosion (Type II) and (b) severely degraded coating, respectively. All of the other specimens (no deposit, CaO and $CaSO_4$ deposits) exhibited very little attack as shown in Figure 4.5 (a), (c) and (d).

The experiments at 750^{o}C were performed to determine how the deposits (i.e. CaO and $CaSO_4$) affected coating degradation under low temperature hot corrosion conditions (Type II hot corrosion). As expected, the Na_2SO_4 in the presence of SO_3 caused severe Type II hot corrosion attack whereas the other deposits did not cause any degradation. These results show that testing at 750^{o}C in gases with SO_3 is not realistic for deposits that may develop in gas turbines using syngas because the attack is induced by Na_2SO_4 only.

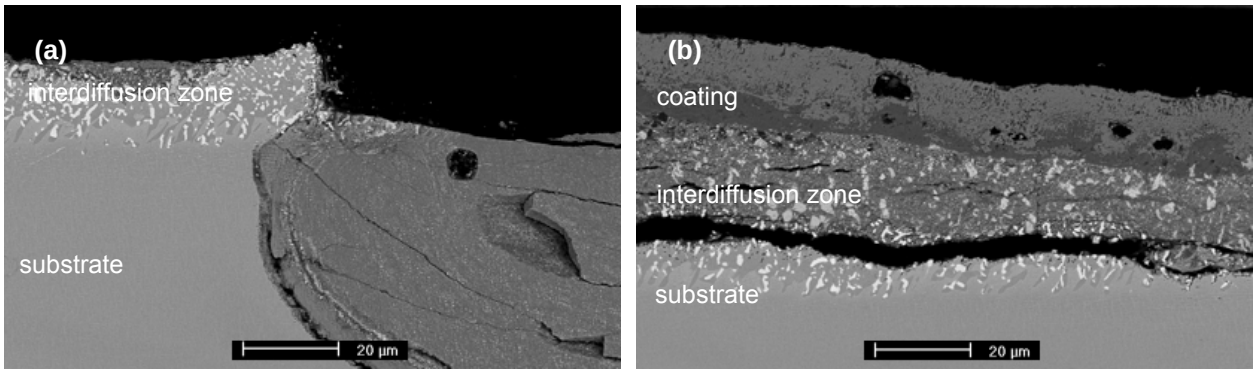

Figure 4.4 Scanning electron micrographs of exposed specimens of platinum aluminide coatings on Rene′ N5 (NP) with Na_2SO_4 deposit at 750°C in a gas mixture with SO_3 after 180 hours. Figures show (a) low temperature hot corrosion and (b) severely degraded coating.

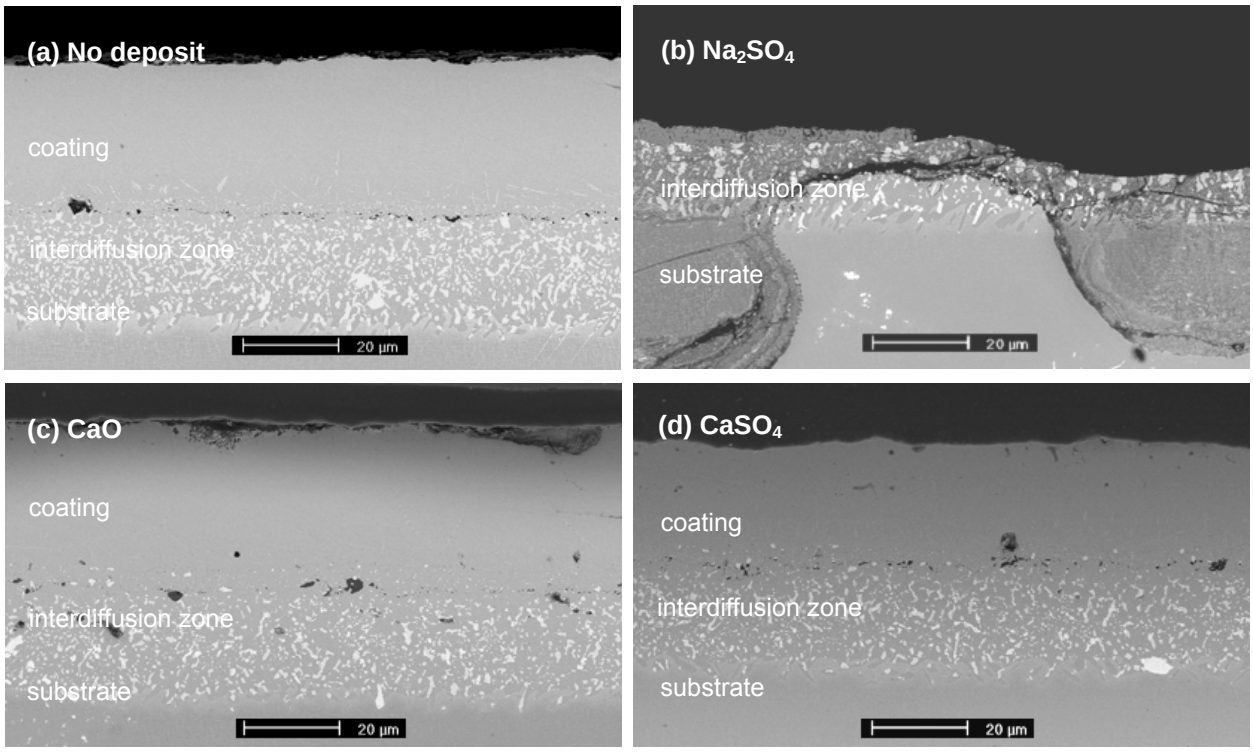

Figure 4.5 Scanning electron micrographs of platinum aluminide coatings on Rene′ N5 (NP) after 180 hours of exposure at 750°C in air with SO_3. These specimens exhibited very little attack except in the case of the specimen with Na_2SO_4 deposit.

4.2.2 Exposure Tests at 950°C in Dry and Wet Air

Weight change versus time measurements for cyclic oxidation at 950°C of the platinum aluminide coating on Rene′ N5 (NP) are presented in Figure 4.6 for dry air and in Figure 4.7 for air containing a water vapor pressure of 0.1 atm. The weight change versus time measurements show reasonably good reproducibility between duplicate test specimens. The specimens with deposits of CaO have larger weight losses than the specimens with other deposits. Also, the weight losses are larger in dry air compared to wet air. Compared to the weight changes of the specimens with no deposit, the specimens with Na_2SO_4 deposits have slightly larger weight gains in both dry and wet air, whereas the specimens with $CaSO_4$ deposits have smaller weight losses.

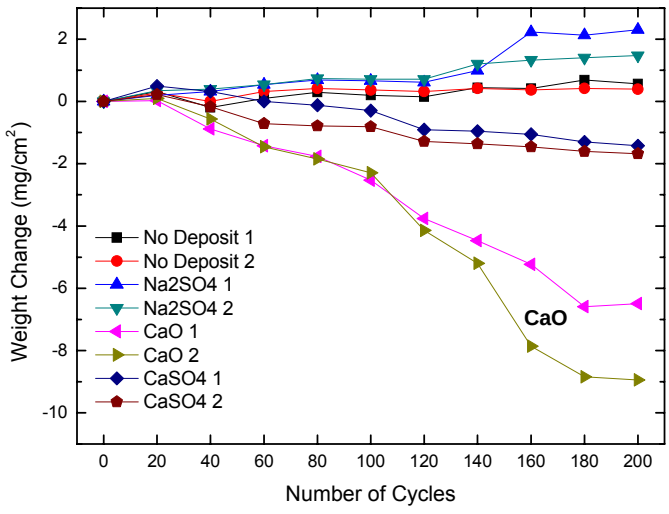

Figure 4.6 Weight change versus time measurements for platinum aluminide coated Rene′ N5 (NP) specimens with different deposits exposed at 950°C in dry air.

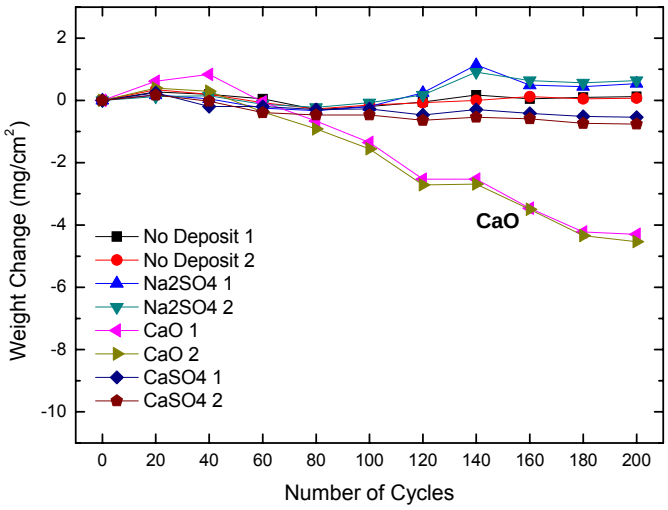

Figure 4.7 Weight change versus time measurements for platinum aluminide coated Rene′ N5 (NP) specimens with different deposits exposed at 950^{o}C in wet air.

Metallographic examination of cross-sections of the exposed specimens was performed after 200 cycles using the scanning electron microscope (SEM). This initial examination was performed to show the general condition of the coatings. SEM micrographs of platinum aluminide coatings on Rene′ N5 (NP) with deposits exposed at 950°C after 200 hours in dry and wet air are presented in Figure 4.8 and Figure 4.9, respectively. Substantial attack is evident on the coatings with deposits, but the most severe degradation has occurred with the specimens with CaO deposits. In the case of the coatings with this deposit, more attack is evident in wet air. In the case of the Na_2SO_4 and $CaSO_4$ deposits, the attack appears to be more severe in wet compared to dry air.

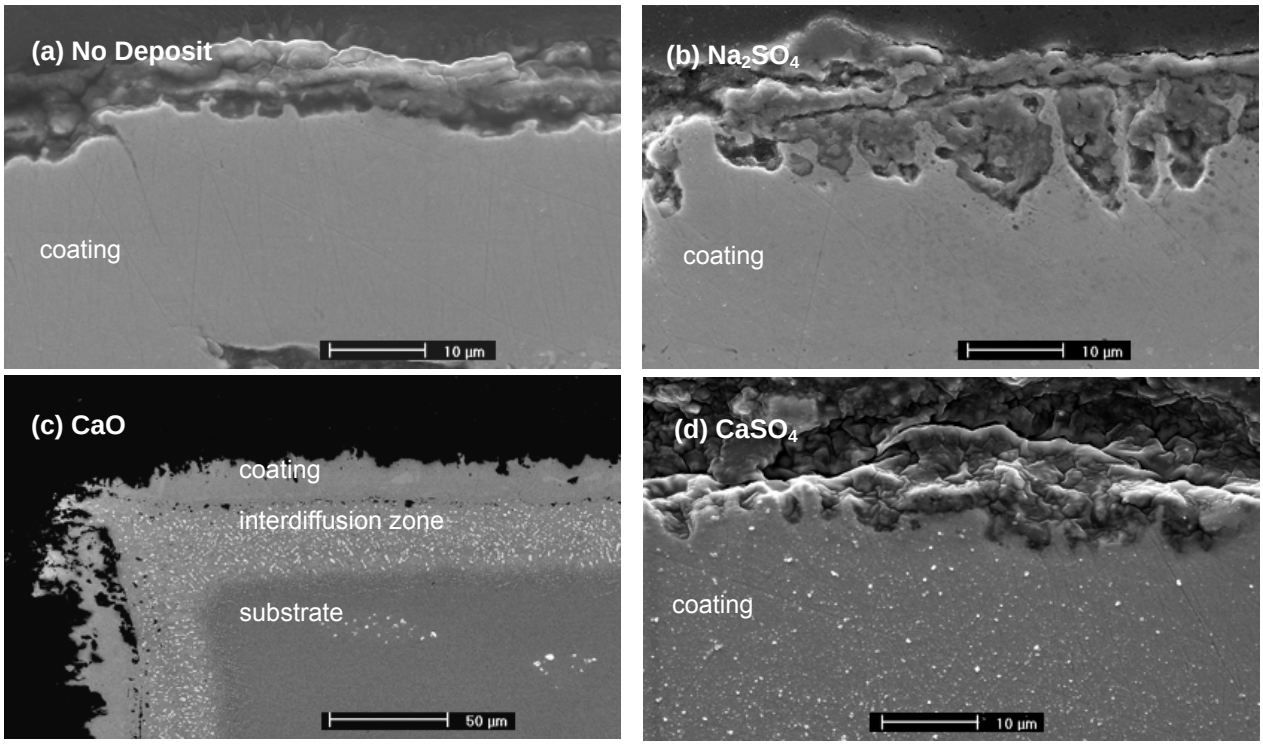

Figure 4.8 Scanning electron micrographs of platinum aluminide coatings on Rene′ N5 (NP) exposed at 950°C after 200 hours in dry air with (a) no deposit, (b) Na_2SO_4, (c) CaO, and (d) $CaSO_4$, respectively.

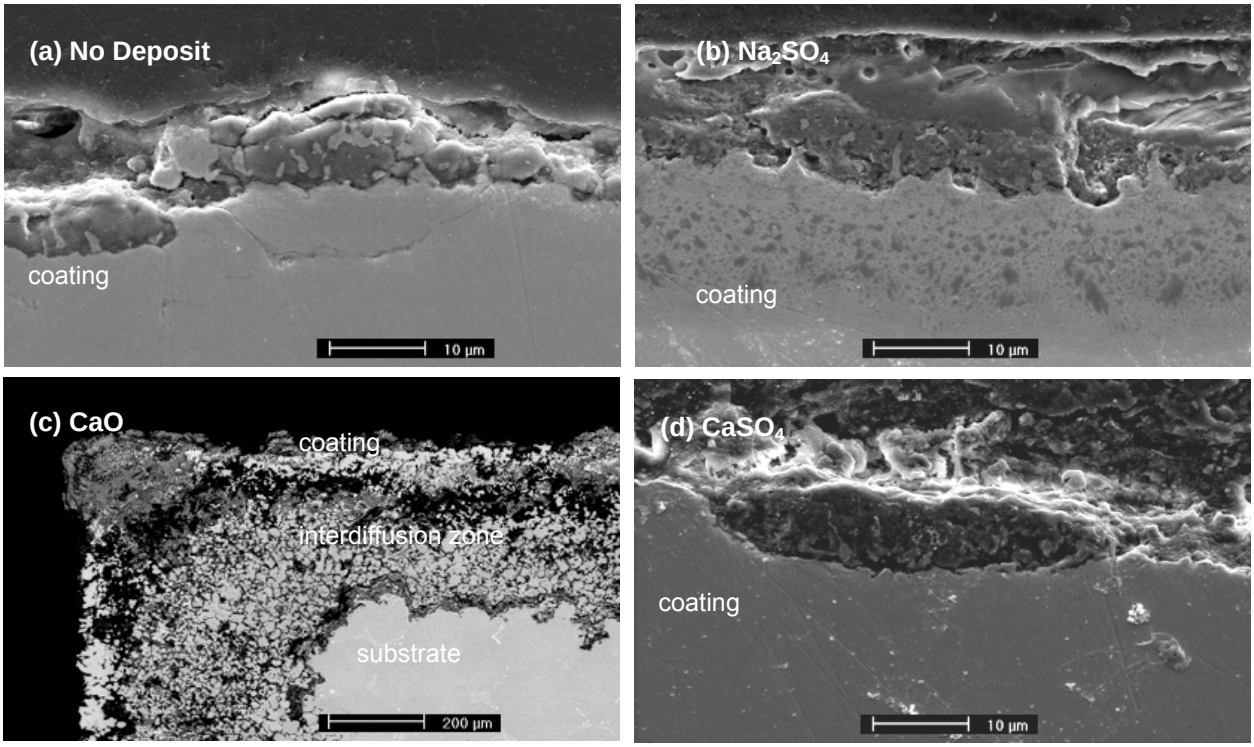

Figure 4.9. Scanning electron micrographs of platinum aluminide coatings on Rene′ N5 (NP) exposed at 950°C after 200 hours in wet air with (a) no deposit, (b) Na_2SO_4, (c) CaO, and (d) $CaSO_4$, respectively.

4.2.3 Exposure Tests at 1150°C in Dry and Wet Air

Weight change versus time measurements for cyclic oxidation at 1150°C of platinum aluminide coatings on Rene′ N5 are presented in Figure 4.10 for dry air and Figure 4.11 for wet air. The weight changes for CaO deposits in both dry and wet air are larger than those for the other deposits.

Scanning electron micrographs of the exposed specimens in dry air are presented in Figures 4.12. In dry air, the CaO deposits have caused more degradation than the other deposits. This attack induced by the CaO results in localized areas of preferential attack (arrows in Figure 4.12 (c)) and the coating thickness has been reduced. A protective oxide has been developed on the coatings with the other deposits as well as on the coating with no deposit, however this latter specimen does exhibit a scale with rather large variations in thickness.

Scanning electron micrographs of the coatings exposed at 1150°C in wet air are presented in Figure 4.13. As in the case of dry air, the CaO deposits have caused more attack. The coating with this deposit has protrusions (arrows in Figure 4.12 (c)) that extend almost to the substrate. The Na_2SO_4 and $CaSO_4$ deposits have also caused degradation where the attack is more severe with the $CaSO_4$ deposits and the attack consists of protrusions extending into the coating as in the case of the CaO deposits.

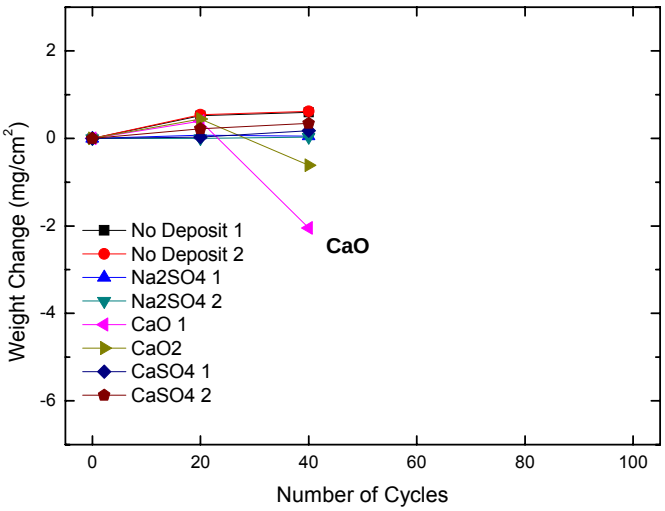

Figure 4.10 Weight change versus time measurements for platinum aluminide coated Rene′ N5 (NP) specimens with different deposits exposed at 1150^{o}C in dry air.

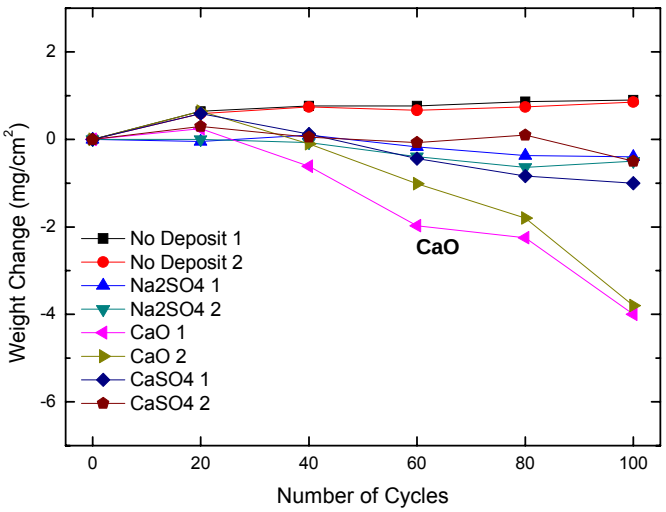

Figure 4.11 Weight change versus time measurements for platinum aluminide coated Rene′ N5 (NP) specimens with different deposits exposed at 1150^{o}C in wet air.

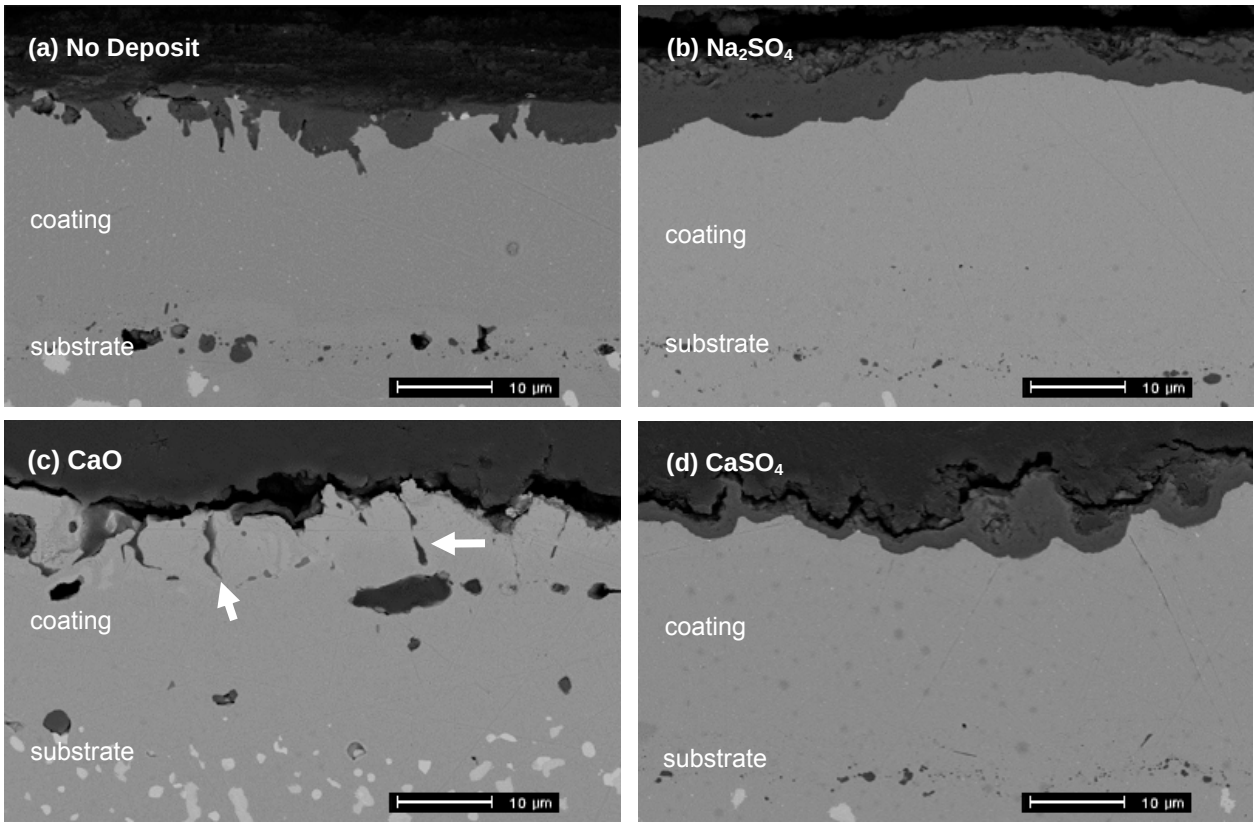

Figure 4.12 Scanning electron micrographs of platinum aluminide coatings on Rene′ N5 (NP) with (a) no deposit, (b) Na_2SO_4, (c) CaO, and (d) $CaSO_4$ deposits exposed at 1150°C for 40 hours in dry air. Note that arrows in (c) indicate preferential attack.

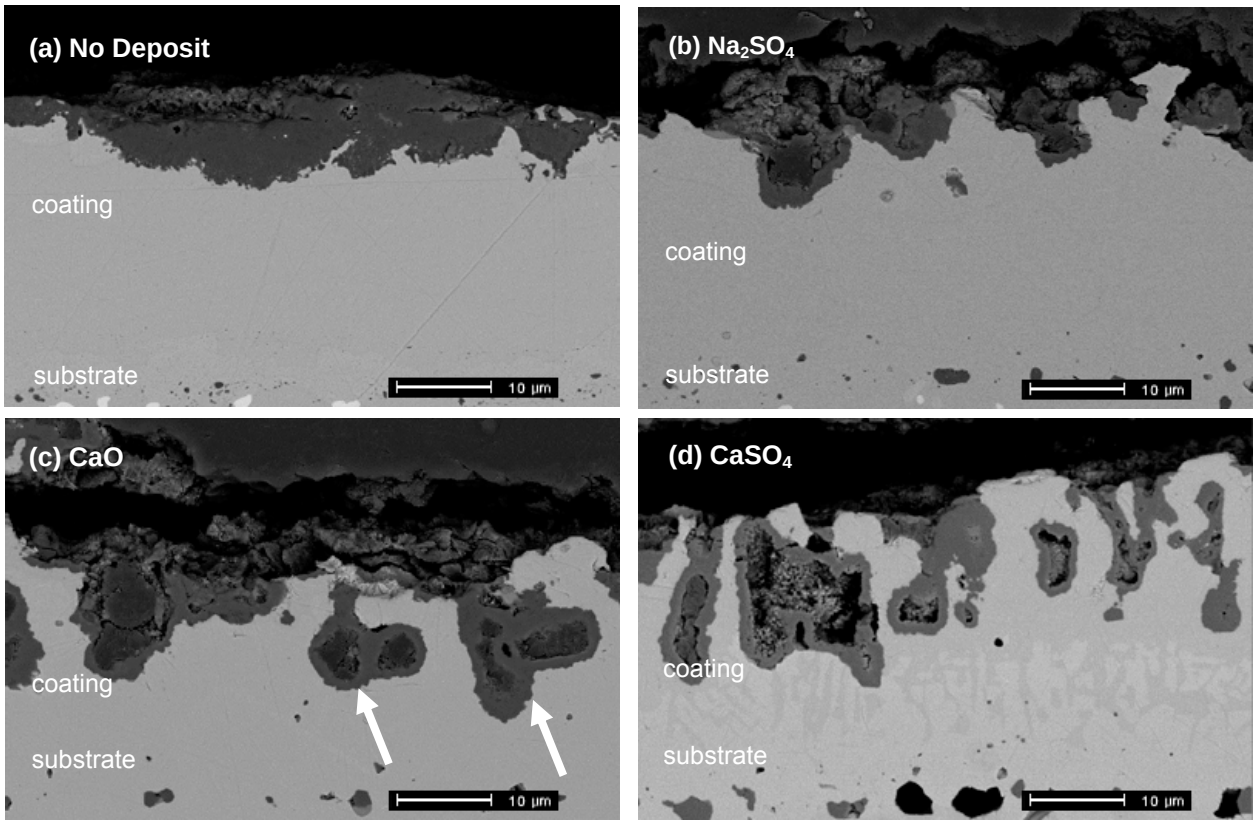

Figure 4.13 Scanning electron micrographs of platinum aluminide coatings on Rene′ N5 (NP) with (a) no deposit, (b) Na_2SO_4, (c) CaO, and (d) $CaSO_4$ deposits exposed at 1150°C for 100 hours in wet air. Note that arrows in (c) indicate protrusions.

4.2.4 Summary: Selection of Test Conditions

Based on the results that have been obtained from the oxidation tests performed at 750°C, 950°C and 1150°C using deposits of CaO, $CaSO_4$ and Na_2SO_4, it is clear that coating degradation has occurred with all of the deposits at 950°C and 1150°C. At 750°C, however, the attack was induced by Na_2SO_4 only. The results obtained at 750°C show that the attack is that of low temperature hot corrosion (Type II) and such conditions should not be used for the testing to be performed in the further experiments where the resistance of alloys and coatings on alloys are to be compared.

The test that was performed at 1150°C showed that CaO deposits caused more attack than deposits of Na_2SO_4 or $CaSO_4$. However, the amount of degradation was severe due to the high temperature and it is believed that the further experiments should not be performed at this temperature.

The testing at 950°C showed that all of the deposits caused increased degradation compared to the coatings with no deposit, but CaO deposits caused the most severe degradation. CaO deposits will be used to compare the behavior of the alloys and coatings in the following experiments. In most cases, the degradation induced by deposits was usually more severe in wet

air compared to dry air. In a few cases, however, the specimens exposed in dry air showed comparable attack to that in wet air.

Accordingly, 950^{o}C for T_1 and CaO deposits for D_1 were selected as the best test conditions for the further experiments to investigate the effect of deposits on different coatings and substrate alloys. The effects of water vapor on the degradation process were examined in further experiments where CaO contaminant/moisture limits were investigated.

4.3 COMPARISON OF ALLOYS AND COATINGS

After the appropriate test conditions were selected in section 4.1, the alloys and coated alloys described in Table 3-2 were exposed under these conditions. In particular, the degradation of René N5, GTD 111 and IN 738, and these alloys with platinum-modified aluminide and CoNiCrAlY coatings were compared upon exposure to CaO deposits at 950˚C in dry and wet air. The results obtained from these tests are presented in the following sections.

4.3.1 Comparison of Uncoated Alloys

4.3.1.1 With No Deposit in Dry and Wet Air - Weight change versus time measurements for IN 738, GTD 111 and René N5 in dry and wet air are presented in Figure 4.14. The weight changes for GTD 111 and IN 738 are similar whereas those for René N5 are significantly smaller. This is expected because René N5 develops a thin α-Al_2O_3 scale whereas IN 738 and GTD 111 are Cr_2O_3 formers. The weight change results in wet air are not much different from those in dry air. GTD 111 and IN 738 have slightly larger weight increases in wet air compared to dry air. The surface photographs of the specimens after exposure in dry and wet air are shown in Figure 4.15. There is no substantial difference between any of the specimens.

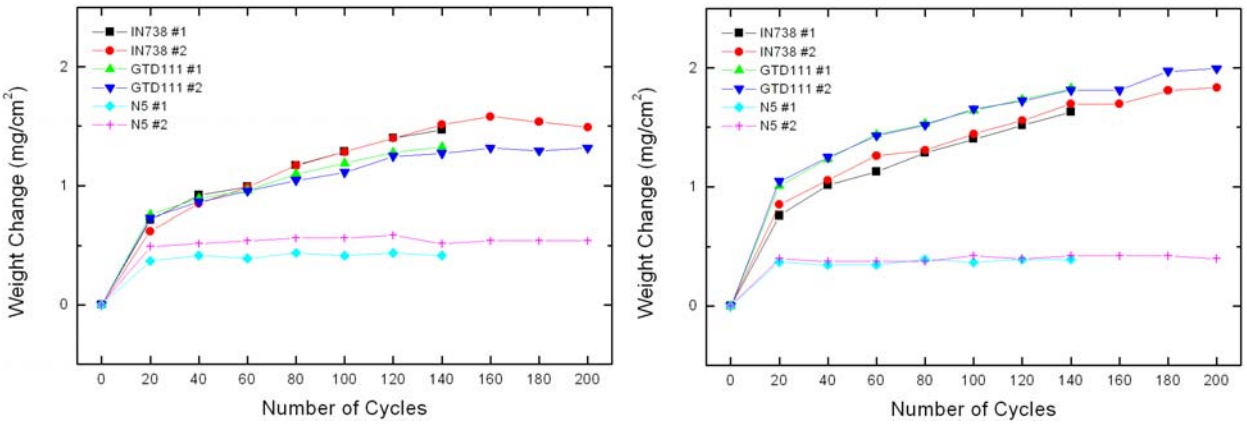

(a) In dry air (b) In wet air

Figure 4.14 Weight Change versus time measurements for the cyclic oxidation (1 cycle consists of 45 minutes in the hot zone and 15 minutes in the cold zone) of René N5, GTD 111, and IN 738 at 950°C in (a) dry and (b) wet (p_{H2O} = 0.1 atm) air.

(a) After 120 hours exposure in dry air

(b) After 80 hours exposure in wet air

Figure 4.15 Surface photographs showing the surf aces of coupon specimens after cyclic oxidation at 950°C in dry and wet (P_{H2O} = 0.1 atm) air.

Scanning electron micrographs of cross-sections of René N5 (N0), GTD 111 (G0), and IN 738 (I0) after 140 hours of cyclic oxidation exposure at 950°C in dry air are presented in Figures 4.16. It can be seen that a very thin oxide scale, which is predominantly α-Al_2O_3, has developed on René N5 in Figure 4.16 (a), whereas thicker scales of Cr_2O_3 have formed on both GTD 111 and IN 738 in Figures 4.16 (b) and (c), respectively. Subscales were also evident in the GTD 111 and IN 738 alloys. The subscales adjacent to the external oxide were aluminum rich and the subscales deeper into the alloy were titanium nitrides. The metallographic results obtained from the exposed specimens in dry air are consistent with weight change versus time measurements presented in Figure 4.14.

Cross-sections of the René N5, GTD 111 and IN 738 after exposure for 140 hours at 950°C in wet air are presented in Figures 4.17. The scale thickness on René N5 varies somewhat in Figure 4.17 (a), but an external α-Al_2O_3 scale has been formed. Particles of oxide, predominantly α-Al_2O_3, extend into the alloy, but the frequency of these particles is much less than that in dry air in Figure 4.16 (a). On GTD 111, an external scale of Cr_2O_3 has formed as shown in Figure 4.17 (b), and internal zones of α-Al_2O_3 and titanium nitrides have been developed.

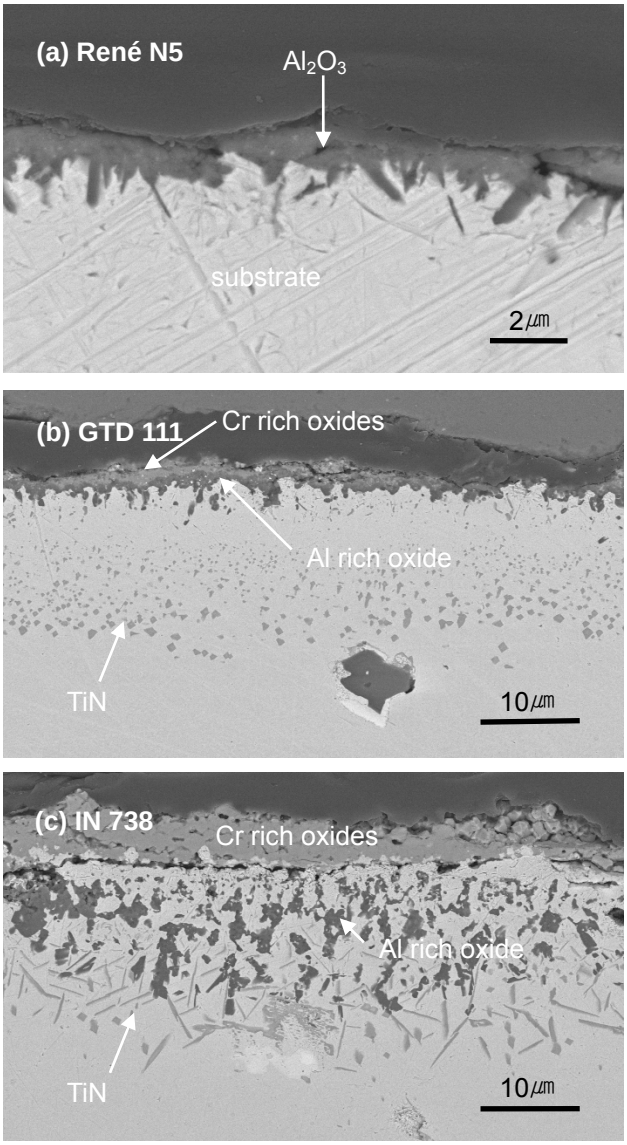

Figure 4.16 Scanning electron micrographs (cross-sectional view) of (a) René N5, (b) GTD 111, and (c) IN 738 after 140 hours of cyclic oxidation at 950^{o}C in dry air.

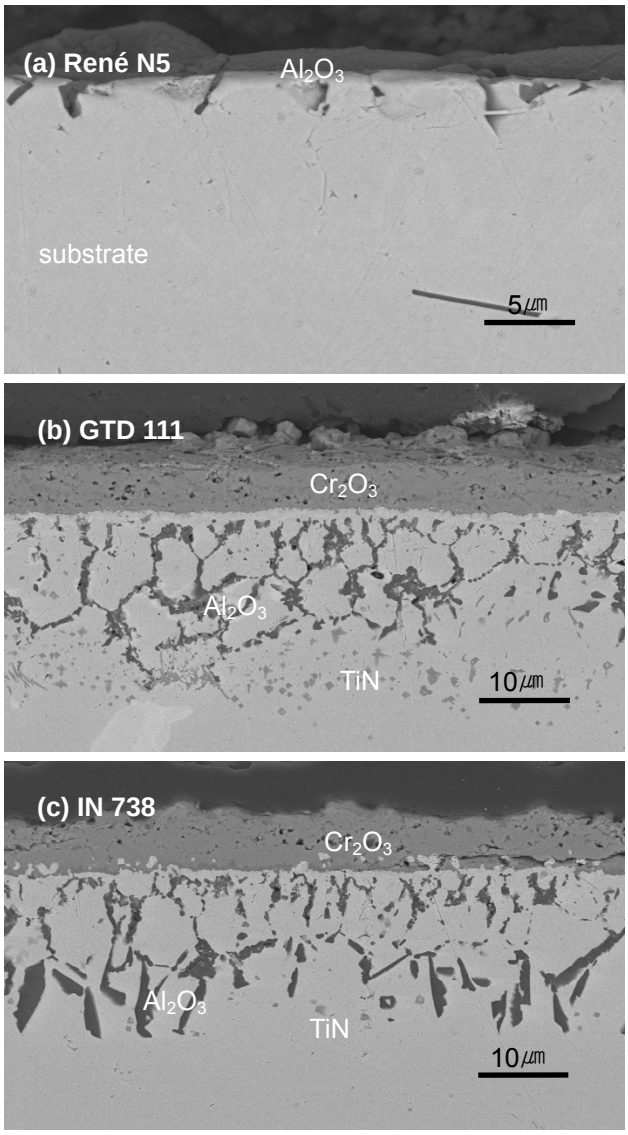

Figure 4.17 Scanning electron micrographs (cross-sectional view) of (a) René N5, (b) GTD 111, and (c) IN 738 after 140 hours of cyclic oxidation at 950^{o}C in wet air.

Upon comparing exposure of this alloy to that in dry air in Figure 4.16 (b), the α-Al_2O_3 is beginning to develop continuity beneath the Cr_2O_3 scale whereas, in wet air, no such continuity is evident and the internal oxide appears to be developing along alloy grain boundaries. The oxides formed on IN 738, Figure 4.17 (c), are similar to those on GTD 111, Figure 4.17 (b), but there appear to be fewer nitrides. In wet air, an external Cr_2O_3 scale has been formed on IN 738 and the internal oxides appear to be forming along alloy grain boundaries similar to GTD 111.

The thicknesses of the internal zones of oxides and nitrides are not substantially different. The major difference is that for all three alloys the internal oxides appear to have formed at special locations in wet air. These special locations appear to be alloy grain boundaries in GTD 111 and IN 738, but the locations in single-crystal René N5 have not been defined. The thicknesses of the nitride zones appear to be smaller in wet air. It is not uncommon to observe internal nitrides when alloys are cyclically oxidized in air. Metallic oxides are usually more stable than metallic nitrides, but during oxidation the oxygen is consumed in forming the external and internal oxide scale and if the nitrogen can enter into the alloy, internal nitrides can be formed.

4.3.1.2 With CaO Deposits in Dry and Wet Air - Weight change versus time measurements for René N5, GTD 111 and IN 738 exposed with and without CaO deposits in dry air are presented in Figures 4.18 (a) and (b), respectively. The CaO deposits caused increased weight gains for all three alloys compared to the specimens with no deposit. The surface photographs of these alloy specimens after 80 hours exposure are presented in Figure 4.19 before and after removing the deposits. The cleaned specimens do not exhibit substantial differences between the three alloys.

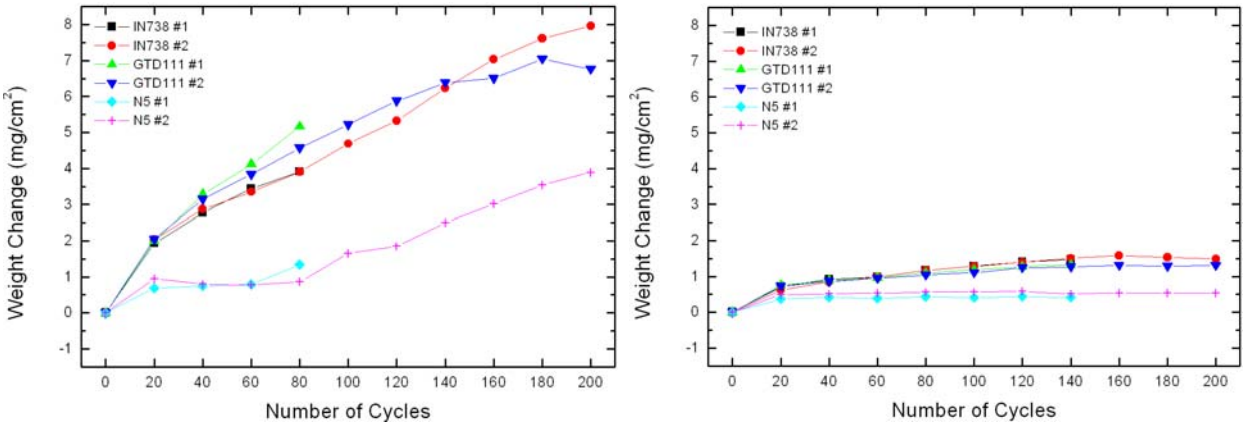

(a) With CaO deposits in dry air (b) With no deposit in dry air

Figure 4.18 Comparison of weight change versus time measurements for René N5, GTD 111, and IN 738 exposed at 950^{o}C in dry air (a) with and (b) without CaO deposits.

(a) Before cleaning

(b) After cleaning

Figure 4.19 Surface photographs of IN 738, GTD 111, and René N5 after 80 hours of cyclic oxidation at 950°C in dry air with CaO deposits (a) before and (b) after cleaning.

Cross-section micrographs of René N5, GTD 111 and IN 738 after exposure for 80 hours of cyclic oxidation at 950°C with CaO deposits are presented in Figures 4.20. In the case of René N5, a thick oxide scale has been formed, Figure 4.20 (a), which was very much thicker than that which formed on this alloy without the deposit, Figure 4.16 (a). Cr_2O_3 and NiO were present at the top of the scale and a small amount of Al_2O_3 was evident in the substrate alloy. The section through GTD 111 is presented in Figure 4.20 (b) where an external scale of Cr_2O_3 and internal oxides and nitrides are evident. The Cr_2O_3 scale appears thicker on the specimen with CaO and

the Al_2O_3 is more discontinuous. A cross-section of IN 738 after exposure for 80 hours in dry air with CaO deposits is shown in Figure 4.20 (c). As for GTD 111, the external scale appears to be thicker than that which formed on this alloy with no deposits. Internal oxide particles and particles of nitrides are also evident. It is clear that, for all three alloys, there was more degradation when CaO was present on the surfaces of the alloys.

Weight change versus time measurements for René N5, GTD 111, and IN 738 exposed with CaO deposits in wet air are presented in Figure 4.21 where results are also presented for exposures of these alloys in dry air with CaO deposits. The weight changes are smaller in wet air but cracking and spalling of oxide may be occurring as indicated by the negative weight change values for René N5. In Figure 4.22, weight change measurements are compared for these alloys with and without CaO deposits for exposure in wet air. The data for CaO deposits suggest cracking and spalling of oxide scales with substantial attack.

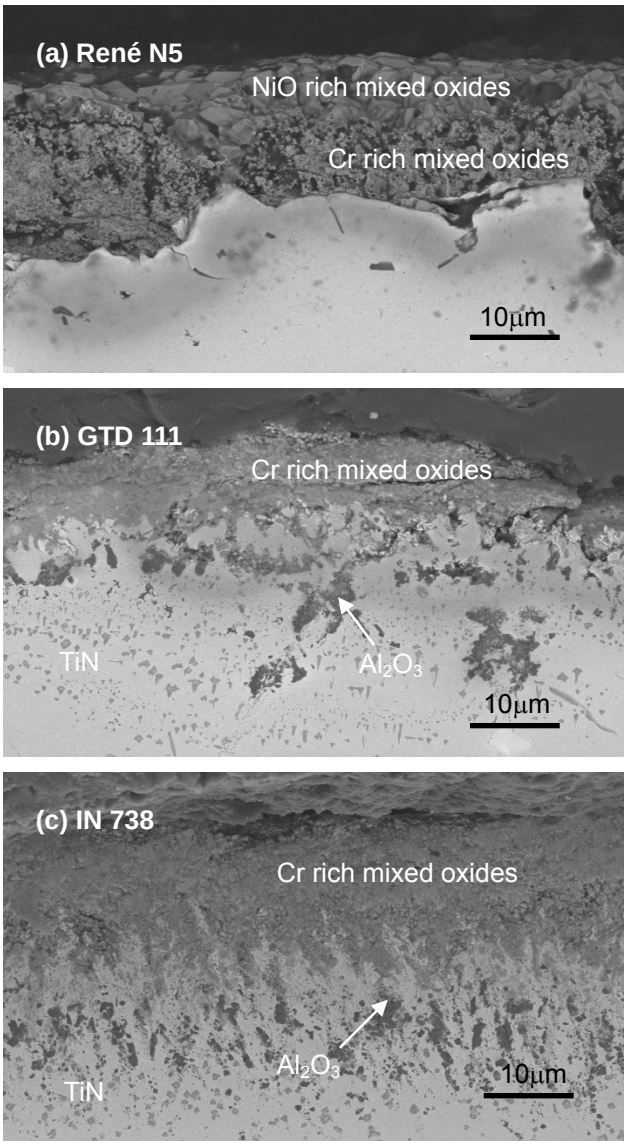

Figure 4.20 Cross-section micrographs of (a) René N5, (b) GTD 111, and (c) IN 738 after 80 hours of exposure at 950°C in dry air with CaO deposits.

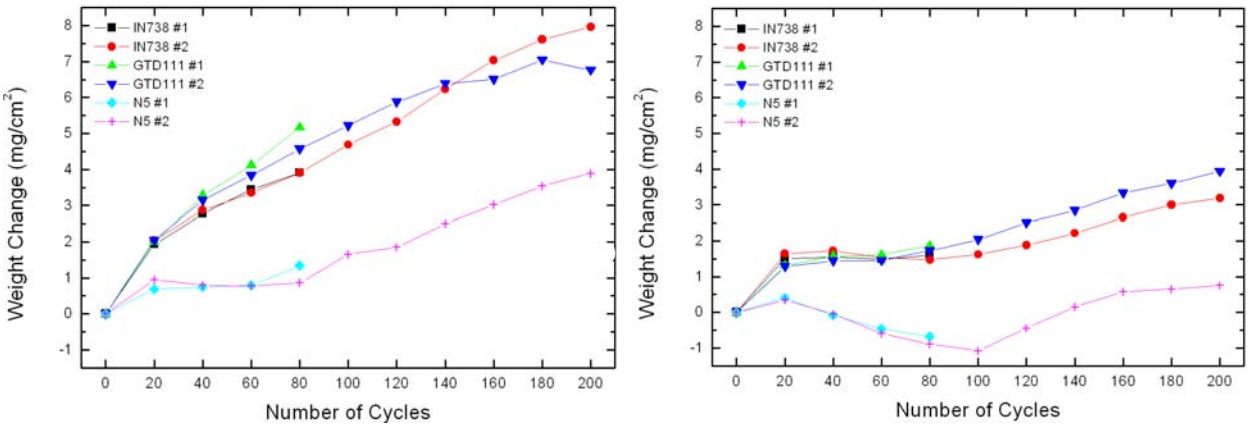

(a) With CaO deposits in dry air (b) With CaO deposits in wet air

Figure 4.21 Weight change measurements for the cyclic oxidation of René N5, GTD 111, and IN 738 with CaO deposits at 950^{o}C in (a) dry and (b) wet air.

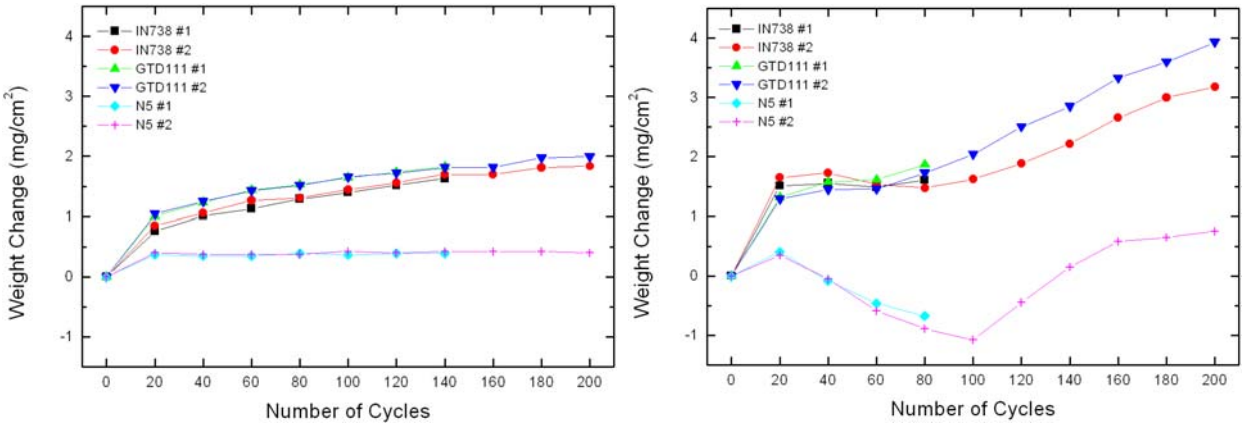

(a) With no deposit in wet air (b) With CaO deposits in wet air

Figure 4.22 Weight change measurements for the cyclic oxidation of René N5, GTD 111, and IN 738 at 950^{o}C in wet air (a) with no deposit and (b) with CaO deposits.

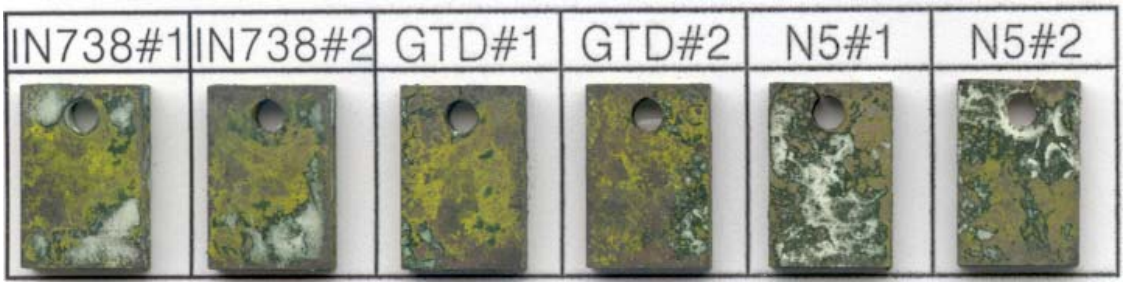

(a) Before cleaning

(b) After Cleaning

Figure 4.23 Surface photographs of the surfaces of coupon specimens after 80 hours exposure with CaO deposits at 950^{o}C in wet air (a) before and (b) after cleaning.

The surface photographs of specimens with CaO deposits after 80 hours of exposure at 950^{o}C in wet air are presented in Figure 4.23. The cleaned surfaces of the specimens show substantial attack. A comparison of micrographs showing cross-sections of René N5, GTD 111, and IN 738 after 80 hours in wet air with CaO deposits is presented in Figure 4.24. All three alloys show features indicating severe degradation. The René N5 specimen shows internal oxidation has occurred. The external scale is thin but it is apparent that much of the oxide has spalled. The internal oxide zone shows that the aluminum in this alloy is being oxidized

internally. The cross-section micrographs for GTD 111 and IN 738 are similar with some internal oxidation. The external scales are thick with features indicating that the chromium in IN 738 has been depleted to levels such that the chromium in this alloy is beginning to be oxidized internally.

The results obtained in the cyclic oxidation of the three alloys show some important features. When CaO deposits are not present, René N5 oxidizes significantly slower than GTD 111 and IN 738. This occurs because René N5 is an Al_2O_3-former whereas GTD 111 and IN 738 are Cr_2O_3-formers. When water vapor is present in the gas environment the oxidation is not much different than in dry air, but the internal oxidation appears to occur along alloy grain boundaries in the two polycrystalline alloys. CaO deposits in dry air cause all three alloys to exhibit more degradation but this attack is more severe on René N5 compared to GTD 111 and IN 738. The addition of water vapor to the gases causes the attack induced by CaO deposits to be more severe for all three alloys because there is more cracking and spalling of oxide in wet air. Again, the degradation of René N5 is more severe than that of GTD 111 and IN 738 in the presence of CaO deposits.

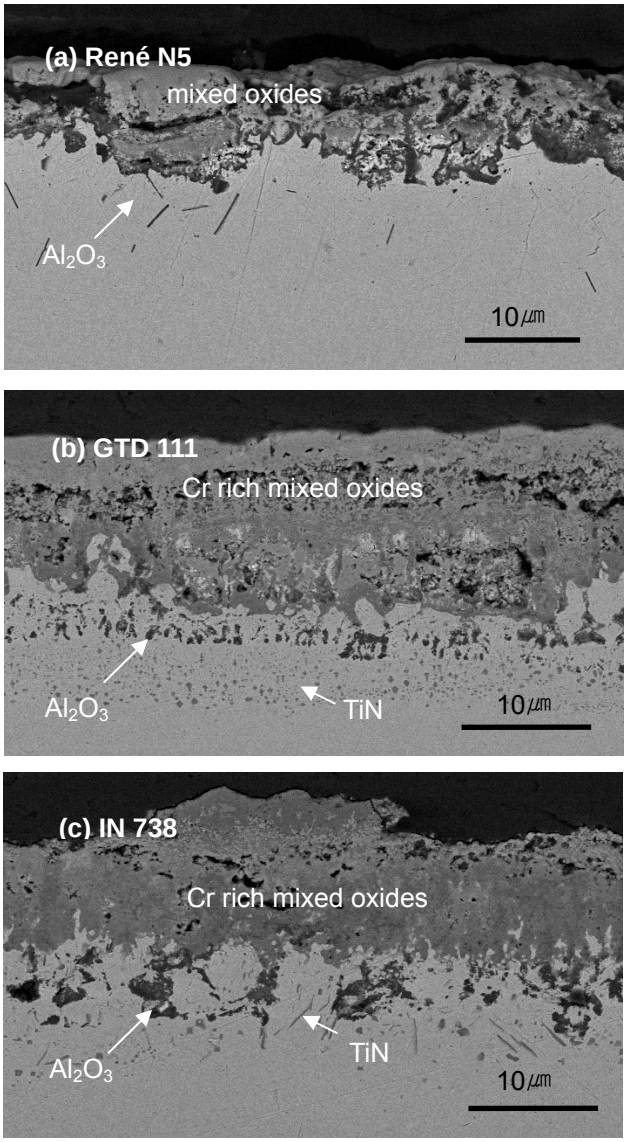

Figure 4.24 Micrographs showing cross-sections of (a) René N5, (b) GTD 111, and (c) IN 738 with CaO deposits at 950^{o}C in wet air after 80 hours exposure.

The degradation is more severe because Al_2O_3 formed on René N5 reacts with CaO to form Ca aluminates which are not considered as a protective layer. At the same time, aluminum is depleted in the underlying layer so that the concentration of Al is not sufficient to form an external Al_2O_3 scale. Therefore, Ni oxidizes rapidly to form NiO on top of the Ca aluminate layer. The NiO layer is thick because neither NiO nor Ca aluminates are a dense structure to make the diffusion of Ni^{+} and O^{2-} sluggish so that the oxygen partial pressure in this region is much higher than the dissociation pressure of NiO. As the Ni content beneath the Ca aluminates region is decreased due to the formation of an external NiO, a new internal Al_2O_3 can form again.

On the other hand, an external Cr_2O_3 layer on GTD 111 and IN 738 reacts with CaO to form Ca chromates ($CaCr_2O_4$). Since the thickness of the continuous Cr_2O_3 layer is large, some Cr_2O_3 still remains unreacted with CaO and provides partial protectiveness. However, cracks are created due to the formation of Ca chromates where the Ca-rich Cr_2O_3 layer becomes less protective. Therefore, the penetration of oxygen through the Cr- and Ca-rich mixed oxides region is easier than through a pure Cr_2O_3 layer resulting in thicker Cr-rich corrosion products. Also, the penetration depth of an internal Al_2O_3- and TiN- forming region is increased.

In Figures 4.25, schematic profiles of oxygen partial pressures are superposed on cross-section micrographs of exposed IN 748 specimens as a function of distance from the surface with and without CaO deposits. Note that the gradient of the oxygen partial pressure is steeper in the

specimen with no deposit. This means that the oxygen flux through the Ca chromate layer is larger than that through the chromia layer. It is known that both ionic diffusion and gas permeation contribute to the overall gas flux through the coating, with the relative contributions from each mechanism depending on factors such as the chemistry and structure of the media.[77-78] The contribution of oxygen permeation to the overall oxygen flux through the chromia layer is very small because of its dense structure. However, the contribution of the permeation becomes larger when Ca chromates form in the chromia layer. The formation of an interconnected network of phase boundaries attributes to a more permeable structure. Therefore, the thickness of the oxide layer becomes larger in the presence of CaO deposits.

On the other hand, the penetration depth of an internal oxide zone is associated with the dissociation pressures of Al_2O_3 and Cr_2O_3 at 950°C, which are designated as $P_{O_2}^{Al/Al_2O_3}$ and $P_{O_2}^{Cr/Cr_2O_3}$, respectively. The values of $P_{O_2}^{Al/Al_2O_3}$ and $P_{O_2}^{Cr/Cr_2O_3}$ can be calculated using the following thermodynamic reactions:

$2Al\ (s) + 3/2O_2\ (g) = Al_2O_3\ (s)$, $\Delta G^{o}_{950^{o}C} = -1287.0$ kJ/mol, $P_{O_2}^{Al/Al_2O_3} = 2.25 \times 10^{-37}$ atm

$2Cr\ (s) + 3/2O_2\ (g) = Cr_2O_3\ (s)$, $\Delta G^{o}_{950^{o}C} = -815.5$ kJ/mol, $P_{O_2}^{Cr/Cr_2O_3} = 6.01 \times 10^{-24}$ atm

In the region where the oxygen partial pressure is in the range between $P_{O_2}^{Cr/Cr_2O_3}$ and $P_{O_2}^{Al/Al_2O_3}$, Cr_2O_3 is no more stable and the only stable oxide in this region is Al_2O_3. Additionally, internal aluminum oxides mainly form along the grain boundaries because of the higher diffusion coefficient of oxygen along the grain boundary.

The mechanism by which CaO causes increased degradation of these alloys will be discussed in section 4.5. It has been found that CaO deposits react with Al_2O_3 and Cr_2O_3 scales to form calcium aluminates and calcium chromates, respectively. Pseudo-binary phase diagrams of CaO-$AlO_{1.5}$ and CaO-$CrO_{1.5}$ are shown in Figures 4.26 and 4.27, respectively. At 950^{o}C, these phases are solid. The phases that form on the surfaces of these alloys are less protective and more prone to spalling compared to the unreacted Al_2O_3 and Cr_2O_3 oxide scales. Consequently, the degradation is more severe.

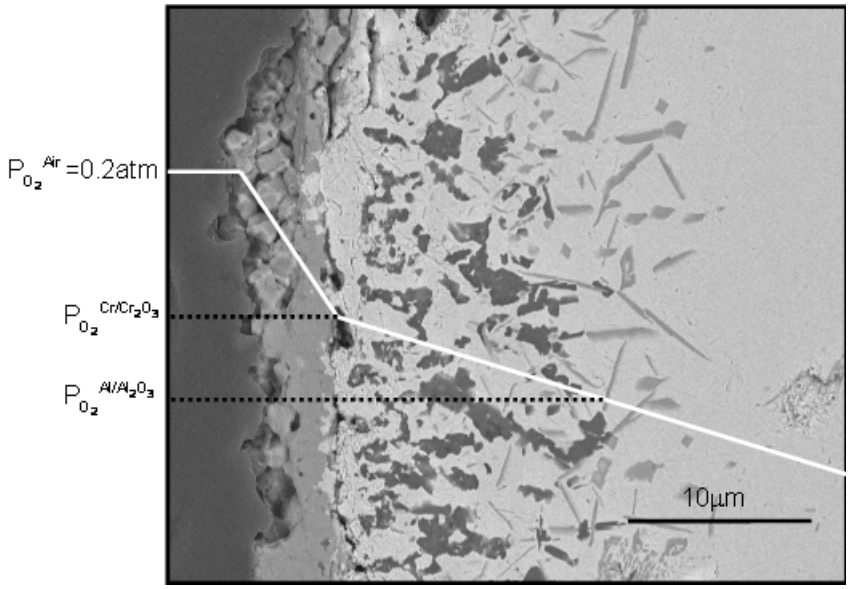

(a) IN 738 with no deposit cyclically exposed at 950°C in dry air for 140 hours.

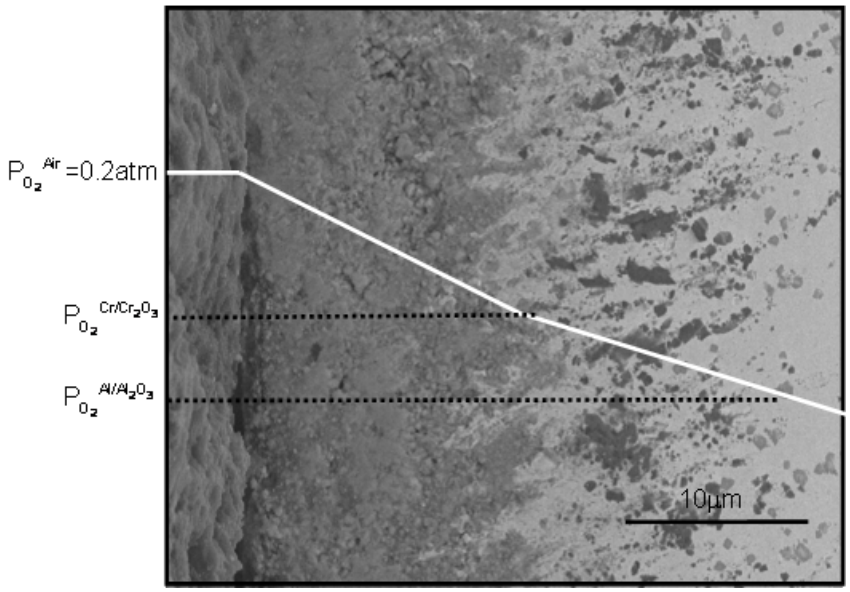

(b) IN 738 with CaO deposits cyclically exposed at 950°C in dry air for 80 hours.

Figure 4.25 Schematic profiles of the oxygen partial pressure as a function of distance from the surface of uncoated IN 738 specimens (a) with no deposit and (b) with CaO deposits. Note that oxygen partial pressure gradient is smaller in the specimen with CaO deposits than that with no deposit due to the presence of Ca chromates and transient oxides.

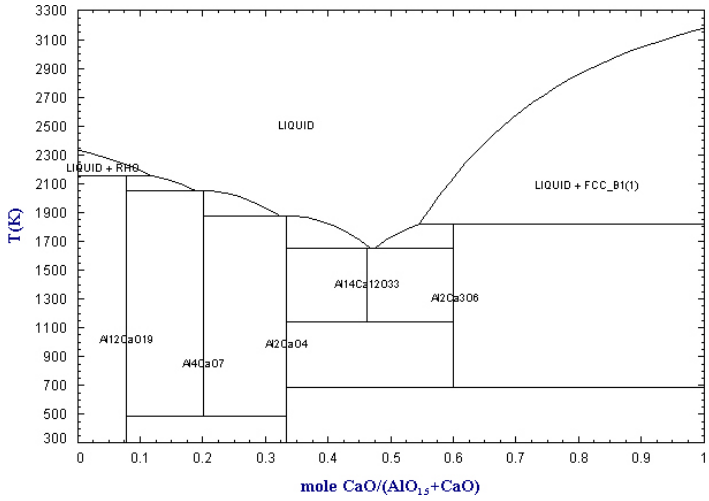

Figure 4.26 A pseudo-binary phase diagram of $CaO\text{-}AlO_{1.5}$. From FactSage thermochemical database system.

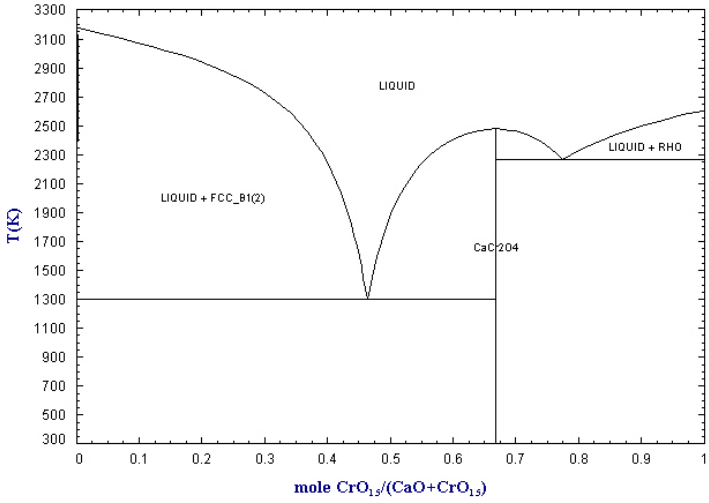

Figure 4.27 A pseudo-binary phase diagram of $CaO\text{-}CrO_{1.5}$. From FactSage thermochemical database system. Note that the only ternary compound is the $CaCr_2O_4$ at 950°C.

4.3.2 Comparison of Coated Alloys

Six different combinations of two coatings and three substrate alloys were investigated in these experiments. A list of coated specimens is as shown in Table 3-2. Coated alloys were cyclically exposed at 950^{o}C in dry and wet air with and without CaO deposits. Specimens with no deposit were exposed to compare the results with those with CaO deposited specimens. Results from these experiments are presented in the following subsections. In discussing the degradation of the coated alloys, weight change versus time measurements will be presented and discussed, and then metallographic examination of the exposed specimens will be considered.

4.3.2.1 Comparison of Weight Change versus Time Measurements for Coatings on Different Alloy Substrates - Weight change versus time measurements for the platinum aluminide coating on the three alloys substrates are presented in Figure 4.28 where the cyclic oxidation conditions are for (a) no deposit in dry, (b) no deposit in wet, (c) CaO deposits in dry, and (d) CaO deposits in wet air. The specimens with no deposit showed a small amount of continuous weight gain, whereas specimens with CaO deposits showed a small weight gain followed by a continuous weight loss. No significant influence of the alloy substrates on the platinum aluminide coating was evident for the time and temperature that were used. No significant effect of water vapor was evident on the degradation with or without deposits.

Weight change versus time measurements for the CoNiCrAlY coating on the three different alloy substrates are presented in Figure 4.29 where the cyclic oxidation conditions are the same as those described in Figure 4.28. The results obtained with the CoNiCrAlY, where the CaO deposits caused increased degradation, did not indicate a significant effect of water vapor nor did the alloy substrates affect the coating degradation.

However, upon comparing the magnitude of the weight losses for the platinum aluminide and CoNiCrAlY coatings with CaO deposits, while there is some variability in the weight changes, it can be seen that the platinum aluminide coating exhibits smaller weight changes than the CoNiCrAlY coating but none of these systems show indications of excessive degradation both in dry and wet air.

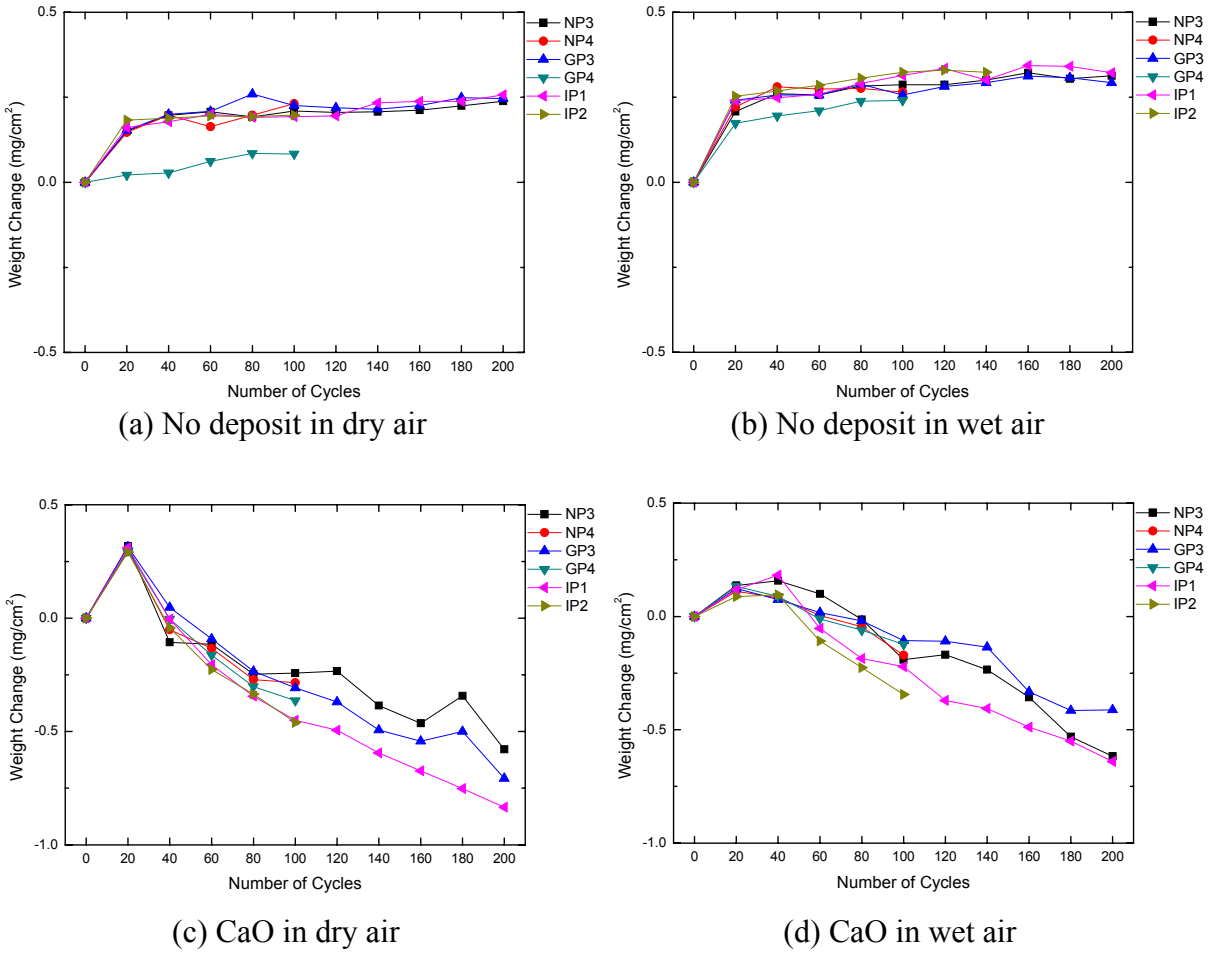

(a) No deposit in dry air

(b) No deposit in wet air

(c) CaO in dry air

(d) CaO in wet air

Figure 4.28 Weight change versus time measurements of platinum aluminide coatings on René N5 (NP), GTD 111 (GP), and IN 738 (IP) exposed at 950°C with and without CaO deposits in dry and wet air.

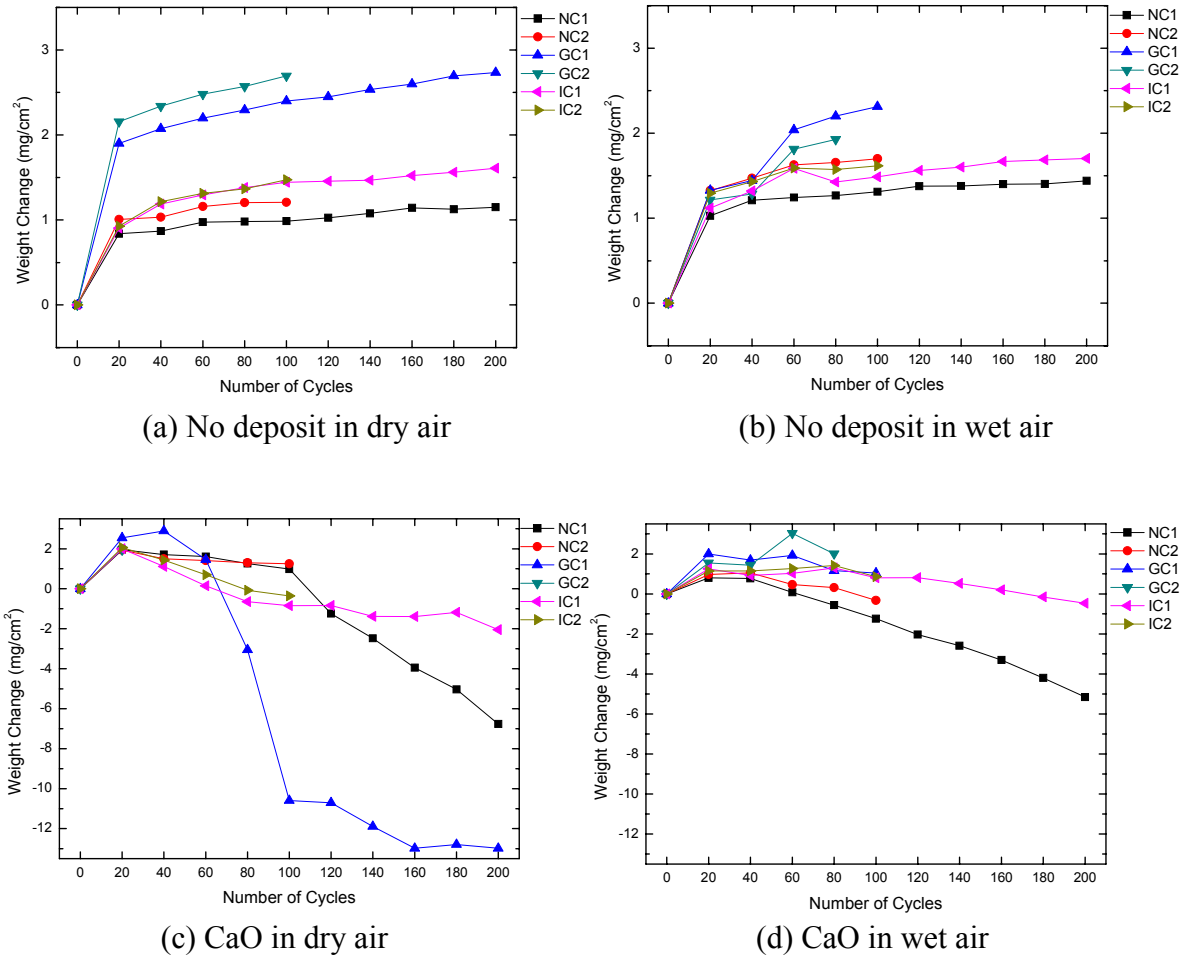

Figure 4.29. Weight change versus time measurements of CoNiCrAlY coatings on René N5 (NC), GTD 111 (GC), and IN 738 (IC) with and without CaO deposits exposed at 950°C in dry and wet air. Note that scales are different between plots of specimens with and without CaO deposits.

4.3.2.2 Comparison of the Microstructures of the Exposed Coatings on Different Alloy Substrates - In Figure 4.30 through 4.33, cross-section micrographs of the coatings exposed 100 hours at 950^{o}C are presented for no deposit in dry, Figure 4.30, no deposit in wet, Figure 4.31, CaO deposits in dry, Figure 4.32, and CaO deposits in wet air, Figure 4.33. The platinum aluminide coatings with no deposit in dry air, Figures 4.30 (a), (b) and (c), had undergone very little attack. External alumina scales developed on these coatings and no effect of the alloy substrates was apparent. In the case of the CoNiCrAlY coating, Figures 4.30 (d), (e) and (f), oxides other than alumina (e.g. Cr_2O_3, $NiAl_2O_4$, etc.) were evident, but the amount of degradation was not large. The presence of water vapor in the air did not significantly affect the oxidation of these coatings, Figure 4.31. Alumina scales were still evident on the platinum aluminide coatings, Figures 4.31 (a), (b) and (c), whereas chromia and spinels were detected in addition to alumina on the CoNiCrAlY coating, Figures 4.31 (d), (e) and (f). It has been found that water vapor usually affects the oxidation of alloys that are marginal alumina-formers and the current results are consistent with this observation.

The presence of CaO deposits causes substantial degradation of all three of the coatings both in dry and wet air, Figure 4.32 and 4.33, respectively. The attack is often localized as is evident in Figures 4.32 (a), (b), (c) and (d). This localized attack may occur in that the

application of the CaO deposits was not always uniform. The presence of water vapor did not cause the attack induced by the CaO deposits to be substantially more severe, Figure 4.33. However, the attack caused by the CaO was substantial in both dry and wet air, and it was difficult to determine if wet conditions caused the attack induced by CaO deposits to be more severe. The features of the attack induced by CaO deposits were similar in both dry and wet air. The metallographic results presented in Figures 4.32 and 4.33 reflect the fact that the weight losses for the platinum aluminide coating were an order of magnitude less than those for the CoNiCrAlY coating. This indicates that the degradation processes are similar for both coatings but occur at lower rates for the platinum aluminide coating.

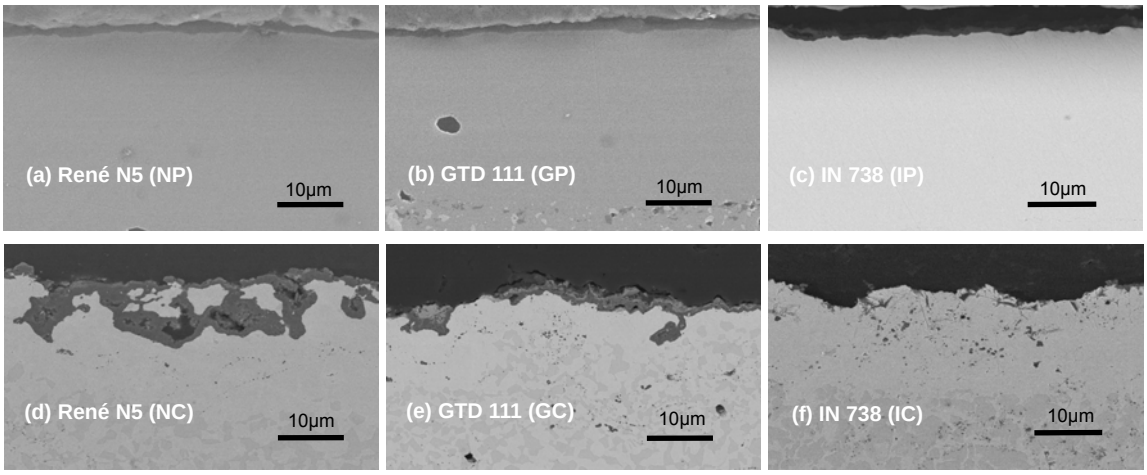

Figure 4.30 Cross-section micrographs of coated specimens with no deposit exposed at 950^{o}C in dry air after 100 hours.

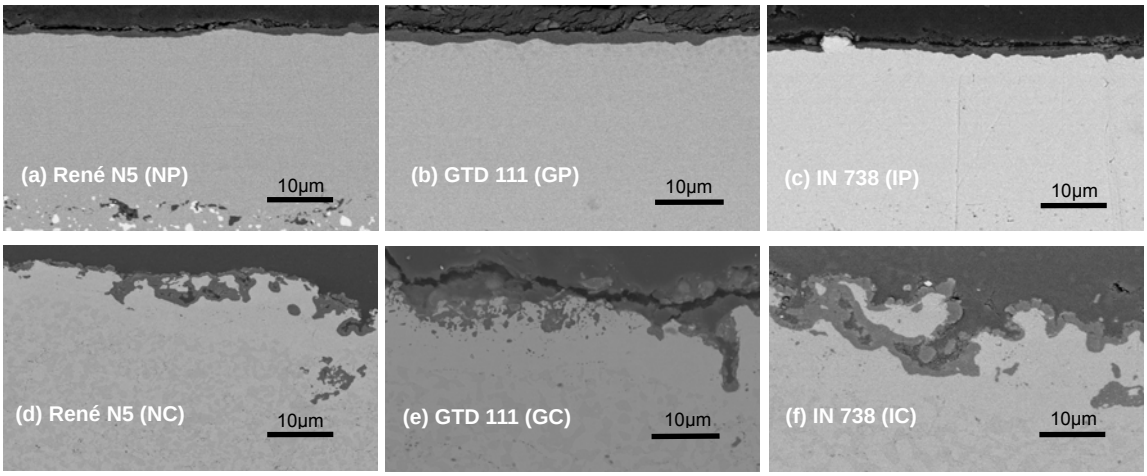

Figure 4.31 Cross-section micrographs of coated specimens with no deposit exposed at 950^{o}C in wet air after 100 hours.

The mechanism by which the CaO causes the coatings to degrade appears to be reaction with the oxide scales that normally are developed on these coatings, namely, alumina with some Cr_2O_3 and $NiAl_2O_4$ spinel in the case of the CoNiCrAlY coatings. The products that form, in particular, Ca aluminates and Ca chromates, are prone to spall under the influence of stresses induced by thermal cycling. It appears that the CoNiCrAlY coating is degraded more than the platinum aluminide coating. The section 4.5 describes the results of experiments intended to provide further understanding of the interactions between CaO and oxide scales.

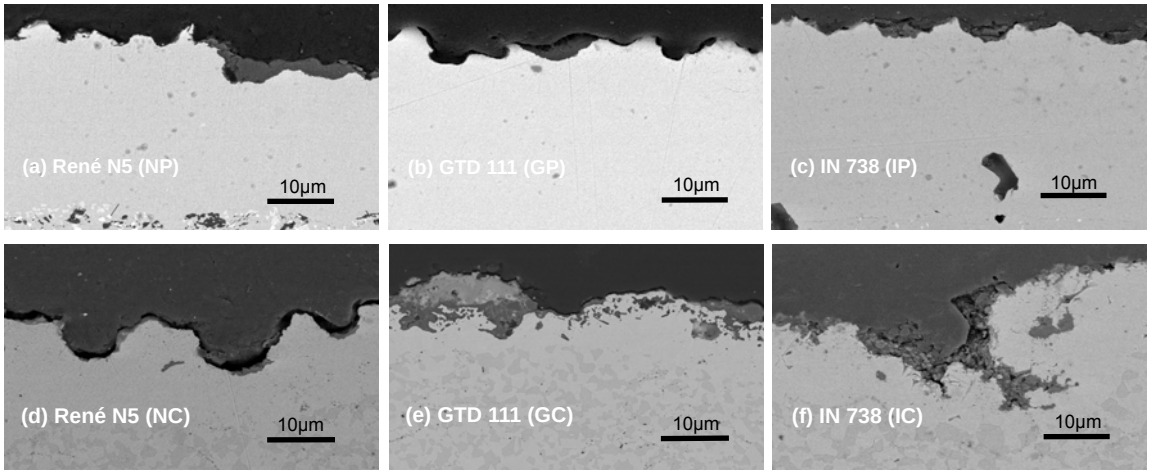

Figure 4.32 Cross-section micrographs of coated specimens with CaO deposits exposed at 950^{o}C in dry air after 100 hours.

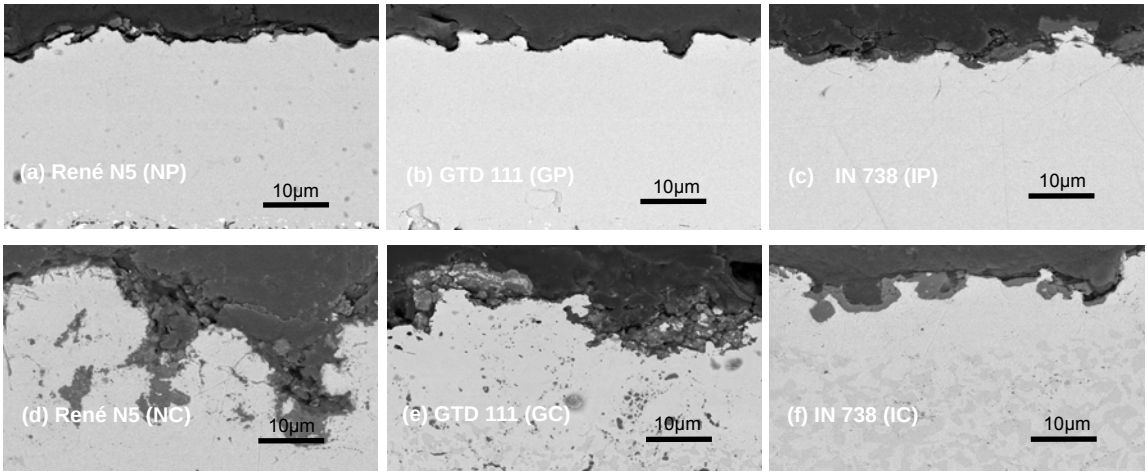

Figure 4.33 Cross-section micrographs of coated specimens with CaO deposits exposed at 950^{o}C in wet air after 100 hours.

4.4 EFFECTS OF CaO DEPOSITS ON THREMAL BARRIER COATINGS

Air Plasma Sprayed (APS) Thermal Barrier Coating (TBC) specimens have been isothermally exposed at 950^{o}C to CaO deposits in dry air. The TBC system investigated consisted of René N5 substrates, a NiCoCrAlY bond coat and an APS yttria-stablized zirconia (YSZ, ZrO_2-$7Y_2O_3$) topcoat. Figure 4.34 shows TBC-coated disks in the as-received condition and after exposures for 100 and 200 hours with and without CaO deposits. The as-received TBC is gray in color. This is believed to be the result of slight reduction of the YSZ occurring in the plasma. When the TBC is exposed in air it quickly develops a white color. The specimens exposed with CaO deposits are slightly discolored suggesting that there is some interaction between the YSZ and CaO.

Figures 4.35 and 4.36 show higher magnification micrographs of the TBC surface in the as-received state and after air exposures. There is some indication of sintering as the width of cracks intersecting the surface decrease with exposure at 950^{o}C even though the sintering is not significant due to the low exposure temperature. Figure 4.37 shows cross-sections of the TBC in the as-received condition and after 200 hours exposure at 950^{o}C with no deposit. Some of the vertical cracks appear to have sintered along part of their length in the exposed TBC.

Figure 4.34 Surfaces of APS TBCs in the as-received condition and after 100 and 200 hours exposure with and without CaO deposits. The diameter of each coupon specimen is 2.54 cm.

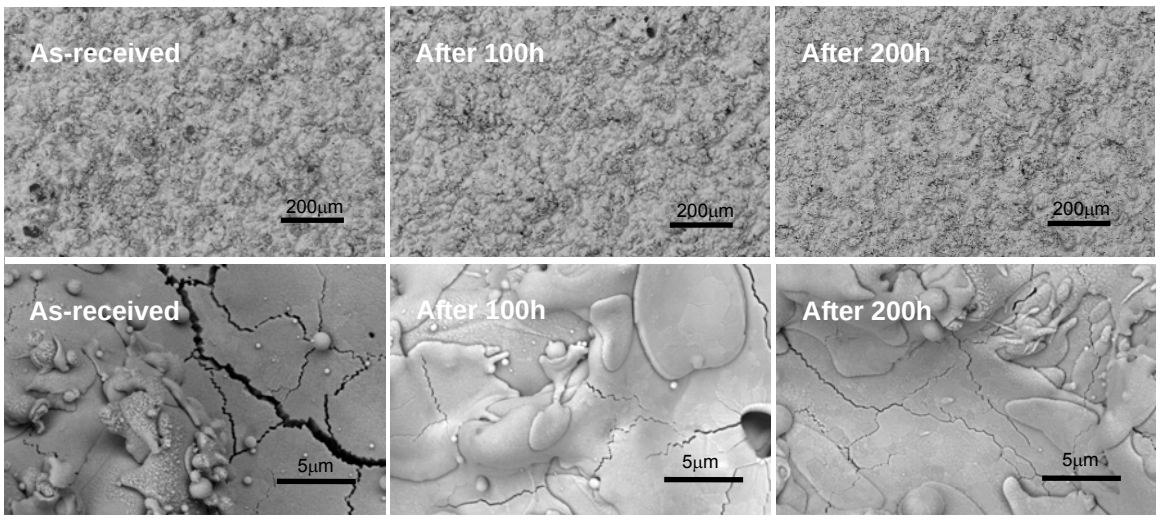

Figure 4.35 Higher magnification (100x for upper three and 5000x for lower three micrographs) micrographs of the surfaces of APS TBCs in the as-received condition and after 100 and 200 hours exposure at 950˚C with no deposit.

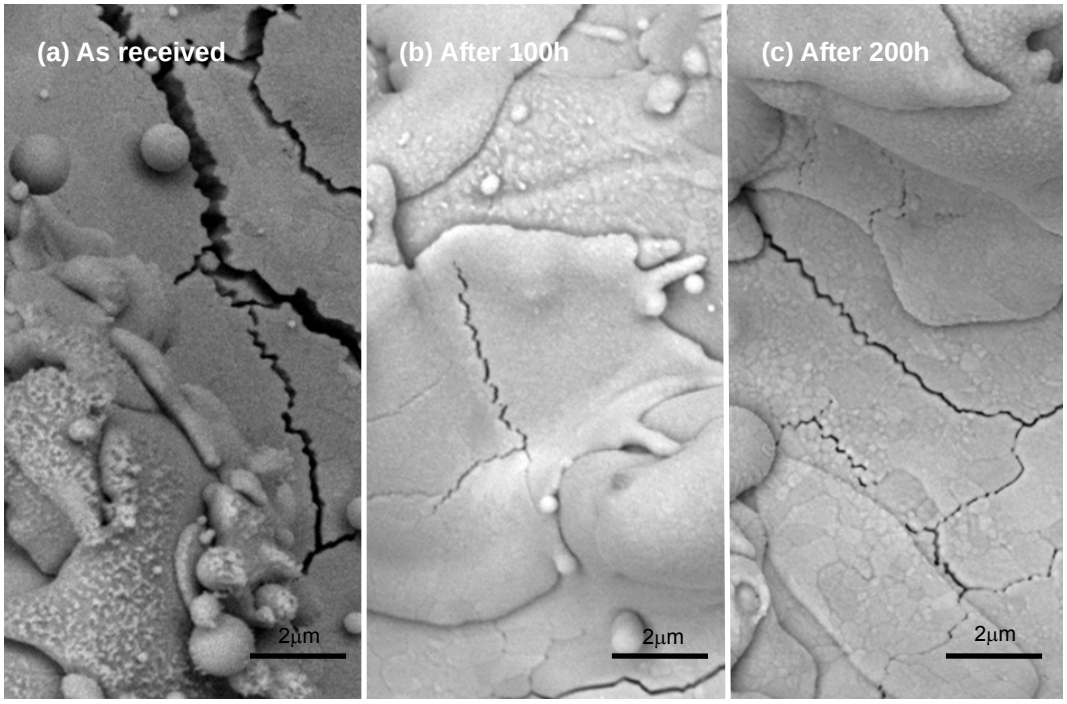

Figure 4.36. Higher magnification micrographs of the surfaces of APS TBCs in the as-received condition and after 100 and 200 hours exposure at 950°C with no deposits.

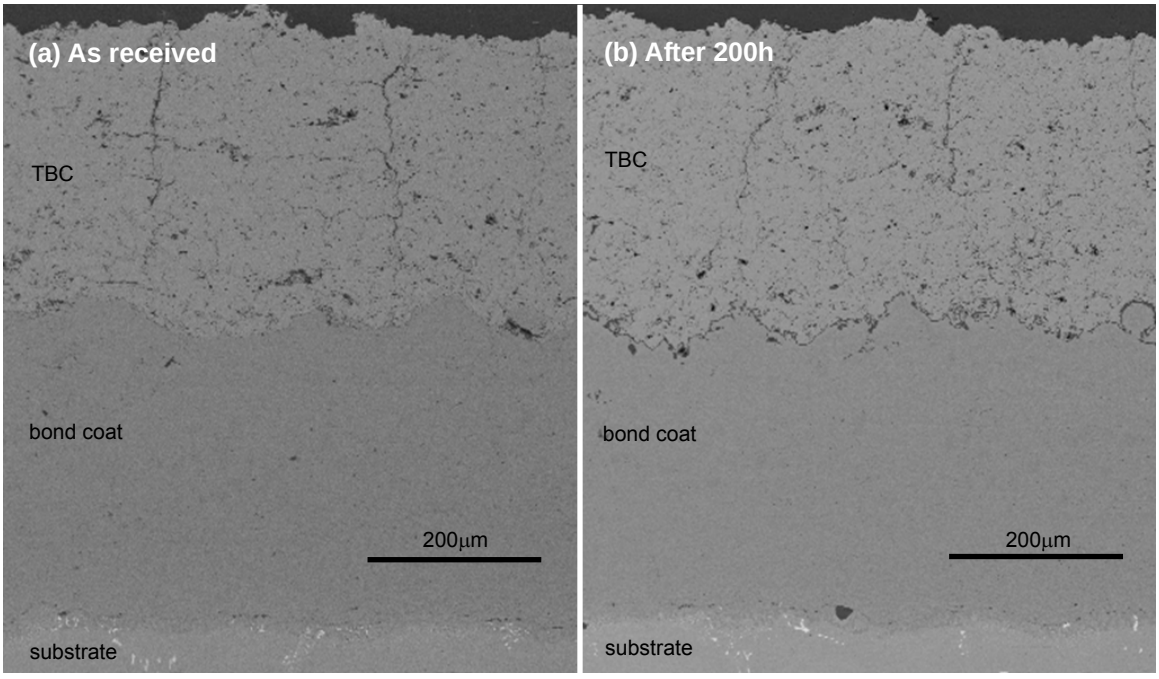

Figure 4.37 Cross-section micrographs of APS TBCs in the as-received condition and after 200 hours exposure at 950°C with no deposit.

Figure 4.38 shows cross-sections of the TBC after 200 hours exposure at 950°C with and without CaO deposits. There is very little difference between the two microstructures except that the TGO is more clearly visible for the specimen exposed with CaO. Figures 4.39 and 4.40 present TBCs in the as-received condition and after 200 hours exposure at 950°C with CaO deposits. The exposed specimen shows material remaining on the surface which contains both Ca and Zr and may be a Ca zirconate ($CaZrO_3$).

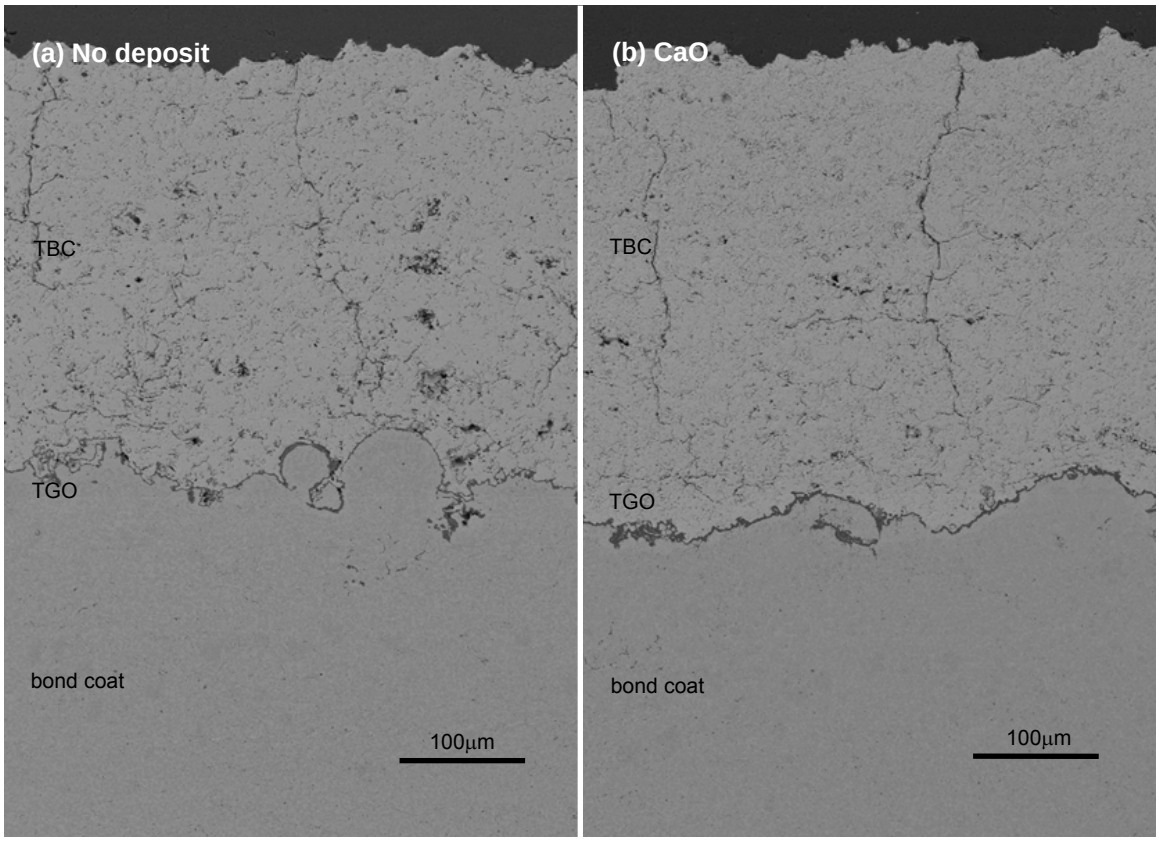

Figure 4.38 Cross-section micrographs of APS TBCs after 200 hours exposure at 950°C with and without CaO deposits.

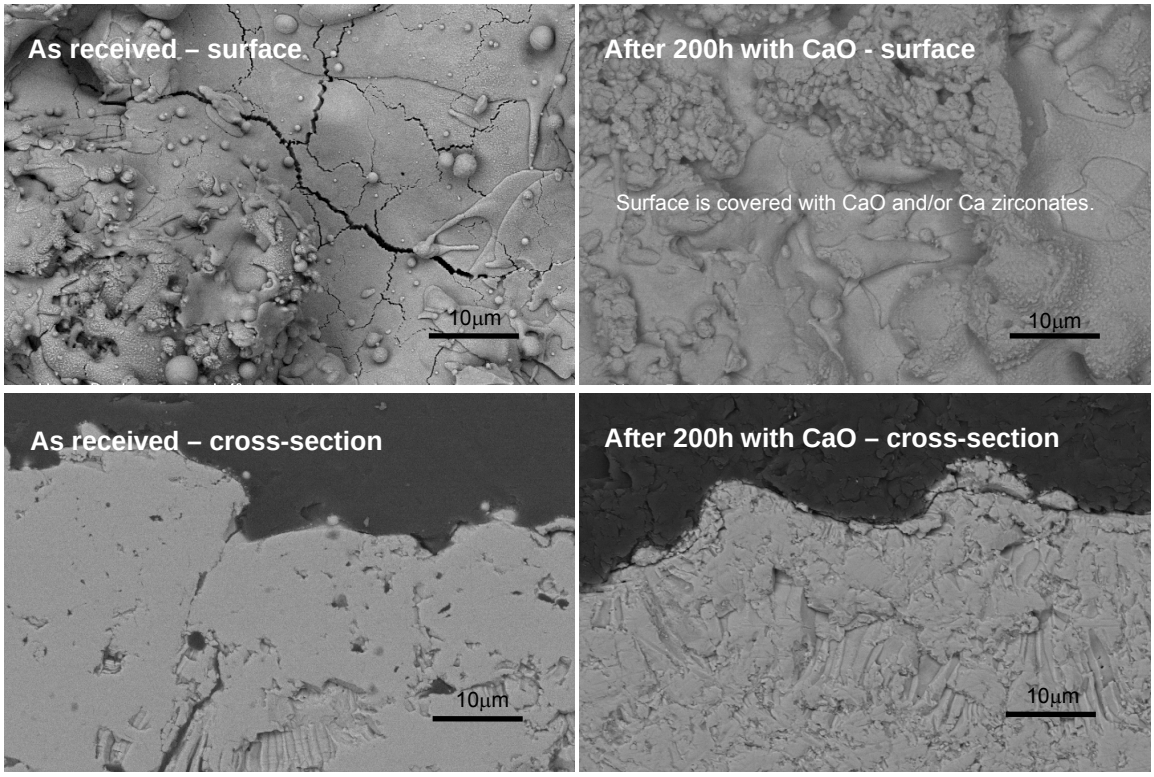

Figure 4.39 Surfaces and cross-sections of APS TBCs in the as-received condition and after 200 hours exposure at 950°C with CaO deposits.

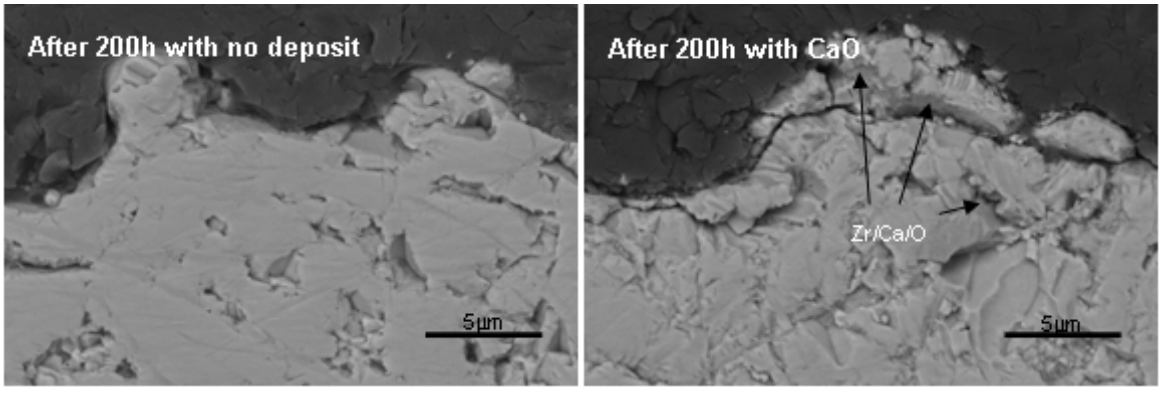

Figure 4.40 Higher magnification cross-section micrographs of APS TBCs after 200 hours exposure at 950°C with and without CaO deposits.

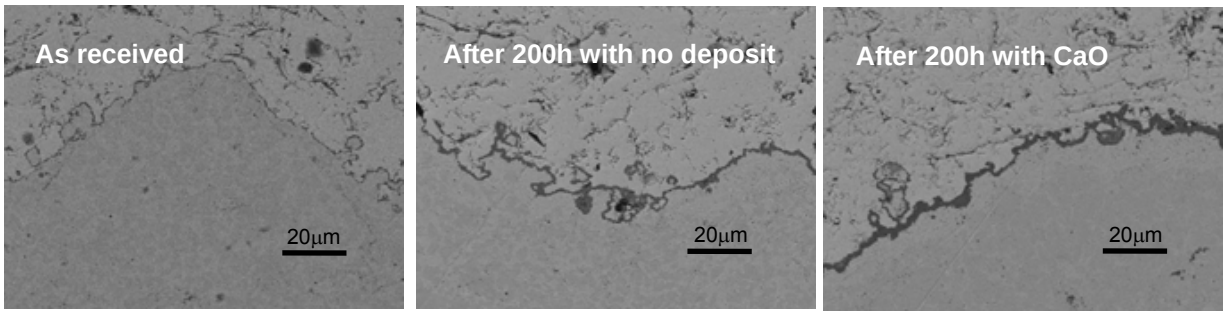

Figure 4.41 Cross-sections of APS TBCs in the as-received condition and after 200 hours exposure at 950°C with and without CaO deposits showing the TGO thickness.

Figure 4.41 compares the interface between the YSZ and NiCoCrAlY bond coat for the as-received TBC, and the specimens exposed for 200 hours with and without the CaO deposits. There is no TGO apparent in the as-received specimen. A TGO has grown on the bond coat of the exposed specimens and it appears that the TGO is thicker on the specimen exposed with CaO. The reason for the thicker TGO growth in the presence of CaO is not clear since several authors in the literature simply state that the top coat is transparent to oxygen due to the porous and microcracked structure of plasma sprayed coatings.[79-80] However, some studies suggested that the presence of the top coat reduces oxide growth rates by a small amount offering some resistance to oxygen penetration, although this is not a strong effect.[81-82] Figure 4.42 shows the effect of coating thickness on the permeability of ZrO_2-4.9 mol% Y_2O_3 plasma sprayed coatings.[83] It is suggested that there is an optimum coating thickness, below which measured permeability values are higher (see the curve for a 120 μm thick coating). If the coating thickness

is larger than the optimum coating thickness, the permeability does not change with respect to the coating thickness. This suggests that the network of interconnected pore space is thickness dependent, up to a limiting thickness. Based on these speculations, it is believed that Ca zirconates that form along the vertical cracks in the TBC, open paths of oxygen delivery to the TGO/TBC interface and the oxygen penetration to the TGO is increased to form thicker TGO layers by reducing the effective thickness of the top coat.

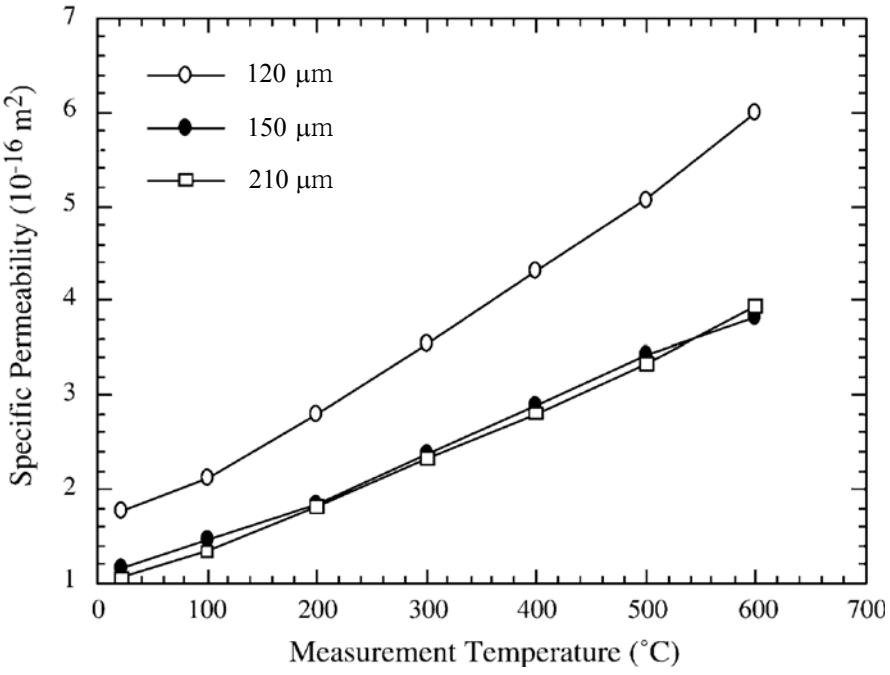

Figure 4.42 Effect of coating thickness on the measured specific permeability of ZrO_2-4.9 mol% Y_2O_3 plasma sprayed coatings, measured with O_2.

Figure 4.43 compares cross-sections of TBCs exposed for 200 hours at 950°C with a CaO deposit and embedded in CaO powder. The microstructures are similar but the external layer of a Ca-Zr oxide ($CaZrO_3$) is thicker for the specimen embedded in CaO powder. Figure 4.44 presents a cross-section of a TBC exposed for 200 hours at 950°C with a sprayed CaO deposit along with elemental maps of the same region. The figure indicates a Ca-Zr oxide at the surface but there is also Ca distributed along a vertical crack running through the TBC. It is not clear if this Ca is the result of CaO-containing liquid penetrating the crack during spraying or if the Ca has migrated during the exposure at 950°C. Figure 4.45 shows a corresponding cross-section and elemental maps for a TBC exposed for 100 hours at 950°C while embedded in CaO powder. The Ca-Zr oxide at the surface is clearly indicated but the penetration of Ca into the coating is less apparent. The phase present in the surface layer has not been identified. The phase diagram for the CaO-ZrO_2 system, Figure 4.46, indicates a ternary oxide, $CaZrO_3$ which is the only thermodynamically stable ternary oxide, could form when ZrO_2 and CaO are placed in contact at 950°C.

It is clear that there is significant reactivity between the YSZ and the CaO deposits. This reactivity is likely to be detrimental to TBC durability but the current experiments were not long enough to verify this.

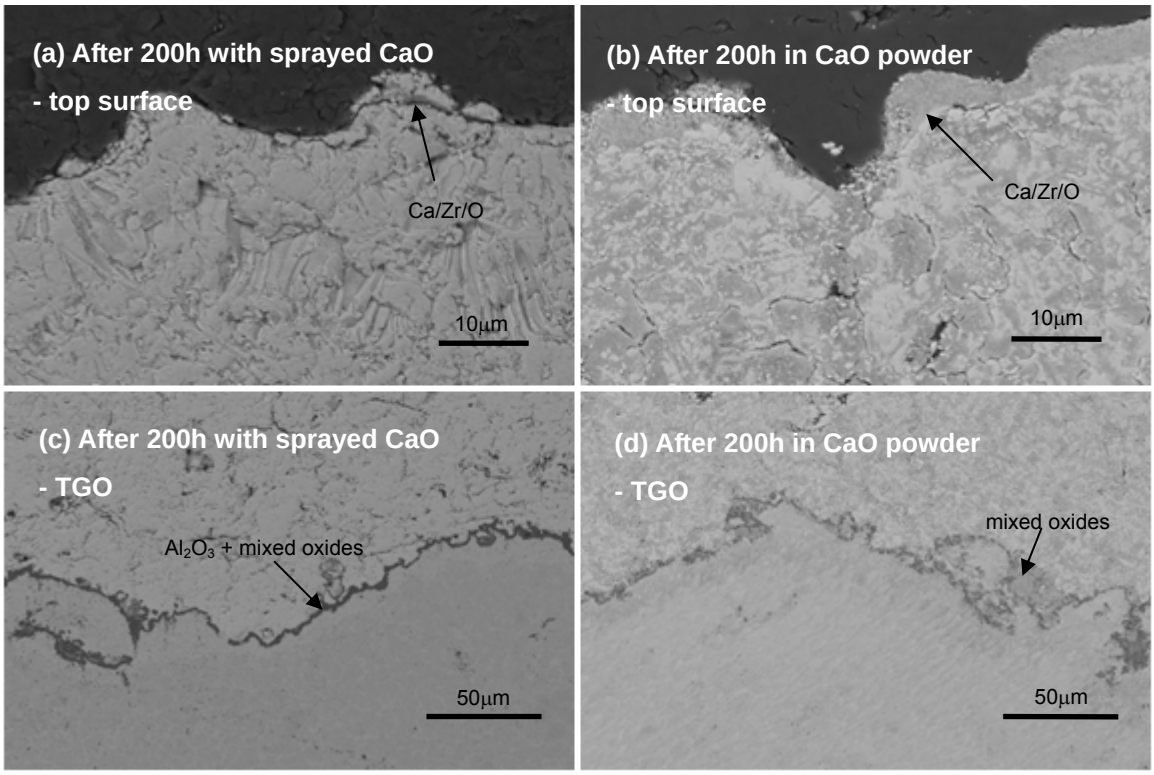

Figure 4.43 Cross-section micrographs comparing the microstructures of APS TBCs exposed at 950^{o}C with CaO deposits and embedded in CaO powder.

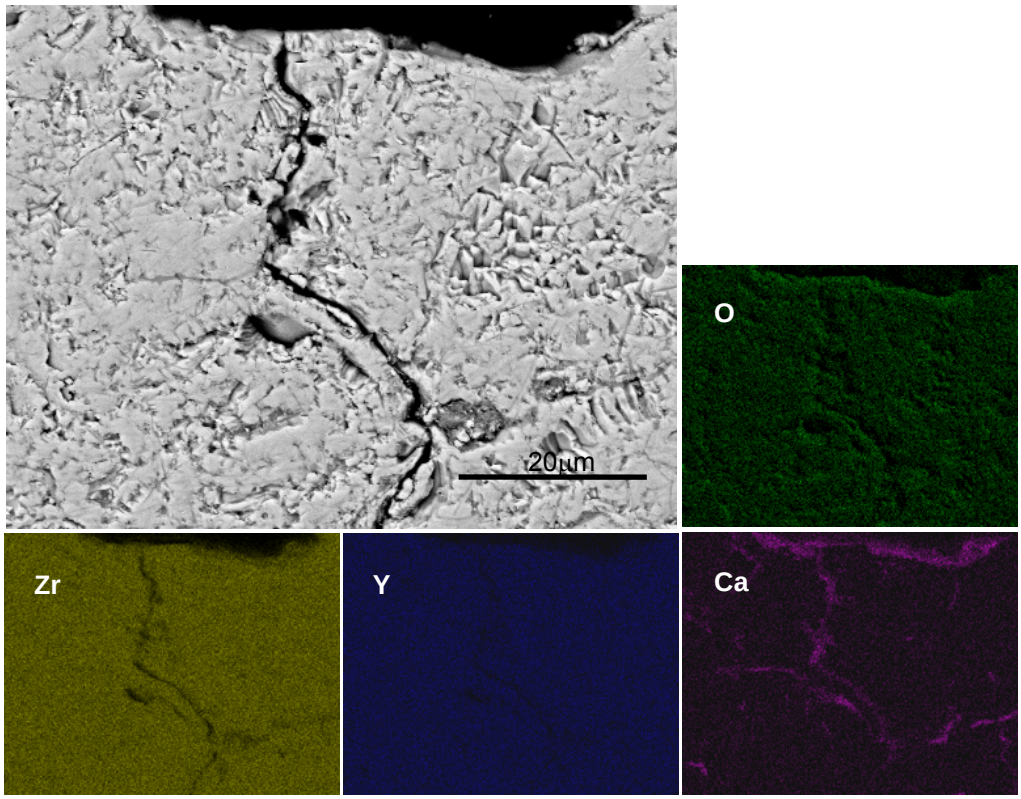

Figure 4.44 Cross-section micrograph and elemental maps for an APS TBC exposed for 200 hours at 950°C with CaO deposits.

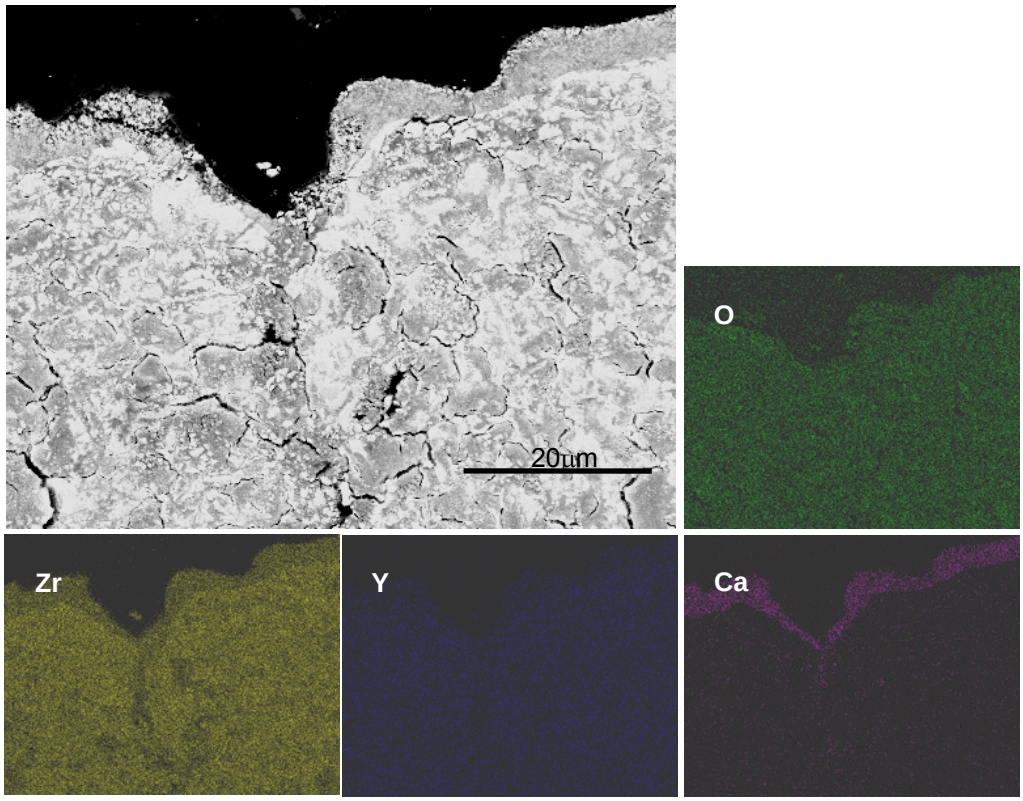

Figure 4.45 Cross-section micrograph and elemental maps for an APS TBC exposed for 100 hours at 950^{o}C embedded in CaO powder.

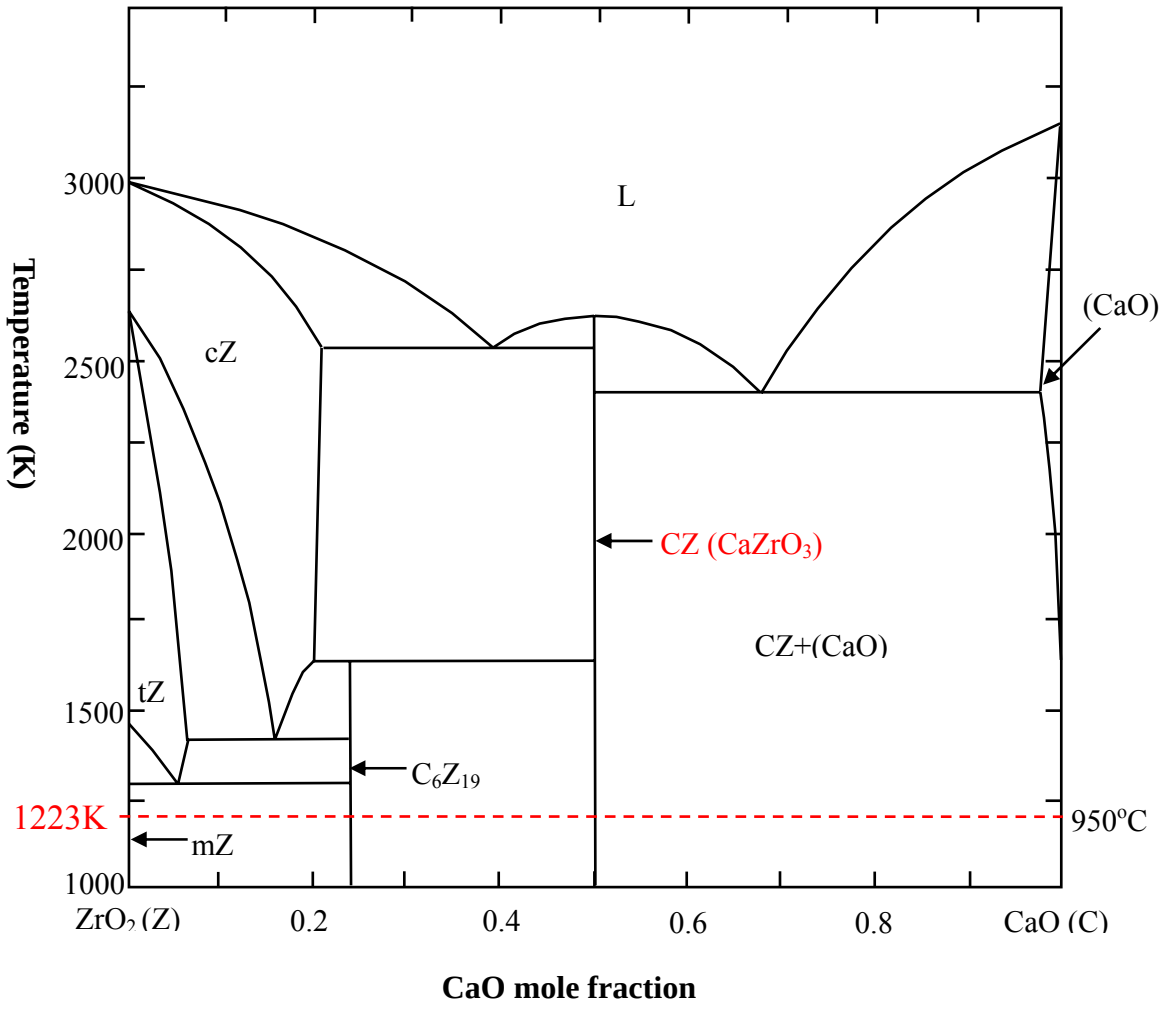

Figure 4.46 A pseudo-binary phase diagram for the CaO-ZrO_2 system. Note that cZ, tZ, mZ, and (CaO) in the diagram represent cubic, tetragonal, monoclinic ZrO_2, and solid solution CaO, respectively.

4.5 INTERACTIONS BETWEEN CaO AND OXIDE SCALES

Several experiments were conducted to investigate the interactions between bulk alumina and CaO. Specimens of polycrystalline alumina were exposed at 950^{o}C while embedded in CaO powder, Figure 4.47. The polycrystalline alumina had apparently been hot pressed in graphite dies as it had carbon on the edges of the coupons. This was removed by heating in air at 1100^{o}C for 60 hours before starting the experiments with CaO powder. Figure 4.48 shows surface photographs of the coupons before and after the 60 hour pretreatment. After 60 hours, the surface became brighter due to the removal of graphite by oxidation of carbon from the alumina specimen during pretreatment.

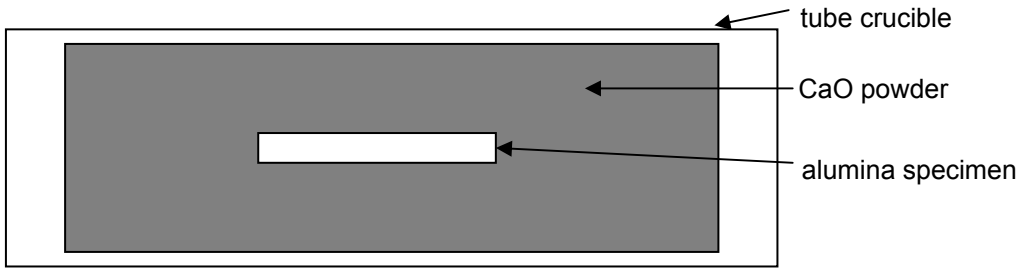

Figure 4.47 A schematic diagram of a crucible for exposing alumina coupons in CaO powder.

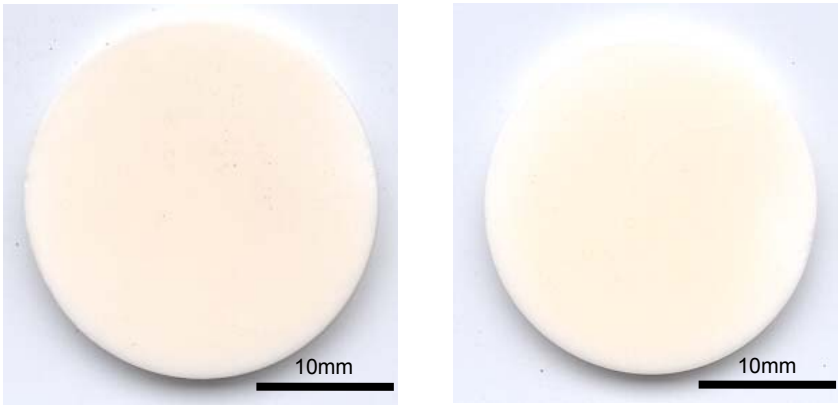

(a) As-received (b) After 60h pretreatment

Figure 4.48 Macroscopic photographs of polycrystalline alumina (Lucalox) (a) before and (b) after 60 hour pretreatment at 1100^{o}C

Figure 4.49 shows the surface micrographs of the polycrystalline alumina specimens before and after a 60 cycle exposure with CaO deposits. EDS indicated some Ca on the surface of the exposed specimen but the X-rays from the underlying material made it difficult to determine if this was a Ca-Al mixed oxide or simply CaO that had remained adherent.

As shown in Figure 4.26, a pseudo-binary phase diagram for the CaO-$AlO_{1.5}$ system indicates that CaO and Al_2O_3 should react to form a series of ternary Ca-Al oxides as listed in Table 4.2. Among the Ca-Al-O ternary compounds, only $CaAl_4O_7$ (CA_2) and $CaAl_{12}O_{19}$ (CA_6) are thermodynamically stable and the rest are metastable or intermediary stable phases under extra dry air environments.[84-92] Figure 4.50 shows XRD results from an experiment in which

CaO was heated in contact with a polycrystalline alumina crucible. Only $CaAl_4O_7$ could be identified from the XRD spectra. Nevertheless, this indicates there is some reactivity between CaO and alumina.

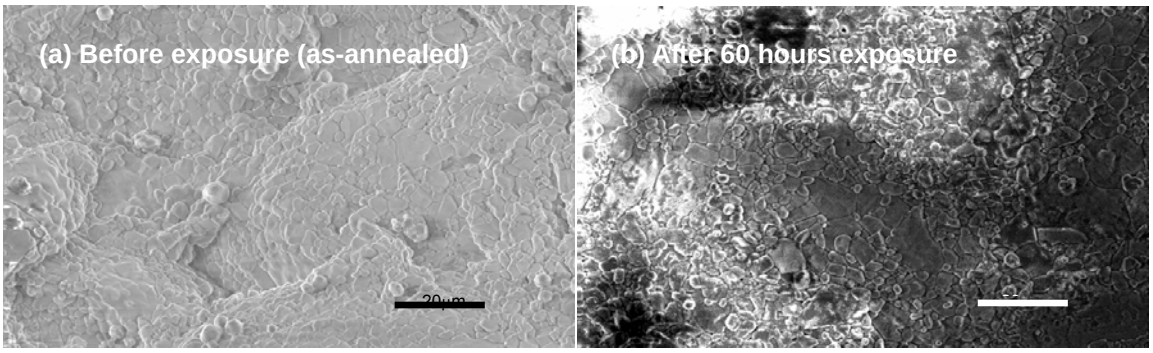

Figure 4.49 Surfaces of polycrystalline alumina specimens (a) before and (b) after 60 hours exposure in CaO at 950°C.

Table 4.2 Ternary compounds in the CaO-Al_2O_3 pseudo-binary phase diagram, Figure 4.26, at 950°C. C=CaO and A=Al_2O_3 in abbreviated formula.

Abbreviated Formula	Molecular Formula	Stability at 950°C
C	CaO	Stable
C_3A	$Ca_3Al_2O_6$	Intermediary stable[86-87]
$C_{12}A_7$ (=C_5A_3[84, 89-90])	$Ca_{12}Al_{14}O_{33}$	unstable in dry air[84-85]
CA	$CaAl_2O_4$	Intermediary stable[86-87]
C_3A_5 (=CA_2[91])	$Ca_3Al_{10}O_{18}$	Intermediary stable[86-87]
CA_2	$CaAl_4O_7$	Stable
CA_3	$CaAl_6O_{10}$	Intermediary stable[88]
CA_6	$CaAl_{12}O_{19}$	Stable (refractory[92])
A	Al_2O_3	Stable

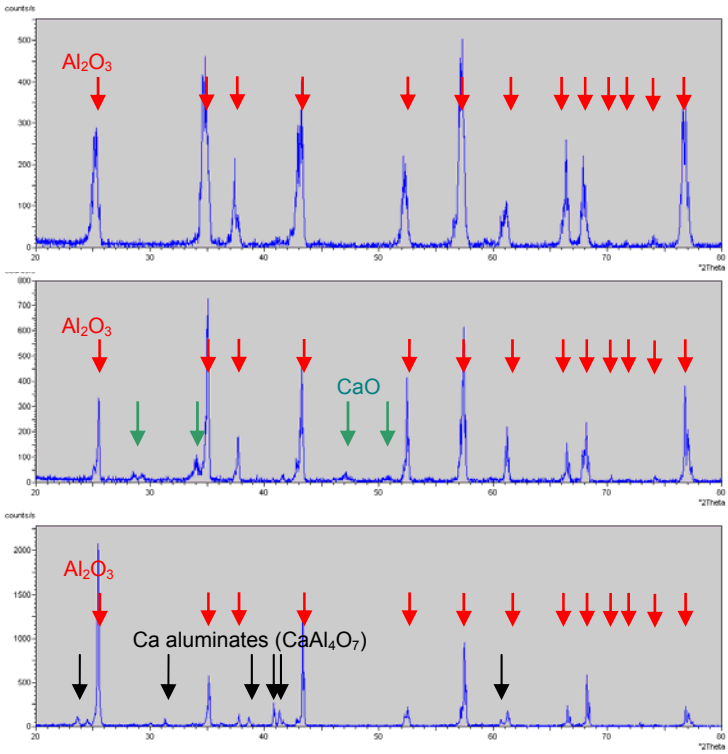

(a) Bare alumina

(b) Alumina deposited with CaO before exposure. Al_2O_3 and CaO were detected.

(c) Alumina deposited with CaO after exposure followed by ultrasonic cleaning.
- Remaining CaO was cleaned.
- Ca aluminates were formed.

Figure 4.50 XRD scans for exposure of polycrystalline alumina specimens with CaO deposits for 40 hours at 950°C. Note that the bottom scan indicates the presence of $CaAl_4O_7$.

Figure 4.51 shows an example to show that cracks are initiated and propagating along the phase boundaries between Ca aluminates and the recovered Al_2O_3 or underlying layers due to the difference in their thermal expansion coefficients. The specimen, IN 738 coated with Pt aluminide (IP), underwent cyclic exposure at 950°C for 100 cycles in dry air. Red lines are tracing crack paths in the figure.

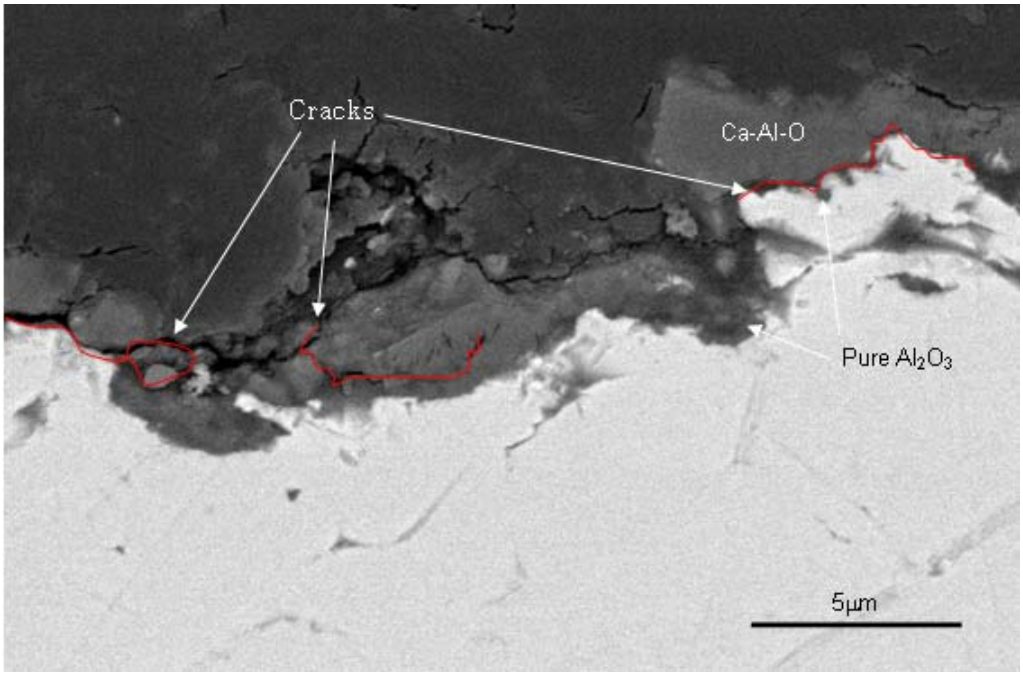

Figure 4.51 A cross-section micrograph of IN 738 coated with platinum aluminide (IP) exposed at 950°C in dry air for 100 hours showing cracks along the phase boundaries.

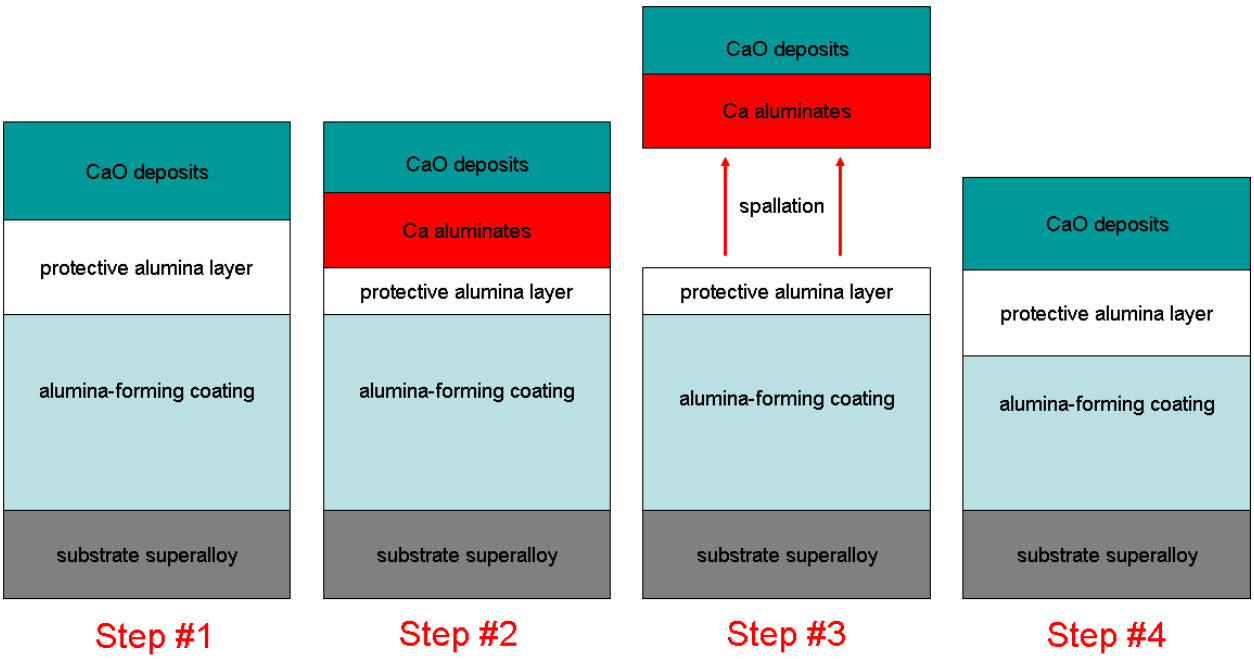

Figure 4.52 A schematic diagram showing the proposed effect of CaO on a growing alumina scale.

Based on these speculations, it is proposed that a major effect of the CaO in damaging a growing alumina scale is that depicted in the schematic diagram of Figure 4.52. The degradation mechanism can be described as follows:

Step #1: CaO deposits are accumulated on the Al_2O_3 protective layer (TGO).

Step #2: CaO reacts with a normally protective Al_2O_3 layer to form Ca aluminates which are not protective against oxidation of underlying layers.

Step #3: Cracks are initiated and propagate along the interface between Ca aluminates and protective alumina layer. They cause spallation of the Ca aluminate layer.

Step #4: An Al_2O_3 protective layer is recovered when the alumina layer is exposed to high oxygen partial pressure environment after the spallation. At the same time, CaO is continuously deposited on the Al_2O_3 layer. This repeats Step #1 - #4 until the coating material is completely used up.

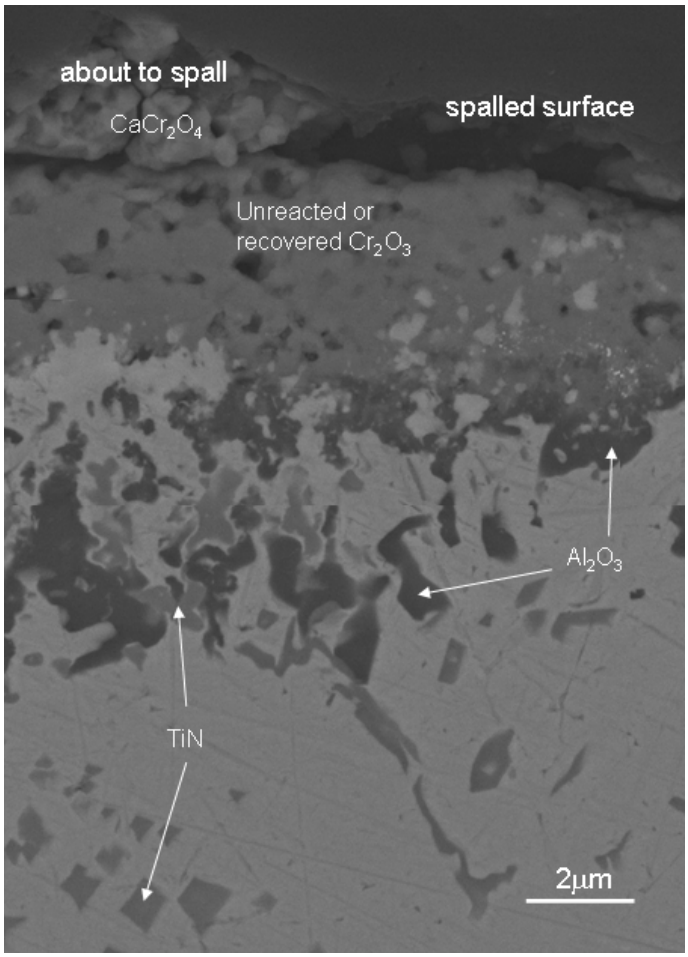

Figure 4.53. A cross-section micrograph showing cracks between $CaCr_2O_4$ and Cr_2O_3 on uncoated GTD 111 (G0) deposited with CaO.

In the case of Cr_2O_3-forming alloys or coatings, Cr_2O_3 reacts with CaO to form $CaCr_2O_4$, which is the only ternary phase in the phase diagram as shown in Figure 4.27. The degradation mechanism of Cr_2O_3-formers is similar to that of Al_2O_3-forming alloys or coatings, i.e., since the Ca chromate is not a protective species, due to the difference in thermal expansion coefficient from those of adjacent oxides and higher strain energy derived from the thicker oxide formation, it is prone to spall. An example of cracks initiated via the formation of Ca chromates is shown in Figure 4.53. It shows spalled surface and cracks along the boundaries between an unreacted Cr_2O_3 layer and Ca chromates, which are about to spall.

Figure 4.54 shows a cross-section micrograph of APS NiCrAlY coated Rene′ N5 (NN) specimen after 100 hour exposure at 950^{o}C in dry air. Cracks along phase boundaries are evident. If both Ca aluminates and Ca chromates are formed as reaction products as in the case of MCrAlY coatings, interfaces between Ca aluminates and Ca chromates also adversely affect the degradation process in addition to the effect of the weak interface between Ca compounds and the underlying layer resulting in additional cracks in the reaction product zone. Therefore, the degradation is more severe. More severe degradation of CoNiCrAlY coatings than platinum aluminide coatings is an example associated with this mechanism.

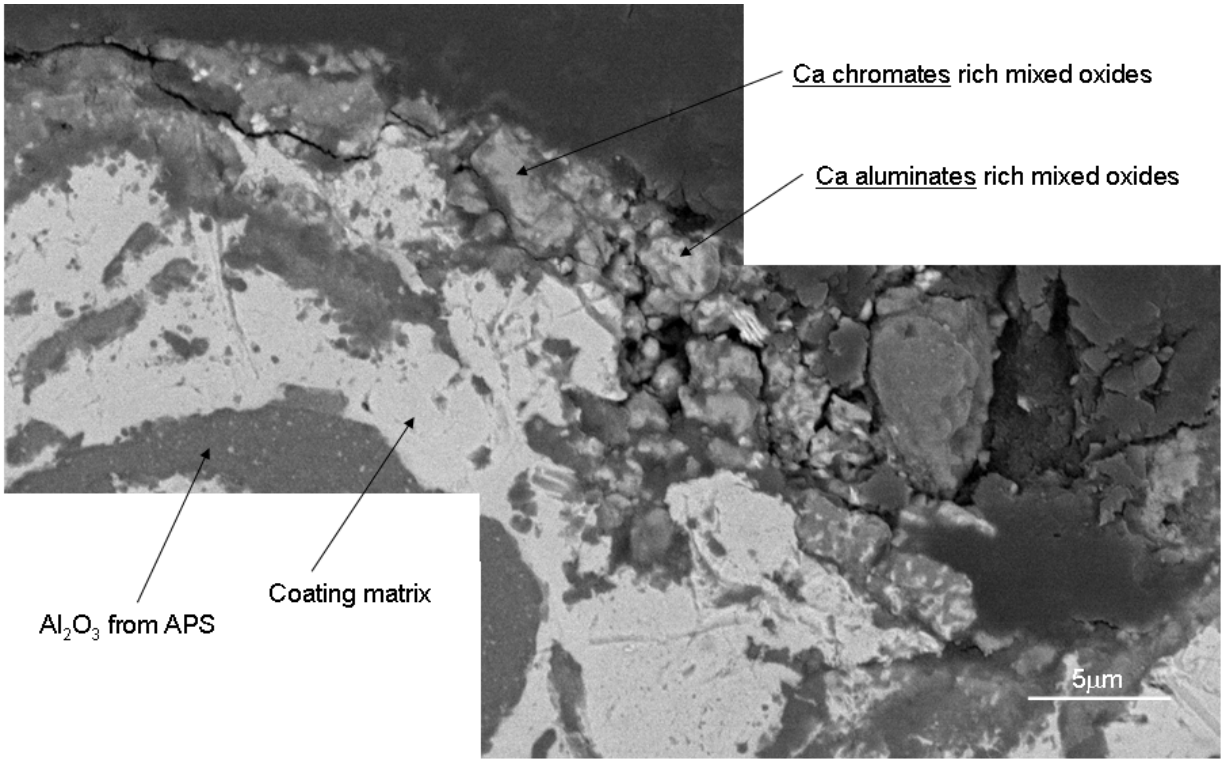

Figure 4.54 Cross-section micrograph of APS NiCrAlY coated Rene′ N5 (NN) specimen after 100 hour exposure at 950°C in dry air.

In a similar fashion, CaO reacts with ZrO_2 in the TBCs to form $CaZrO_3$, which is also the only stable ternary oxide in the pseudo-binary phase diagram as shown in Figure 4.46. Weak interfaces between Ca zirconates and the underlying topcoat are readily spalled.

Figure 4.55 shows schematic diagrams showing the adverse effect of non-protective Ca compounds during thermal cycling for (a) platinum aluminide coating, (b) MCrAlY coating, and (c) TBC coating. Red lines indicate weak interfaces which can cause initiation of cracks along the phase boundaries.

Important thermodynamic reactions associated with the formation of stable Ca ternary compounds at 950°C are as follows:

$$CaO(s) + 2Al_2O_3(s) = CaAl_4O_7(s), \quad \Delta G^{o}_{950^{o}C} = -57.100 \text{ kJ/mol}$$

$$CaO(s) + 6Al_2O_3(s) = CaAl_{12}O_{19}(s), \quad \Delta G^{o}_{950^{o}C} = -77.926 \text{ kJ/mol}$$

$$CaO(s) + Cr_2O_3(s) = CaCr_2O_4(s), \quad \Delta G^{o}_{950^{o}C} = -65.532 \text{ kJ/mol}$$

$$CaO(s) + ZrO_2(s) = CaZrO_3(s), \quad \Delta G^{o}_{950^{o}C} = -35.596 \text{ kJ/mol}$$

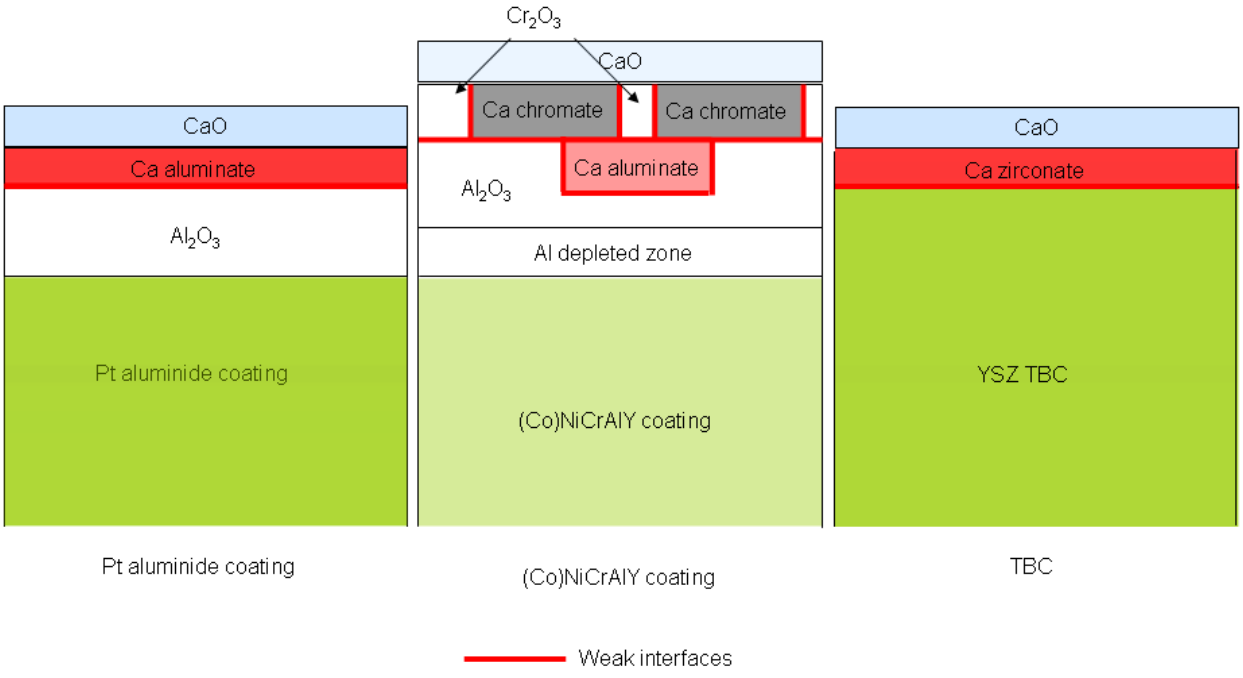

Figure 4.55 Schematic diagrams showing the adverse effect of non-protective Ca compounds on (a) platinum aluminide coating, (b) MCrAlY coating, and (c) TBC coating during thermal cycling. Red lines indicate weak phase boundaries.

4.6 EFFECTS OF CONTAMINANT LEVEL AND WATER VAPOR PRESSURE

The purpose of these experiments is to determine the effects of contaminant amount and the partial pressure of water vapor on the deposit-induced degradation. This was achieved by using the two types of specimens, namely uncoated GTD 111 and platinum aluminide and CoNiCrAlY coated GTD 111, and testing at 950^{o}C.

This experiment was divided into two parts: Part 1 – the effect of the amount of CaO and Part 2 – the effect of water vapor pressure. In order to examine the effects of the amount of deposit, as well as water vapor content, experiments were performed where the amount of the deposit, and water vapor content, were varied.

4.6.1 Part 1: The Effect of The Amount of CaO

In Part 1, 1.0±0.1 mg/cm^2 of CaO, which was the selected deposit in the initial experiments, was applied to four uncoated GTD 111 (G0) coupon specimens. The specimens were exposed for 20 hours at 950^{o}C, which was also determined in the initial experiments in section 3.2. After examination of the exposed specimens, 1.0±0.1 mg/cm^2 of the deposit was applied to three of the specimens, and all four specimens were exposed and additional 20 hours at 950^{o}C. This procedure was repeated until all specimens had been exposed 80 hours and specimen four had four times as much deposit as specimen #1 on which the deposit was applied for the first time

and not later on. These experiments were performed in dry air and in air with water vapor of 0.1 atm. During these experiments, weight changes were monitored every 20 hours and cross section microstructures were documented using the SEM and the EDAX after 80 hours exposure.

In Figure 4.56, weight change versus time measurements are presented for uncoated GTD 111 (G0) specimens with different amounts of CaO deposits. These experiments were performed in dry air and in air with water vapor at 0.1 atm. The data in Figure 4.56 are presented where the weight of the deposits are included in the measurements, (a) and (b), as well as where the weight of the deposits are subtracted from the weight change measurements, (c) and (d). Both approaches show that the amount of attack, as shown in Figure 4.56, increases as the amount of CaO deposits is increased.

Surface photographs of the exposed specimens are presented in Figure 4.57. It is evident that the degradation increases as the amount of CaO is increased, but it is not clear if there is more attack in water vapor compared to dry air. Cross-section micrographs through exposed specimens are presented in Figures 4.58 and 4.59 for dry and wet air conditions, respectively. It is clear that the amount of attack increases with the amount of CaO deposits.

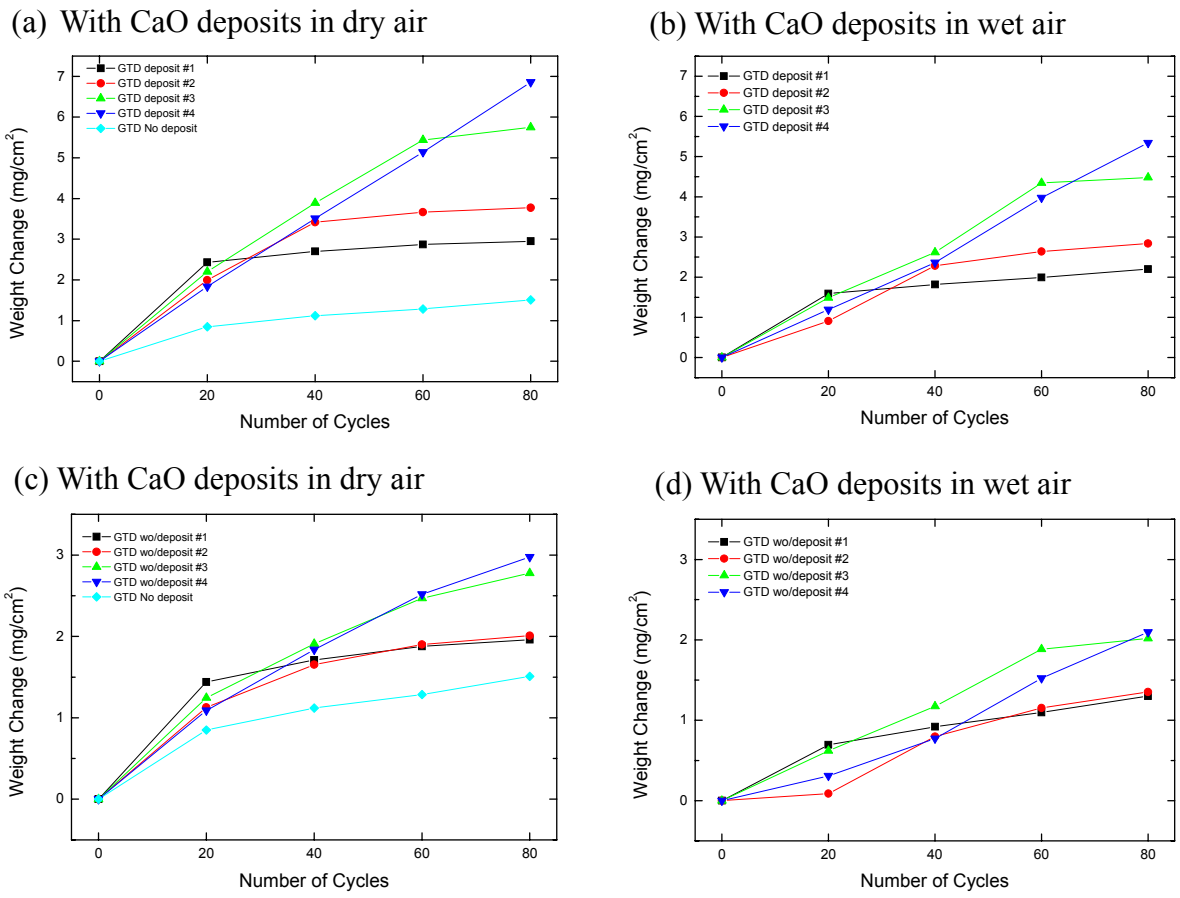

Figure 4.56 Weight change versus time measurements for uncoated GTD 111 exposed at 950°C (a) and (c) in dry, (b) and (d) in wet air with different amounts of CaO deposits.

(a) In dry air

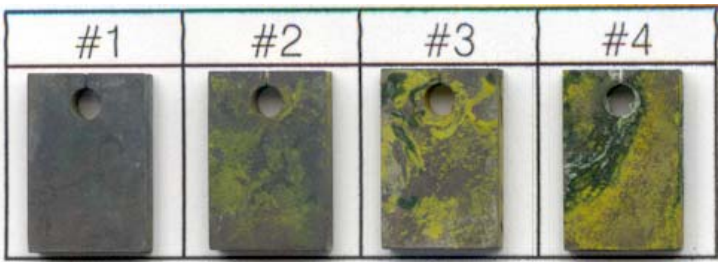

(b) In wet air

Figure 4.57 Surface photographs of uncoated GTD 111 (G0) with different amounts of CaO deposits after 80 hours exposure in (a) dry and (b) wet air. Note that the specimen #0 in (a) is the one on which no CaO was deposited.

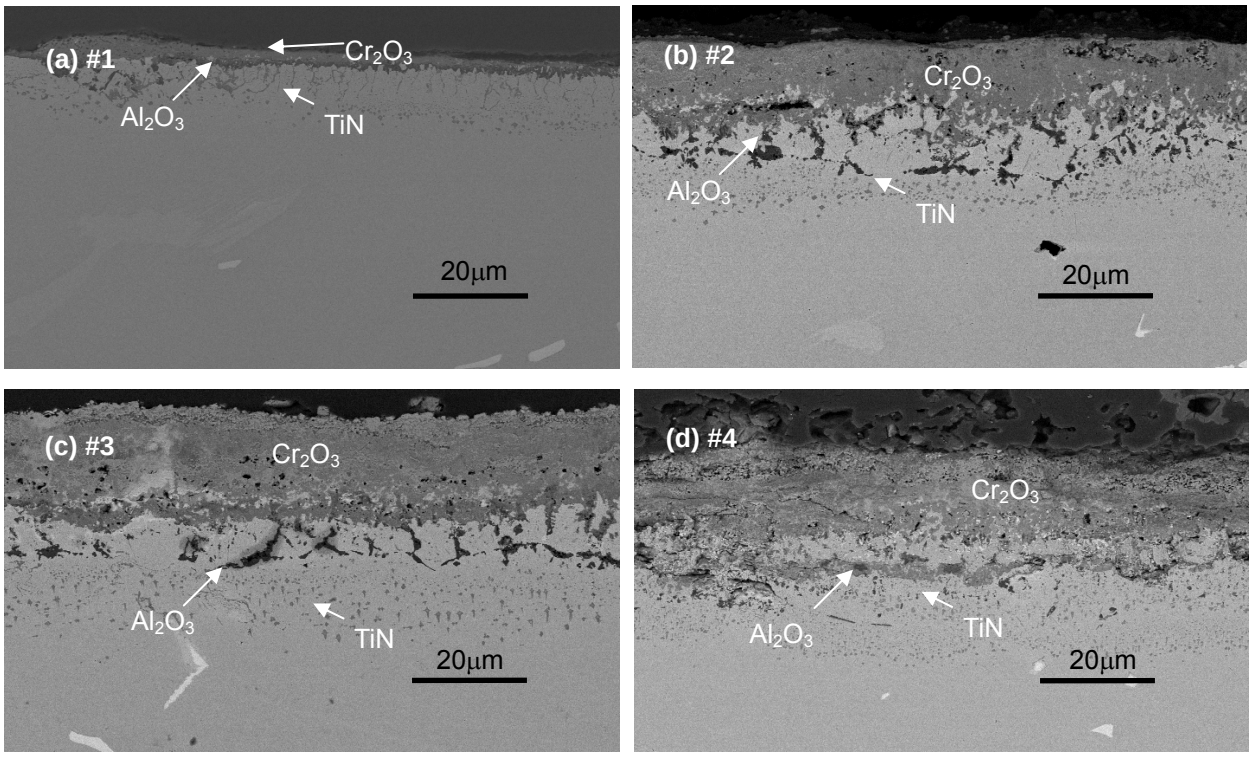

Figure 4.58 Cross-section micrographs of uncoated GTD 111 with different amounts of CaO deposits exposed at 950^{o}C after 80 hours exposure in dry air.

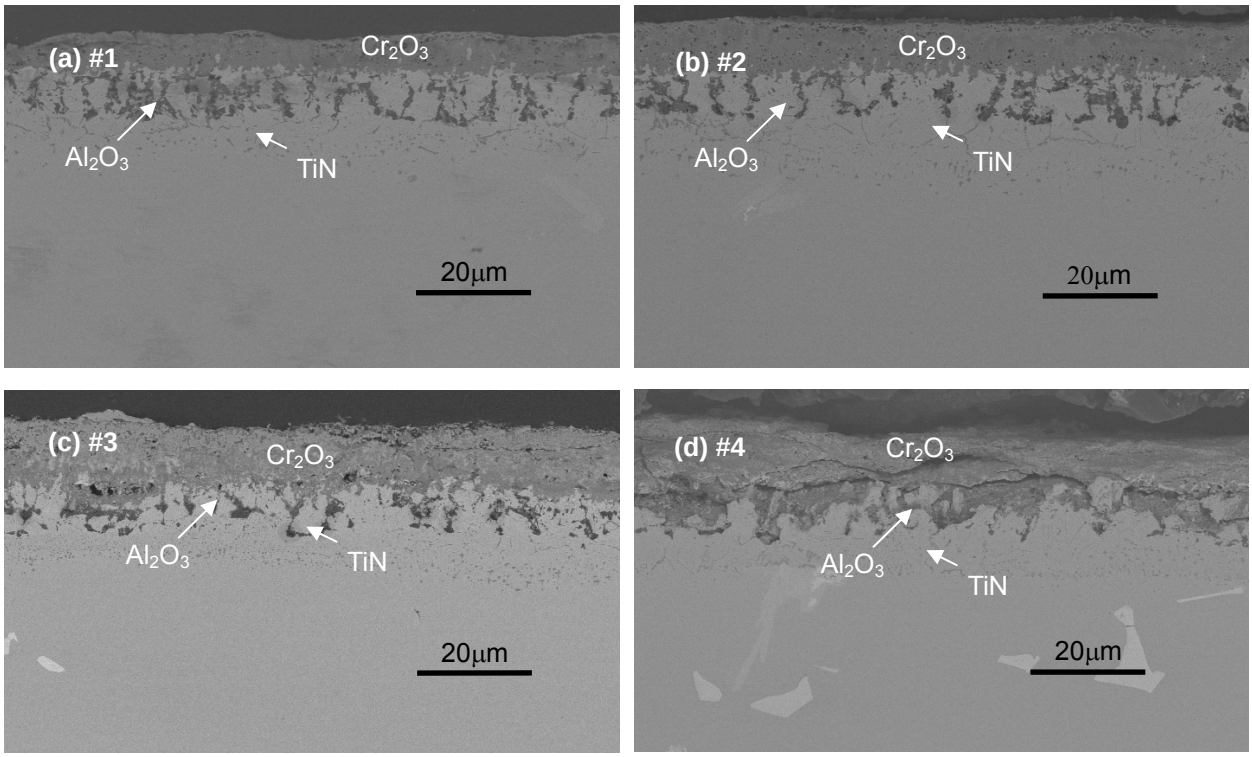

Figure 4.59. Cross-section micrographs of uncoated GTD 111 with different amounts of CaO deposits exposed at 950^{o}C after 80 hours exposure in wet air.

4.6.2 Part 2: The Effect of The Water Vapor Pressure

Experiments in Part 2 were performed with and without CaO deposits, but the water vapor pressure in the air was 0.2 atm. To establish the water vapor pressure at 0.2 atm, the temperature of the water bath was now maintained at 60.5^{o}C. The results obtained with uncoated GTD 111, as well as this alloy coated with a platinum aluminide and a CoNiCrAlY coating are presented in Figures 4.60 and 4.61. These weight change measurements were obtained for cyclic oxidation conditions at 950^{o}C and show results for no deposit, Figure 4.60, and with CaO deposits, Figure 4.61. The presence of water vapor at 0.1 atm and 0.2 atm in comparison to dry conditions has not caused consistent differences between the alloys and coatings, Figure 4.60. The weight changes are small and there are not large differences between the dry and wet results.

These results are surprising, since there are data in the literature[50] that show water vapor causes α-Al_2O_3 scales to spall more profusely, and it also causes increased vaporization of Cr_2O_3 scales.[52] It is believed that the present results do not show such effects because the temperature of 950^{o}C is low and the exposure times are short. For example, the spalling of α-Al_2O_3 induced by water vapor has been observed at 1100^{o}C and vaporization of Cr_2O_3 becomes evident after exposure times on the order of 1000 cycles. The results obtained with CaO deposits also do not show substantial effects of water vapor pressure on the amount of degradation, Figure 4.61. The

CaO deposits have caused significant degradation but a strong influence of water vapor on this degradation is not apparent.

In Figure 4.62, micrographs are presented for specimens of GTD 111 exposed to cyclic oxidation at 950^{o}C for different water vapor pressures where some of the specimens had CaO deposits and others did not. Consistent with the weight change measurements, there is a significant difference between the specimens with and without the CaO deposits, but there are not pronounced differences for specimens exposed to different water vapor pressures. Metallographic examination of the exposed specimens with the platinum aluminide and CoNiCrAlY coatings also did not show substantial effects of the water vapor pressure on the attack induced by CaO deposits. In all cases, the attack induced by CaO deposits was substantial but the available results did not show that water vapor caused this attack to be substantially more severe.

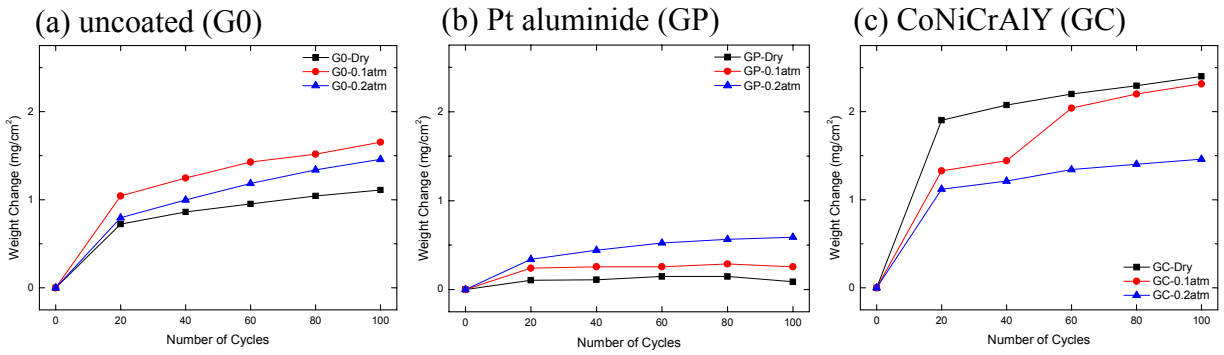

Figure 4.60 Weight change versus cycles at 950°C for (a) uncoated GTD 111 (G0), (b) GTD 111 with platinum aluminide coatings (GP), and (c) GTD 111 with CoNiCrAlY coatings (GC), for exposures with no deposit in air with different water vapor pressures.

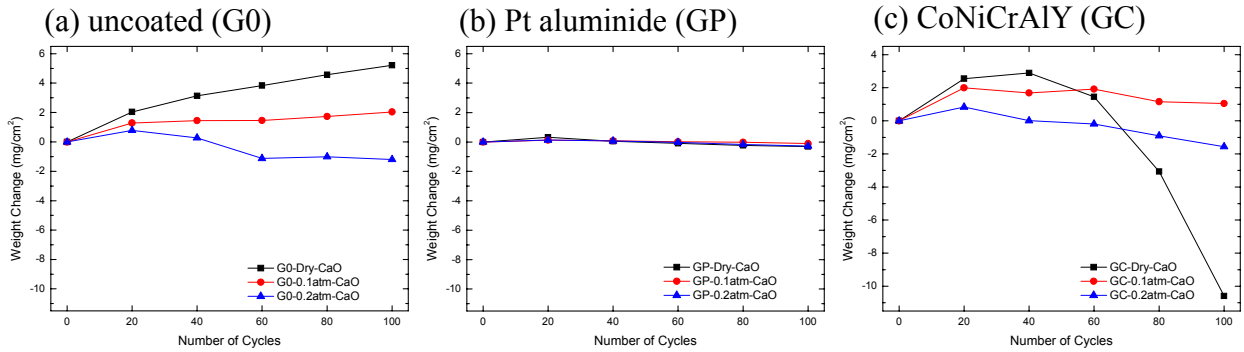

Figure 4.61 Weight change versus cycles at 950°C for (a) uncoated GTD 111 (G0), (b) GTD 111 with platinum aluminide coatings (GP), and (c) GTD 111 with CoNiCrAlY coatings (GC), for exposures with CaO deposits in air with different water vapor pressures.

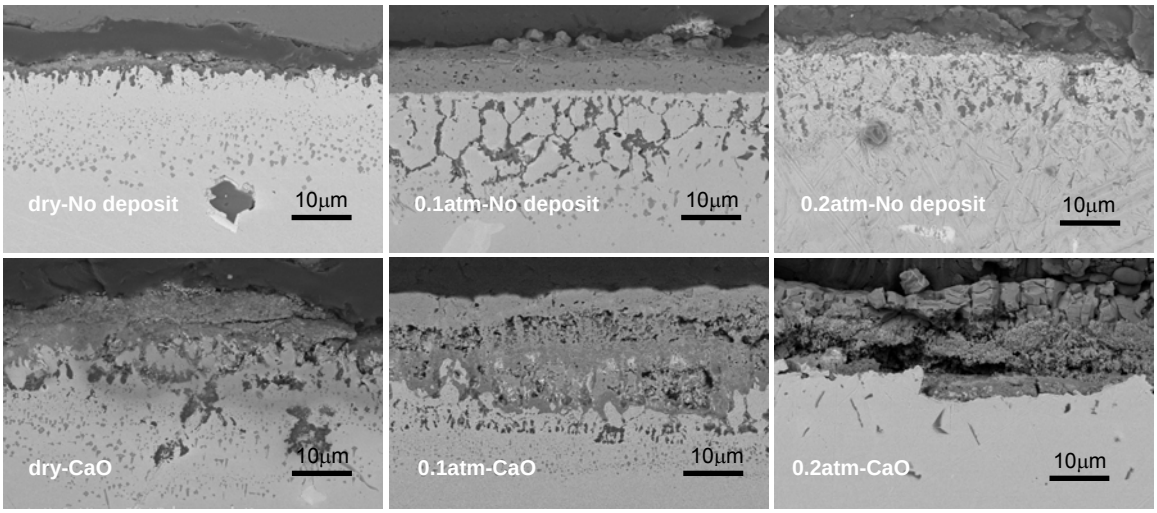

Figure 4.62 Scanning electron micrographs for uncoated GTD 111 specimens exposed to cyclic oxidation at 950^{o}C in air with different water vapor pressures when some specimens had a deposit of CaO and others did not.

4.7 EFFECTS OF DEPOSITS OF SiO_2 AND Fe_2O_3

The results obtained with CaO deposits show that solid deposits at high temperatures can cause severe alloy degradation. Early in this study, several deposits, which had been scraped from turbine blades, were examined. These were found to contain iron, as well as calcium. In is not unusual to observe iron oxides on exposed turbine hardware and they are usually considered benign. A limited number of experiments have been performed to investigate the effect of Fe-containing deposits on superalloy and coating degradation. Also, since silica is a common constituent in coal ash and dust entrained in the air, experiments were also conducted with silica deposits.

Figure 4.63 shows weight change versus number of cycles for uncoated GTD 111 (G0), GTD 111 with a CoNiCrAlY coating (GC), and GTD 111 with a Pt-modified aluminide coating (GP) exposed at 950^{o}C in dry air with and without deposits of SiO_2. The deposit has negligible effect on the weight changes for uncoated and platinum aluminide coated GTD 111. The weight gains for CoNiCrAlY-coated GTD 111 are somewhat smaller for the specimen with the SiO_2 deposit compared with the specimen exposed with no deposit which may be caused by some spalling of the SiO_2 deposit.

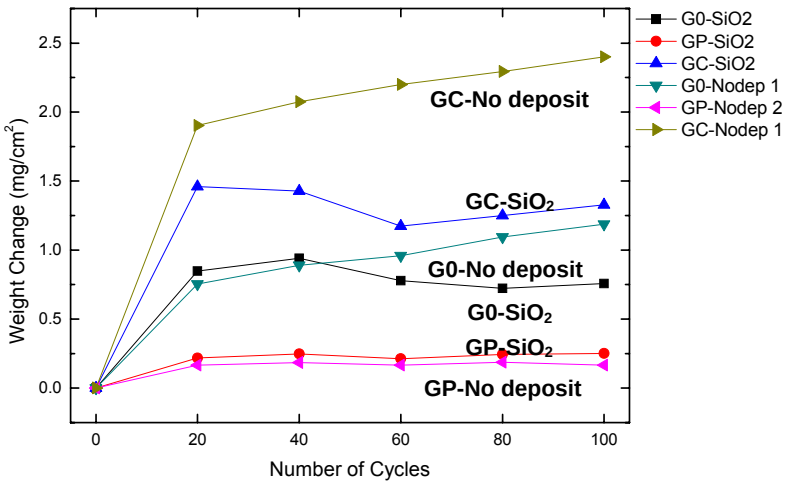

Figure 4.63 Weight change versus number of cycles for G0, GP, and GC exposed with and without SiO_2 deposits at 950°C.

Figure 4.64 shows the surfaces of these three specimens after exposure with the deposits. The outward growth of the chromia scale on uncoated GTD 111 has resulted in the incorporation of silica particles into the scale. The two coated specimens were covered with a continuous alumina scale. Figure 4.65 shows weight change versus number of cycles for uncoated GTD 111 (G0), GTD 111 with a CoNiCrAlY coating (GC), and GTD 111 with a Pt-modified aluminide coating (GP) exposed at 950°C in dry air with and without deposits of Fe_2O_3. The deposits do not result in a significant difference in the weight changes for any of the specimens. Figure 4.66 shows the surfaces of these three specimens after exposure with the deposits. There was no indication of significant reaction between the Fe_2O_3 and any of the scales.

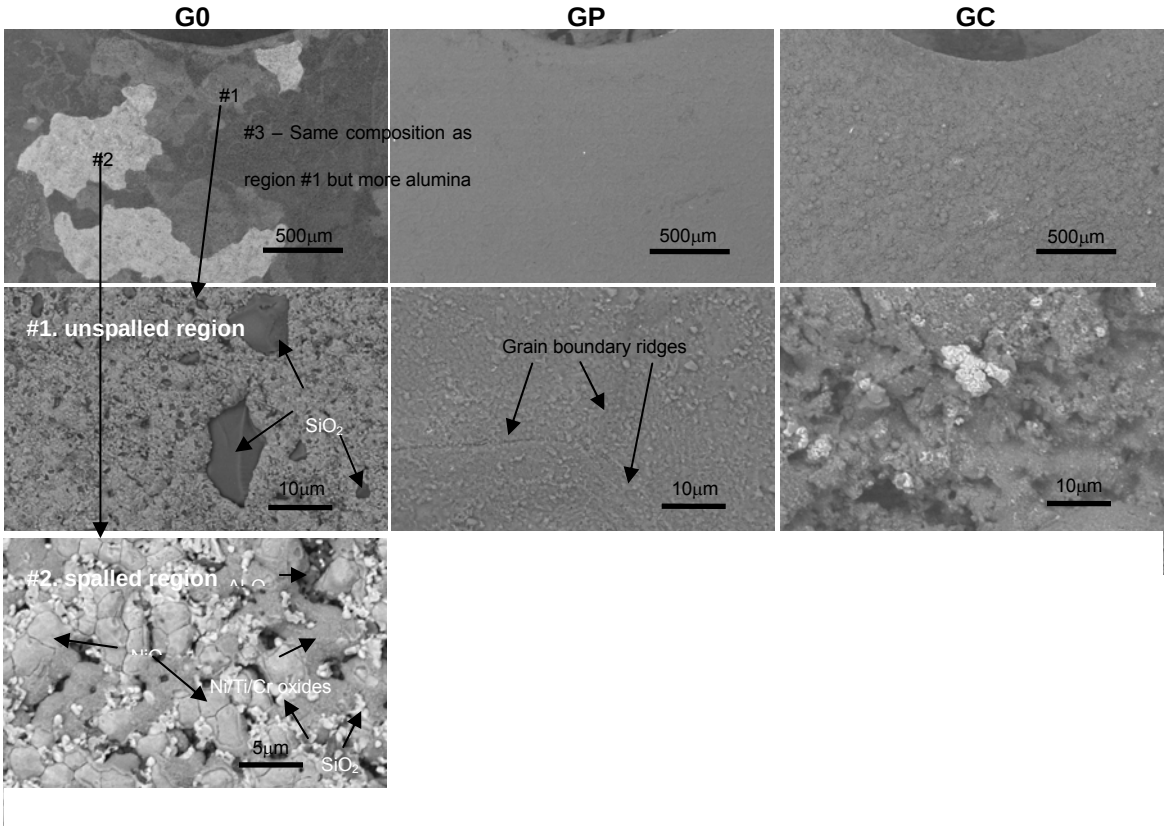

Figure 4.64 Surface micrographs of G0, GP, and GC after 100 hour cycles exposure with SiO_2 deposits at 950°C.

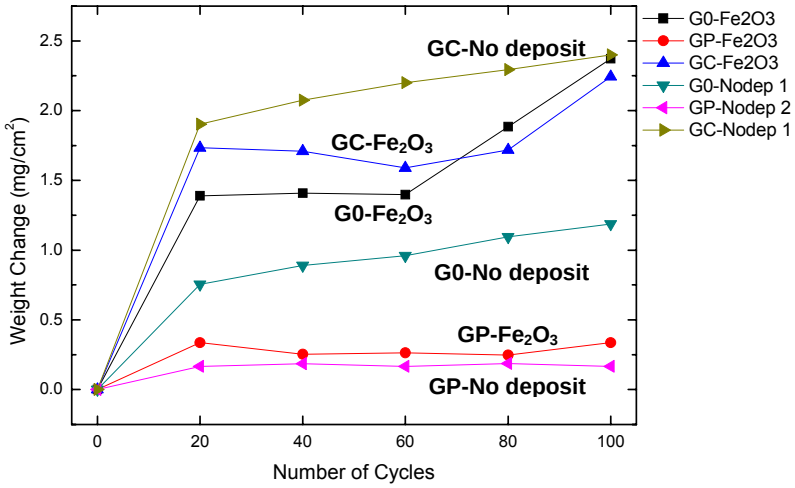

Figure 4.65 Weight change versus number of cycles for G0, GP, and GC exposed with and without Fe_2O_3 deposits at 950°C.

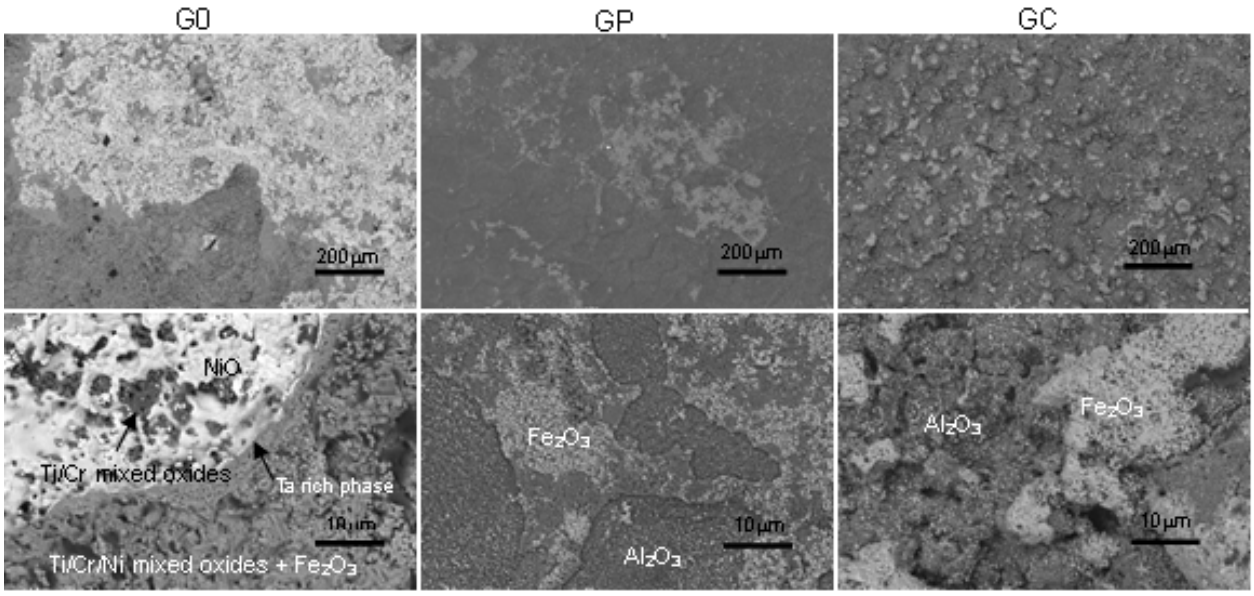

Figure 4.66 Surface micrographs of G0, GP, and GC after exposure with Fe_2O_3 deposits at 950°C.

Figure 4.67 compares the weight changes versus number of cycles for uncoated GTD 111 (G0), GTD 111 with a CoNiCrAlY coating (GC), and GTD 111 with a Pt-modified aluminide coating (GP) exposed at 950°C in dry air with no deposit and deposits of CaO, SiO_2, and Fe_2O_3. The data presented at the scale of these plots clearly demonstrate the dramatic detrimental effects of CaO compared to the other deposits.

While it is obvious from the weight change versus time measurements that CaO deposits cause much more severe degradation of the alloys and coatings than SiO_2 or Fe_2O_3, it is necessary to point out that the latter two deposits did react with some of the oxidation products

formed on the alloys and coatings as shown on Figure 4.67. The reaction of these deposits with oxidation products was more evident on the uncoated alloy than the specimens with coatings, nevertheless, some reaction with coatings was detected. Consequently, exposure of alloys and coatings to deposits such as SiO_2 and Fe_2O_3 for long periods of time at temperatures above 1000^oC may contribute to the degradation of alloys and coated alloys.

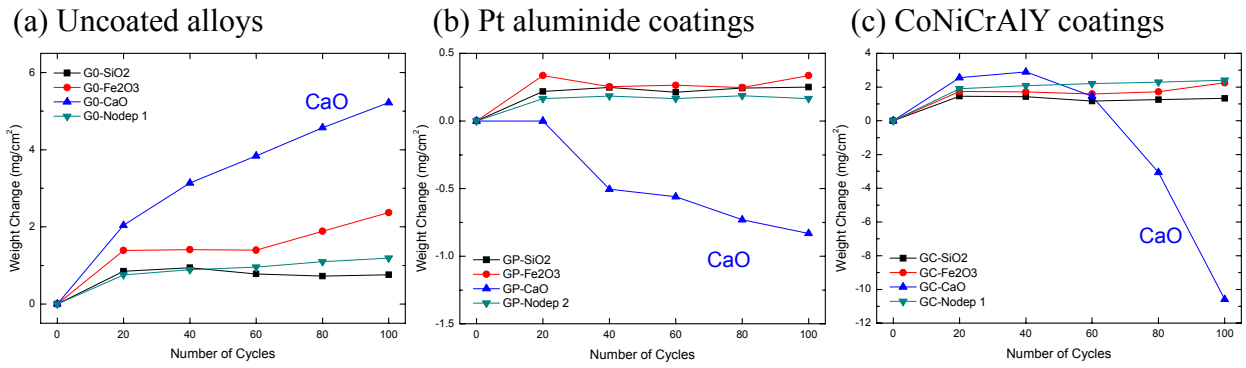

Figure 4.67 Comparison of weight change versus number of cycles for GO, GP, and GC exposed with no deposit and deposits of CaO, SiO_2, and Fe_2O_3 at 950^oC.

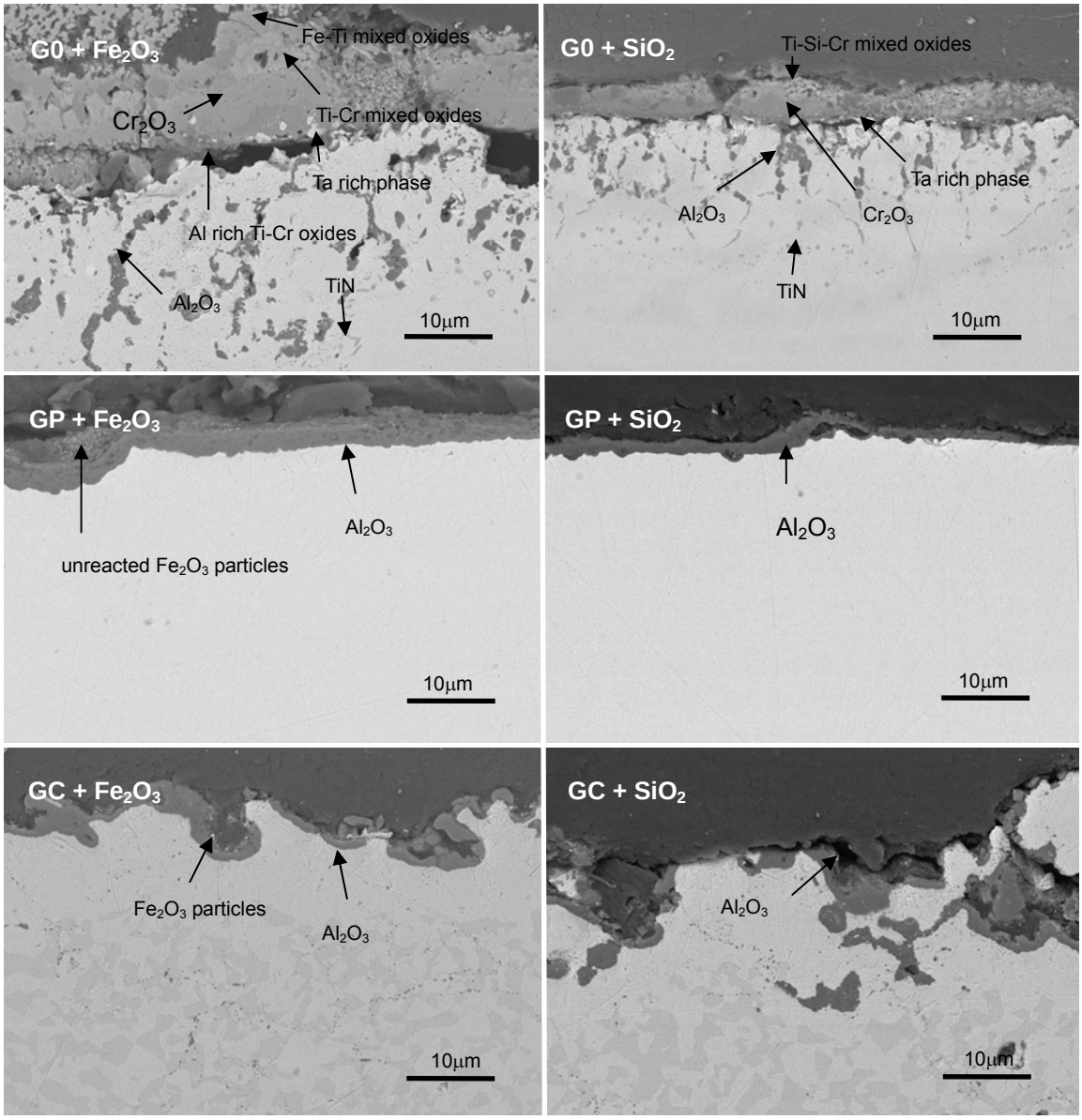

Figure 4.68 Micrographs showing oxidation products formed on coated and uncoated GTD 111 after 100 hours exposure at 950°C in dry air. This specimen had deposits of Fe_2O_3 and SiO_2 on its surface prior to oxidation.

5.0 SUMMARY AND CONCLUSIONS

5.1 RELEVANT TEST CONDITIONS

Calcium has been detected in ash deposits obtained from turbine hardware when syngas was used for combustion. Therefore, it was decided to investigate the effect of calcium in the form of CaO and $CaSO_4$ on the degradation of a number of alloys and coatings. The initial experiments were directed at determining the test conditions whereby a large number of alloys and coatings could be compared.

Platinum aluminide coated Rene′ N5 (NP) specimens were coated with three different deposits, CaO, $CaSO_4$ and Na_2SO_4. The Na_2SO_4 deposit was selected because a large body of data is available for the attack of alloys by this deposit. These specimens were exposed at three different temperatures, 750^{o}C, 950^{o}C, and 1150^{o}C. It was found that the effect of $CaSO_4$ deposits on degradation of the specimens was not significant at all three temperatures. Na_2SO_4 deposits caused typical low temperature hot corrosion at 750^{o}C in dry air containing 1000ppm SO_3 gas whereas the effect of Na_2SO_4 on degradation at 950^{o}C and 1150^{o}C both in dry and wet air was not discernable. However, CaO deposits caused severe degradation of the specimens at 950^{o}C and even more severe at 1150^{o}C both in dry and wet air although degradation at 750^{o}C was not

substantial. It was concluded that CaO substantially accelerates the degradation of platinum aluminide coated Rene′ N5 (NP).

The attack induced by CaO deposits at 1150^{o}C was very severe. Accordingly, 950^{o}C and CaO deposits were selected as the primary exposure variables for the further intensive experiments to study the effect(s) of solid deposits on degradation of various uncoated and coated superalloys.

5.2 COMPARISON OF ALLOYS AND COATINGS

Three superalloys, Rene′ N5, GTD 111, and IN 738, as well as these alloys coated with either platinum aluminide or CoNiCrAlY, were exposed in dry and wet air at 950^{o}C with CaO deposits that had been decided in the initial experiments. The effect of water vapor on degradation was not significant for all specimens under the conditions used in the present study.

5.2.1 Comparison of Uncoated Alloys

With no deposit, Rene′ N5 (N0) formed a very thin α-Al_2O_3 protective layer on the surface whereas GTD 111 (G0) and IN 738 (I0) formed a thicker external Cr_2O_3 scale, an internal discontinuous Al_2O_3 layer, and TiN particles under the oxide layers.

When CaO deposits were present, Rene′ N5 formed a very thick NiO-rich mixed oxide external scale. Ca-rich mixed oxides and a small amount of an internal Al_2O_3 layer were also formed. On the other hand, the Cr_2O_3-forming alloys, GTD 111 and IN 738, formed a thick Ca-rich, Cr_2O_3-based mixed oxides as external scales. Internal Al_2O_3 and TiN particles were present under the oxide layers. These observations were consistent with the thermogravimetric analyses showing that weight gains of specimens with CaO deposits were much larger than those with no deposit. Also, spalling of the Ca-rich oxide layers was observed.

5.2.2 Comparison of Coated Alloys

The effect of the substrate alloy composition on degradation of the coatings was not significant either with or without CaO deposits. With no deposit, the platinum aluminide coatings formed a very thin α-Al_2O_3 protective layer and CoNiCrAlY coatings also formed a relatively continuous α-Al_2O_3 protective external scale both in dry and wet air. When CaO deposits were present on the surface, the exposed specimens showed irregular surface morphologies and weight losses. However, weight changes of all coated specimens were much smaller than those of uncoated specimens. This means that coated specimens are much more resistant to the CaO-induced attack than uncoated specimens under the conditions used in the present study. Therefore, it was concluded that CaO deposits induced severe degradation of coated alloys but not as much as that

of uncoated alloys. Also, it is believed that non-uniform distribution of CaO particles over the surfaces of specimens causes preferential attack resulting in irregular surface morphologies of the coating surfaces.

Platinum aluminide coatings showed more resistance than CoNiCrAlY coatings against CaO-induced attack both in dry and wet air.

5.3 EFFECTS OF CaO DEPOSITS ON THERMAL BARRIER COATINGS

APS TBC specimens were isothermally exposed at 950^{o}C to study the effect of CaO deposits on degradation of TBCs. It turns out that $CaZrO_3$, which is the only stable ternary compound in the Ca-Zr-O phase diagram, forms via the reaction between CaO and ZrO_2 and the $CaZrO_3$ layer is prone to spall from the surface. However, since the reaction is not very extensive at 950^{o}C, the effect of CaO on overall degradation is not substantial.

Also, the TGO layers in TBC specimens with CaO deposits are thicker than those without. It is believed that Ca zirconates that form along the vertical cracks in the TBC, open paths of oxygen delivery to the TGO/TBC interface and the oxygen partial pressure at the TGO is increased to form thicker TGO layers.

5.4 INTERACTIONS BETWEEN CaO AND OXIDE SCALES

From the XRD analyses of the CaO-deposited Al_2O_3 specimens after exposure at 950^oC in dry air, $CaAl_4O_7$ was detected on the surface. It is proposed that Ca aluminates do not behave as a protective layer. Thermal cycles can cause spallation of Ca aluminate layer by propagating cracks along the Ca aluminate / Al_2O_3 interface. The degradation mechanism can be described as follows:

Step #1: CaO deposits are accumulated on the Al_2O_3 protective layer (TGO).

Step #2: CaO reacts with a normally protective Al_2O_3 layer to form Ca aluminates which are not protective against oxidation of underlying layers.

Step #3: Cracks are initiated and propagate along the interface between Ca aluminates and protective alumina layer. They cause spallation of the Ca aluminate layer.

Step #4: An Al_2O_3 protective layer is recovered when the alumina layer is exposed to high oxygen partial pressure environment after the spallation. At the same time, CaO is continuously deposited on the Al_2O_3 layer. Then, Step #1 - #4 is repeated until the coating material is completely used up.

CoNiCrAlY coated specimens with CaO deposits showed more severe degradation than platinum aluminide coated specimens due to the formation of Ca chromates in addition to Ca aluminates. More amounts of weak phase boundaries cause more severe degradation under thermal cycling due to the CTE differences between different phases and higher strain energy derived from the thicker oxide formation. In the case of the uncoated superalloys, similar processes occur, but the attack is more severe than that of coated alloys because the alloys become depleted of aluminum (Rene′ N5) and chromium (GTD 111 and IN 738) near the surface.

5.5 EFFECTS OF CONTAMINANT AMOUNT AND WATER VAPOR PRESSURE

In these experiments, the effect(s) of the amount of deposits and the water vapor pressure on uncoated GTD 111 (G0) specimens were studied. As the amount of CaO deposits was increased, more severe degradation of the specimens occurred both in dry and wet air. This result implies that the continuous introduction of CaO deposits on the surface is necessary for additional or continuous formation of Ca aluminates.

Uncoated and coated specimens of GTD 111 were exposed in air containing different water vapor pressures. The effect of water vapor pressure did not show increased spallation nor increased Cr_2O_3 vaporization as observed at 1100^{o}C and after 1000 hours exposure by other

investigators. It is believed that the test temperature is too low and the exposure time is too short in the present study to observe such results. It is concluded that the effect of water vapor is not substantial with or without CaO deposits under the conditions used in this study.

5.6 EFFECTS OF DEPOSITS OF SiO_2 AND Fe_2O_3

A limited number of experiments have been performed to investigate the effect(s) of SiO_2 and Fe_2O_3 deposits that may be present on turbine hardware when syngas is used. The deposits did not result in a significant difference in the weight changes for any of the specimens and there was no indication of significant reactions between these deposits and any of the scales compared to CaO deposits. Nevertheless, some reaction products, such as Fe or Si titanates, are evident upon metallographic observation of exposed specimens, especially of uncoated specimens. Consequently, exposure of alloys and coatings to deposits such as SiO_2 and Fe_2O_3 for long periods of time at temperature above 1000^oC may contribute to the degradation of alloys and coated alloys.

5.7 SOLID vs. LIQUID DEPOSITS

It is well documented that liquid deposits, such as Na_2SO_4 and $NaVO_3$, can cause severe degradation of alloys and coatings at elevated temperatures. The current research shows that solid deposits can also cause severe degradation of alloys and coatings. Moreover, the severity of the attack, caused by the solid deposit, is dependent upon the composition and the amount of the deposit.

BIBLIOGRAPHY

1. R. A. Wenglarz and I. G. Wright, "Alternate Fuels for Land-Based Turbines", in *Workshop Proceedings of Materials and Practices to Improve Resistance to Fuel Derived Environmental Damage In Land- and Sea-Based Turbines*, EPRI, p4-45, 2003

2. U. Lenk and P. Voitlander, *VGB Power Tech.*, Vol. 8, p57, 2001

3. V. Pareek and C. Wilkes, "Fuels in Gas Turbines", in *Workshop Proceedings of Materials and Practices to Improve Resistance to Fuel Derived Environmental Damage In Land- and Sea-Based Turbines*, EPRI, p3-1, 2003

4. S. Zurek, Wikimedia Commons, http://en.wikipedia.org/wiki/Image:IGCC_diagram. svg, 2006

5. Energy Information Administration, "Chapter 5: Coal" in *Annual Energy Outlook 2007 with Projections for 2030*, Report #: DOE/EIA-0383 (2007), Official Energy Statistics from the U.S. Government, 2007

6. Energy Information Administration, "Overview" in *Annual Energy Outlook 2008 with Projections for 2030 - Early Release*, Report #: DOE/EIA-0383 (2008), Official Energy Statistics from the U.S. Government, 2008

7. R. A. Wenglarz and J. Oakey, "Gas Turbine Issues In Advanced Gasification Systems," in *Proceedings of the 8th Liège Conference on Materials for Advanced Power Engineering*, 2006

8. W. C. Fang and R. A. Rapp, *J. Electrochem. Soc.*, Vol. 130, p2335, 1983

9. K. L. Luthra and D. A. Shores, *J. Electrochem. Soc.*, Vol. 127, p2202, 1980

10. K. L. Luthra, *Met. Trans. A*, Vol. 13A, No. 9, p1647, 1982

11. K. L. Luthra, *Met. Trans. A*, Vol. 13A, No. 10, p1843, 1982

12. K. L. Luthra, *Met. Trans. A*, Vol. 13A, No. 10, p1853, 1982

13. K. L. Luthra, "Mechanism of Low Temperature Hot Corrosion", in *High Temperature Corrosion*, edited by R. A. Rapp, NACE-6, National Association of Corrosion Engineers, Houston, TX, p507, 1983

14. K. L. Luthra, *J. Electrochem. Soc.*, Vol. 132, p1293, 1985

15. N. Birks, G. H. Meier, and F. S. Pettit, "Chapter 8. Hot Corrosion", in *Introduction to High Temperature Oxidation of Metals, Second Edition*, Cambridge University Press, Cambridge, 2006

16. R. A. Rapp, *Corros. Sci.*, Vol. 44, pp209, 2002

17. F. S. Pettit and C. S. Giggins, "Hot Corrosion" in *Superalloys II*, edited by C. T. Sims, N. S. Stoloff, and W. C. Hagel, New York, NY, John Wiley & Sons, 1987

18. N. Birks, G. H. Meier, and F. S. Pettit, "Chapter 7. Reactions of Metals in Mixed Environments", in *Introduction to High Temperature Oxidation of Metals, Second Edition*, Cambridge University Press, Cambridge, 2006

19. R. A. Rapp, "Hot Corrosion", in *Workshop Proceedings of Materials and Practices to Improve Resistance to Fuel Derived Environmental Damage In Land- and Sea-Based Turbines*, EPRI, p3-47, 2003

20. J. Stringer, *Ann. Rev. Mat. Sci.* Vol. 7, p477, 1977

21. R. A. Rapp, "Hot Corrosion of Materials", in *Selected Topics in High Temperatures Chemistry*, edited by O. Johnannesen and A. Anderson, New York, NY, Elsevier, 1989

22. N. S. Bornstein and M. A. DeCrescente, *Met. Trans.*, Vol. 2, p2875, 1971

23. B. M. Warnes, *The Influence of Vanadum on the Sodium Sulfate Induced Hot Corrosion of Thermal Barrier Coating Material*s, Ph.D. Dissertation, University of Pittsburgh, PA, 1990

24. U. Seybolt, *Trans. Met. Soc. AIME*, Vol. 242, p1955, 1968

25. N. S. Bornstein and M. A. DeCrescente, *Trans. Met. Soc. AIME*, Vol. 245, p1947, 1969

26. J. A. Goebel and F. S. Pettit, *Met. Trans.*, Vol. 1, p1943, 1970

27. J. A. Goebel, F. S. Pettit, and G. W. Goward, *Met. Trans.*, Vol. 4, p261, 1973

28. M. Li, X. Sun, W. Hu, H. Guan, and S. Chen, *Oxid. Met.*, Vol. 65, p137, 2005

29. R. H. Barkalow and G. W. Goward, "Microstructural Features of Low Temperature Hot Corrosion in Nickel and Cobalt Base MCrAlY coating Alloys", in *High Temperature Corrosion*, edited by R. A. Rapp, NACE-6, National Association of Corrosion Engineers, Houston, TX, p502, 1983

30. P. Kofstad, Chap. 14 "Corrosion in Mixed Reactants: II. Hot Corrosion and/or Salt-Induced Corrosion," in *High Temperature Corrosion*, Elsevier Applied Science, NY, p425, 1988

31. X. Zheng and R. A. Rapp, *J. Electrochem. Soc.*, Vol. 140, p2857, 1993

32. Y. S. Zhang and R. A. Rapp, Corrosion, Vol. 43, p348, 1987

33. D. K. Gupta and R. A. Rapp, *J. Electrochem. Soc.*, Vol. 127, p2194, 1980

34. Y. S. Chang and R. A. Rapp, *J. Electrochem. Soc.*, Vol. 132, p2498, 1986

35. P. D. Jose, D. K. Gupta, and R. A. Rapp, *J. Electrochem. Soc.*, Vol. 132, p735, 1985

36. D. Z. Shi and R. A. Rapp, *J. Electrochem. Soc.*, Vol. 133, p849, 1986

37. 35. N. Otsuka and R. A. Rapp, *J. Electrochem. Soc.*, Vol. 137, p46, 1990

38. R. A. Rapp and K. S. Goto, in *Hot Corrosion of Metals by Molten Salts 1*, edited by J. Braunstein and J. R. Selman, Electrochem. Soc., Pennington, NJ, p 159, 1981

39. S. C. Srivastava, K. M. Godwalla, M. K. Banerjee, *J. Mat. Sci.*, Vol. 32, p835, 1997

40. Gitanjaly, S. Prakash and S. Singh, *Bri. Corros. J.*, Vol. 37, No. 1, p56, 2002

41. M. P. Borom, C. A. Johnson, and L. A. Peluso, *Surf. Coat. Technol.*, Vol. 86-87, p116, 1996

42. C. Mercer, S. Faulhaber, A. G. Evans, and R. Darolia, *Acta Mat.*, Vol. 53, p1029, 2005

43. N. M. Yanar, F. S. Pettit and G. H. Meier, *Met. Mat. Trans. A*, Vol. 37A, p1563, 2006

44. A. G. Evans, D. R. Mumm, J. W. Hutchinson, G. H. Meier, and F. S. Pettit, *Prog. Mat. Sci.*, Vol. 46, p505, 2001

45. C. G. Levi, "Stability Issues in Thermal Barrier Coatings", Lecture Note in *Summer School on Advanced Thermostructural Materials*, University of California, Santa Barbara, CA 2006

46. S. Krämer, J. Yang, C. A. Johnson, and C. G. Levi, *J. Am. Ceram. Soc.*, Vol. 89, p10, 2006

47. R. A. Wenglarz, "Turbine Flow Path Issues for Syngas and Other Alternate Fuels", in *Impact of Alternative Fuels on Turbine Materials, Materials Workshop III*, DOE, University of Connecticut, 2002

48. W. T. Reed, *External Corrosion and Deposits*, American Elsevier Publishing Co., Inc., New York, NY, 1971

49. K. T. Chiang, G. H. Meier, and R. A. Perkins, *Journal of Materials for Energy Systems*, Vol. 6, p71, 1984

50. R. A. Wenglarz, V. K. Sethi and R. Gonzalez, *Mat. High Temp.*, Vol. 9, p145, 1991

51. R. Janakiraman, G. H. Meier, and F. S. Pettit, *Met. Trans. A*, Vol. 30A, p2905, 1999

52. G. H. Meier, K. Onal and F. S. Pettit, *Interaction of Steam/Air Mixtures With Turbine Airfoil Alloys and Coatings*, AGSTR Project (No. 99-01-SR077) Final Report, South Carolina Energy Research and Development Center, Clemson, SC, 2002

53. M. C. Maris-Sida, G.. H. Meier and F. S. Pettit, *Met. Trans. A*, 34A, p2609, 2003

54. K. Onal, M. C. Maris-Sida, G. H. Meier, and F. S. Pettit, *Materials at High Temperatures*, Vol. 20, p327, 2003

55. K. Onal, M. C. Maris-Sida, G. H. Meier and F. S. Pettit, p607 in *Superalloys 2004*, edited by K. A. Green et al, TMS, September 19, 2004

56. E. Essuman, G. H. Meier, J. Żurek, M. Hänsel and W. J. Quadakkers, *Oxid. Met.*, Vol. 69, p143, 2008

57. A. Rahmel and J. Tobolski, *Corros. Sci.*, Vol. 5, p33, 1965

58. C. W. Tuck, M. Odgers, and K. Sachs, *Corros. Sci.*, Vol. 5, p271, 1969

59. R. L. McCarron and J. W. Shulz, "The Effects of Water Vapor on the Oxidation Behavior of Some Heat Resistant Alloys", in *Proceedings of Symposium on High Temperature Gas-Metal Reactions in Mixed Environments*, AIME, New York, p360, 1973

60. H. Bouaouine, F. Armanet, and C. Coddet, in *International Congress on Metallic Corrosion*, Toronto, Canada, p379, 1989

61. I. Kvernes, M. Oliveira, and P. Kofstad, *Corros. Sci.*, Vol. 17, p237, 1977

62. R. Kremer and W. Auer, *Mat. Corros.*, Vol. 48, p35, 1997

63. E. A. Irene, *J. Electrochem. Soc.*, Vol. 121, p1613, 1974

64. J. F. Cullinan, *The Oxidation of Carbon-Carbon Composites between 300℃ and 900℃ in Oxygen and Oxygen/Water Vapor Atmospheres*, MS Thesis, University of Pittsburgh, 1989

65. E. J. Oplia and R. E. Hann, *J. Amer. Ceram. Soc.*, Vol. 87, p197, 1997

66. J. L. Smialek, R. C. Robinson, E. J. Opika, D. S. Fox and N. S. Jacobson, *Adv. Composite Mater.*, Vol. 8, p33, 1999

67. A. J. Sedriks, *Corriosion of Stainless Steels, Second Edition*, John Wiley and Sons, Inc., New York, 1996

68. K. O. Hance, *Effects of Water Vapor on the Oxidation Behavior of Alumina and Chromia Forming Superalloys at Temperatures between 700^{o}C and 1000^{o}C*, PhD Dissertation, University of Pittsburgh, 2005

69. P. Kofstad, *Microscopy of Oxidation*, edited by M. J. Bennett and G. W. Lorimer, The Institute of Metals, London, p2, 1991

70. B. A. Pint and J. M. Rakowski, *NACE Paper #00259 from NACE Corrosion 2000*, Orlando, FL, March 2000

71. G. H. Meier and F. S. Pettit, '*Investigation of Materials Performances in High Moisture Environments Including Corrosive Contaminants Typical of Those Arising by Using Alternative Fuels in Gas Turbines*', UTSR Project (04 01 SR 116) Annual and Final Reports, University of Pittsburgh, 2005, 2006, 2007, 2008

72. C. S. Giggins and F. S. Pettit, *J. Electrochem. Soc.*, Vol. 118, p1782, 1971

73. G. R. Wallwork and A. Z. Hed, *Oxid. Met.*, Vol. 3, p171, 1971

74. N. Birks, G. H. Meier, and F. S. Pettit, "Chapter 5. Oxidation of Alloys", in *Introduction to High Temperature Oxidation of Metals, Second Edition*, Cambridge University Press, Cambridge, 2006

75. N. Birks, G. H. Meier, and F. S. Pettit, "Chapter 10. Protective Coatings", in *Introduction to High Temperature Oxidation of Metals, Second Edition*, Cambridge University Press, Cambridge, 2006

76. Personal communication with K. Hance, GE Infrastructure: Energy, Greenville SC, 2007

77. A. Bennett, *Mater. Sci. Technol.* Vol. 2, p257, 1986

78. W. Lee, D. Stinton, C. Berndt, F. Erdogan, Y. Lee, and Z. Mutasim, *J. Am. Ceram. Soc*., Vol. 79, p3003, 1996

79. B. A. Pint, I. G. Wright, W. Y. Lee, Y. Zhang, K. Prussner, and K. B. Alexander, *Mat. Sci. Eng. A*, Vol. 245, p201, 1998

80. W. J. Brindley and R. A. Miller, *Adv. Mater. Proc.*, Vol. 136, p29, 1989

81. B Wu, E. Chang, D. Tu, and S. Wang, *Mater. Sci. Eng. A*, Vol. 111, p201, 1989

82. L. Lelait, S. Alperine, and R. Mevrel, J. Mater. Sci., Vol. 27, p5, 1992

83. A. C. Fox and T. W. Clyne, *Surf. Coat. Technol.*, Vol. 18, p311, 2004

84. B. Hallstedt, *J. Am. Cer. Soc*., Vol. 73, p15, 1990

85. R. W. Nurse, J. H. Welch and A. J. Majumdar, *Trans. Br. Ceram. Soc.*, Vol. 64, p323, 1965

86. G. A. Rankin and F. E. Wright, *Am. J. Sci.*, Vol. 39, p1, 1915

87. E. S. Shepherd, G. A. Rankin, and F. E. Wright, *Am. J. Sci.*, Vol. 28, p293, 1909

88. J. Jeevaratnam, F. P. Glasser, L. S. Dent Glasser, *J. Am. Cer. Soc*., Vol. 47, p105, 1964

89. J. Jeevaratnam, L. S. Dent Glasser, and F. P. Glasser, *Nature*, Vol. 194, p764, 1962

90. G.. Eriksson and A. D. Pelton, *Met. Trans. B*, Vol. 24B, p807, 1993

91. K. Lagerqvist, S. Wallmark, and A. Westgren, *Z. Anorg. Allg. Chem.*, Vol. 234, p1, 1937

92. J. E. Kopanda and G.. MacZura, "Production Processes, Properties, and Applications for Calcium Aluminate Cements", p171-184 in *Alumina Chemicals Science and Technology Handbook,* edited by L. D. Hart, American Ceramic Society, Westerville, OH, 1990